

Nonlinear Vibrations of Rotating Pretwisted Composite Blade Reinforced by Functionally Graded Graphene Platelets Under Combined Aerodynamic Load and Air Flow in Tip Clearance

X. J. Gu

Beijing University of Technology

W. Zhang (✉ sandyzhang0@yahoo.com)

Beijing University of Technology

Y. F. Zhang

Shenyang Aerospace University

Research Article

Keywords: Rotating pretwisted composite blade, graphene platelet, leakage of air flow, external and multiple parametric excitations, chaotic vibrations

Posted Date: May 24th, 2021

DOI: <https://doi.org/10.21203/rs.3.rs-524445/v1>

License: © ⓘ This work is licensed under a Creative Commons Attribution 4.0 International License.

[Read Full License](#)

Version of Record: A version of this preprint was published at Nonlinear Dynamics on July 13th, 2021.
See the published version at <https://doi.org/10.1007/s11071-021-06681-z>.

Nonlinear Vibrations of Rotating Pretwisted Composite Blade Reinforced by Functionally Graded Graphene Platelets under Combined Aerodynamic Load and Air Flow in Tip Clearance

X. J. Gu^{a1}, W. Zhang^{a2*} and Y. F. Zhang^{b3*}

^aBeijing Key Laboratory of Nonlinear Vibrations and Strength of Mechanical Structures
College of Mechanical Engineering, Beijing University of Technology
Beijing 100124, P. R. China

^bCollege of Aerospace Engineering, Shenyang Aerospace University
Liaoning 110136, P. R. China

¹Email: guxiaojun1992@yahoo.com, ²Email: sandyzhang0@yahoo.com

³Email: yufeizhang73@163.com

Running Headline: Nonlinear vibrations of Rotating Composite Cantilever Blades

Submitted to: *Nonlinear Dynamics*, May 13, 2021

Revised Version:

Number of Pages: 54

Number of Figures: 20

* corresponding authors, emails: sandyzhang0@yahoo.com, yufeizhang73@163.com

Abstract

The primary resonance and nonlinear vibrations of the functionally graded graphene platelet (FGGP) reinforced rotating pretwisted composite blade under combined the external and multiple parametric excitations are investigated with three different distribution patterns. The FGGP reinforced rotating pretwisted composite blade is simplified to the rotating pretwisted composite cantilever plate reinforced by the functionally graded graphene platelet. It is novel to simplify the leakage of the air flow in the tip clearance to the non-uniform axial excitation. The rotating speed of the steady-state adding a small periodic perturbation is considered. The aerodynamic load subjecting to the surface of the plate is simulated as the transverse excitation. Utilizing the first-order shear deformation theory, von-Karman nonlinear geometric relationship, Lagrange equation and mode functions satisfying the boundary conditions, three-degree-of-freedom nonlinear ordinary differential equations of motion are derived for the FGGP reinforced rotating pretwisted composite cantilever plate under combined the external and multiple parametric excitations. The primary resonance and nonlinear dynamic behaviors of the FGGP reinforced rotating pretwisted composite cantilever plate are analyzed by Runge-Kutta method. The amplitude-frequency response curves, force-frequency response curves, bifurcation diagrams, maximum Lyapunov exponent, phase portraits, waveforms and Poincare map are obtained to investigate the nonlinear dynamic responses of the FGGP reinforced rotating pretwisted composite cantilever plate under combined the external and multiple parametric excitations.

Key words: Rotating pretwisted composite blade, graphene platelet, leakage of air flow, external and multiple parametric excitations, chaotic vibrations

1. Introduction

As a key component of the aero engine, the blade is crucial to the flight safety. To improve the flight efficiency and to enhance the thrust-weight ratio of the aero engine, the composite materials with the lighter and better mechanical properties are applied in the airplane and is highly significant. The graphene, as an advanced carbon nano material, has been widely researched in recent years. The characteristics of the low mass density and excellent mechanical performance of the graphene reinforcements make it extremely meaningful to apply in the blade. The service environment of the rotating blade is complex and changeable, which subjects to various excitations, such as the aerodynamic excitation, centrifugal force and thermal stress. During the airplane flight, the primary resonance and nonlinear vibrations of the blade often happen. The blade can be simplified to the rotating pretwisted composite cantilever plate. It is necessary for us to research the primary resonance and nonlinear vibrations of the rotating pretwisted composite cantilever plate reinforced the functionally graded graphene platelet (FGGP) under combined the external and multiple parametric excitations. The novelty of this paper is to simplify the leakage of the air flow in the tip clearance to the non-uniform axial excitation. It is found that the axial excitation and distribution of the graphene have significant influences on the primary resonance and nonlinear vibrations of the FGGP reinforced rotating pretwisted composite cantilever plate.

Because of the excellent mechanical properties, the graphene reinforced composites have attracted attentions for many researchers. The buckling and post-buckling properties of the FGGP reinforced beams were investigated by Yang et al [1]. Chen et al. [2] used Timoshenko beam theory to research the nonlinear vibrations and post-buckling on the porous nano-composite beams reinforced by the graphene platelets. Based on the non-uniform rational B-spline formulation, Kiani [3] investigated the large amplitude free vibration of the FGGP reinforced plate and took into account the influence of the temperature on the material properties. Mao and Zhang [4,5] investigated on the vibration and stability of the piezoelectric composite plate reinforced by the graphene platelets. Based on the high-order shear deformation theory, Wang et al. [6] presented an investigation on the frequency and bending behaviors of the graphene platelet reinforced doubly-curved shallow shell. Zhao et al. [7] employed the finite element method to research the nonlinear bending problems of the FGGP reinforced trapezoidal plate and discussed the influence of the bottom angle on the bending characteristics of the

trapezoidal plates. Considering an open edge crack, Tam et al. [8] explored the nonlinear bending of the functionally graded graphene reinforced beam.

Due to the complexity of the geometry features for the blade, many scholars simplified it as the rotating beam with the high aspect ratio, rotating plate and rotating shell with the low aspect ratio to analyze the vibration. The linear vibration characteristics of the rotating blades were studied by many researches. Gupta and Rao [9] presented an analysis of the torsional frequencies on the pretwisted cantilever plate. The frequency and critical load of the thick rotating blades with cracked were investigated by Chen et al. [10]. Sun et al. [11,12] respectively proposed the plate model and shell model to study the free vibration of a rotating pretwisted blade. Cao et al. [13] applied the first-order deformation theory to investigate the free vibration of a sandwich blade considering the thermal barrier coating layers. In [14], a thick shell theory was employed to analyze the linear vibration of the rotating pretwisted functionally grade sandwich blade. The model considering the couple effect among the stretching, bending and torsion was proposed by Oh and Yoo [15]. The shallow shell theory was utilized in [16] to study the influence of the initial geometric imperfection on the linear frequency and mode of the rotating pretwisted panel. Using Chebyshev-Ritz method, Niu et al. [17] and Zhang et al. [18] respectively analyzed the natural vibration of the rotating pretwisted functionally graded composite cylindrical blade and tapered blade reinforced with the graphene platelets. The free vibrations of a rotating pretwisted beam under the axial loading were studied by Ondra and Titurus [19]. Gu et al. [20] presented a shallow shell model to investigate the dynamic stability of a rotating twisted plate considering the initial imperfection. Using the couple model, Zhao et al. [21] researched the free vibration of a rotating pretwisted blade-shaft reinforced by graphene platelets. Maji and Singh [22] investigated the free vibration of the rotating cylindrical shell by using the third-order shear deformation theory. Based on the shallow shell theory, Li and Cheng [23] used the variable thickness model to study the free vibration of the rotating pre-twisted blades. Xiang et al. [24] adopted the shell model to research the free vibration of the composite blade.

The vibration behaviors of the blade could not be solved completely by the linear vibration theory. The nonlinear vibration theory was introduced into the blade vibration analysis. Avramov et al. [25] investigated the flexural-flexural-torsional nonlinear vibrations of the rotating beam. Wang and Zhang [26] considered the geometric nonlinear model to study the stability and bifurcations of the rotating blade. Arvin et al. [27] applied the flapping nonlinear normal modes to analyze 2:1 internal resonances. Considering the

influence of varying rotating speed, Yao et al. [28] explored the nonlinear vibrations of the blade. Bekhoucha et al. [29] utilized Galerkin and harmonic balance methods to research the nonlinear forced vibrations of the rotating beam. Based on Galerkin and multiple scale methods, Arvin and Lacarbonara [30] investigated the nonlinear dynamic responses of the rotating beam. Yao et al. [31] employed a pre-twisted, presetting and thin walled rotating beam model to analyzed 2:1 internal resonance and primary resonance of the compressor blade. Zhang and Li [32] studied the nonlinear vibrations of the rotating blade. Wang et al. [33] used a two-degree-of-freedom model to analyze 1:1 internal resonance of the turbine blade under the air flows. Roy and Meguid [34] investigated the nonlinear transient dynamic responses of a rotating blade. Bai et al [35] developed a new method to promote the computational efficiency of the vibration characteristics and reliability analysis. Yao et al. [36] employed the cylindrical shell model to study the nonlinear dynamic responses of the rotating blade. Using the vortex lattice method, Zhang et al. [37] developed an analysis method of the nonlinear resonances for a rotating composite blade under the subsonic flow excitation. Niu et al. [38] utilized the backward differentiation formula and Runge-Kutta Algorithm to analyze the nonlinear transient responses of the rotating FGM cylindrical panel. Considering the effect of varying cross-section and aerodynamic force, Zhang et al. [39] researched the nonlinear vibrations and internal resonance of a rotating blade. Hao et al. [40] investigated the nonlinear transient responses of a rotating pretwisted cantilever plate. Zhang et al. [41] considered the strong gas pressure to study the super-harmonic resonances of a rotating pre-deformed blade.

The literature reviews indicate that applying the graphene composites with the superior properties to the rotating blade is highly meaningful. Studying the nonlinear vibrations and resonances of the rotating blade are very important to the blade designs and failure analysis. Few analyses can be found on the primary resonance and nonlinear vibrations of the FGGP reinforced composite blade under the non-uniform axial excitation generated by leakage flow at the tip clearance. In this paper, the primary resonance and nonlinear dynamic responses of the FGGP reinforced rotating pretwisted composite cantilever plate with three different distribution patterns are studied by considering the external and multiple parametric excitations. The load generated by the leakage flow at the tip clearance is simplified to the non-uniform axial excitation. There exists the rotating speed of the steady-state adding a small periodic perturbation. The aerodynamic load subjecting to the surface of the blade is simplified to the transverse excitation. Utilizing the first-order shear deformation theory, von-Karman nonlinear geometric relationship,

Lagrange equation and mode functions satisfying the boundary conditions, three-degree-of-freedom nonlinear ordinary differential governing equations of motion are derived for the FGGP reinforced rotating pretwisted composite cantilever plate. Runge-Kutta method is applied to analyze the primary resonance and nonlinear dynamics of the rotating pretwisted composite cantilever plate under the axial and transverse excitations. The amplitude-frequency and force-frequency response curves, bifurcation diagrams, maximum Lyapunov exponent, phase portraits, waveforms and Poincare map are obtained to investigate the nonlinear dynamic responses of the FGGP reinforced rotating pretwisted composite cantilever plate under combined the external and multiple parametric excitations.

2. Dynamic Modeling of Vibration

The theoretical formulation is derived for a blade, which is simplified to a FGGP reinforced rotating pretwisted composite cantilever plate. The aerodynamic load subjects to the surface of the rotating pretwisted composite cantilever plate. The leakage flows generated at the tip clearance is simulated as the non-uniform axial excitation. The rotating pretwisted composite cantilever plate is subjected to the varying rotating speed. Therefore, the rotating pretwisted composite cantilever plate is subjected to the transverse and multiple parametric excitations. The length, width and thickness of the FGGP reinforced rotating pretwisted composite cantilever plate respectively are a , b and h .

There are four coordinate systems to describe the model of the blade, as shown in Figures 1(a) and 1(b). The coordinate system (X_1, Y_1, Z_1) is defined on the center of the rotating disk with the radius R and rotating speed Ω . The rotating pretwisted composite cantilever plate is fixed on the disk. The coordinate system (X, Y, Z) is defined on the center of the root for the pretwisted composite cantilever plate, in which the axes X and Y respectively parallel to X_1 and Y_1 , and the axis Z coincides with the axis Z_1 . The coordinate system (x, y_0, z_0) is obtained by rotating the coordinate system (X, Y, Z) at angle φ around the axis Z , in which the axis y_0 coincides with the median of the cantilever plate root. The unit vector in the coordinate system (x, y_0, z_0) is denoted as $(\mathbf{i}, \mathbf{j}, \mathbf{k})$. The coordinate system (x, y, z) is defined to describe the pretwisted of the cantilever plate. The y axis is equal to the y_0 axis on the root of the cantilever plate.

The pretwisted angle is denoted as θ at the top of the cantilever plate. The twist rate is assumed to be the linear distribution from the root to tip of the plate, which is denoted as $\kappa = \theta/a$.

As show in Figure 1(a), the aerodynamic load subjects to the surface of the blade in transverse direction and is simplified to the transverse excitation F . Besides, the load on the top of the plate is induced by the leakage flows at the tip clearance. Based on reference [42], the sketch map of the airflow through the tip clearance of the blade is obtained, as shown in Figure 2(a). It is found that the aerodynamic load on the edge of the blade tip is small due to the presence of the separation bubble and reaches the maximum value P_{\max} after the gas flows goes into the tip clearance. Then, the pressure on the top of the blade gradually diminishes. Therefore, the aerodynamic load on the blade tip is simplified to the non-uniform axial excitation, as shown in Figure 2(b).

The non-uniform axial excitation P_{in} of the FGGP reinforced rotating pretwisted composite cantilever plate is expressed as

$$P_{in} = (P_{\max} - P_{03}) \left(-\frac{4z}{h} + 2 \right) + P_{03}, \quad \left(\frac{h}{4} \leq z \leq \frac{h}{2} \right), \quad (1a)$$

$$P_{in} = (P_{\max} - P_{03}) \left(\frac{4z}{3h} + \frac{2}{3} \right) + P_{03}, \quad \left(-\frac{h}{2} \leq z \leq \frac{h}{4} \right), \quad (1b)$$

$$P_{\max} = P_{01} + P_{02} \cdot \cos(\omega t) + P_{03}, \quad (1c)$$

where P_{01} and P_{03} are the static part of the axial excitation, P_{02} is the static part and dynamic part of the axial excitation, ω is the frequency of the dynamic part for the axial excitation.

The aerodynamic load subjects to the surface of the blade and is simulated as the transverse excitation with the harmonic form. Therefore, the transverse excitation F of the FGGP reinforced rotating pretwisted composite cantilever plate is written as

$$F = F_{\tau} \cdot \cos(\Omega_1 t), \quad (2)$$

where F_{τ} and Ω_1 are the amplitude and frequency of the transverse excitation, respectively.

As show in Figure 1(b), the location vector \mathbf{r}_0 on the middle surface of the rotating pretwisted composite cantilever plate is obtained as

$$\mathbf{r}_0 = x\mathbf{i} + y\cos(\kappa x)\mathbf{j} + y\sin(\kappa x)\mathbf{k}. \quad (3)$$

Using the method given in reference [12], Lamé parameters of the FGGP reinforced

rotating pretwisted composite cantilever plate are written as

$$A = |\mathbf{r}_{0,x}| = \sqrt{1 + \kappa^2 y^2}, \quad (4a)$$

$$B = |\mathbf{r}_{0,y}| = 1. \quad (4b)$$

The unit vector $(\mathbf{a}_1, \mathbf{a}_2, \mathbf{a}_3)$ in the coordinate (x, y, z) is obtained as

$$\mathbf{a}_1 = \frac{\mathbf{r}_{0,x}}{A} = \frac{1}{A}(\mathbf{i} - y\kappa \sin(\kappa x)\mathbf{j} + y\kappa \cos(\kappa x)\mathbf{k}), \quad (5a)$$

$$\mathbf{a}_2 = \frac{\mathbf{r}_{0,y}}{B} = \cos(\kappa x)\mathbf{j} + \sin(\kappa x)\mathbf{k}, \quad (5b)$$

$$\mathbf{a}_3 = \mathbf{a}_1 \times \mathbf{a}_2 = \frac{1}{A}(-y\kappa \mathbf{i} - \sin(\kappa x)\mathbf{j} + \cos(\kappa x)\mathbf{k}). \quad (5c)$$

To describe the pretwisted properties of the rotating composite cantilever plate, the second quadratic form Φ_2 is derived as

$$\Phi_2 = Ldx^2 + 2Mdx dy + Ndy^2, \quad (6a)$$

$$L = \mathbf{a}_3 \cdot \mathbf{r}_{0,xx} = 0, \quad (6b)$$

$$M = \mathbf{a}_3 \cdot \mathbf{r}_{0,xy} = \frac{\kappa}{\sqrt{1 + \kappa^2 y^2}}, \quad (6c)$$

$$N = \mathbf{a}_3 \cdot \mathbf{r}_{0,yy} = 0. \quad (6d)$$

The radii R_x and R_y respectively are located in the x and y directions. The radii R_x , R_y and twisted rate R_{xy} are obtained by

$$\frac{1}{R_x} = \frac{L}{A^2} = 0, \quad (7a)$$

$$\frac{1}{R_y} = \frac{N}{B^2} = 0, \quad (7b)$$

$$\frac{1}{R_{xy}} = \frac{M}{AB} = \frac{\kappa}{1 + \kappa^2 y^2}. \quad (7c)$$

The FGGP reinforced rotating pretwisted composite cantilever plate is composed of N_L layers with the same thickness $\Delta h = h/N_L$, as shown in Figure 3. The reinforcement and matrix of the rotating pretwisted composite cantilever plate are the graphene platelets and epoxy polymer, respectively. It is seen from Figure 3 that in each layer, the graphene platelets are uniformly dispersed in the epoxy polymer. The darker colors represent the more graphene platelets. The graphene platelets are uniformly distributed among the

whole plate, calling as the U pattern, see Figure 3(a). The plate with the O pattern exhibited in Figure 3(b) demonstrates that in the middle layer, the graphene platelet contents are high. From the middle layer to the upper and lower surfaces, the graphene platelets decrease gradually. The plate with the X pattern has the opposite distribution pattern with the O pattern, as shown in Figure 3(c).

Based on reference [17], the volume fractions $V_G^{(k)}$ ($k=1,2,...,N_L$) of the k th layer graphene platelet are written as

pattern U

$$V_G^{(k)} = V_G^*, \quad (8a)$$

pattern O

$$V_G^{(k)} = 2V_G^* (1 - |2k - N_L - 1| / N_L), \quad (8b)$$

pattern X

$$V_G^{(k)} = 2V_G^* |2k - N_L - 1| / N_L, \quad (8c)$$

where V_G^* ($k=1,2,...,N_L$) denote the total volume fractions of the graphene platelets

$$V_G^* = \frac{f_G}{f_G + (1 - f_G)(\rho_G / \rho_M)}, \quad (9)$$

and f_G is the total weight fraction of the graphene platelets, ρ_G and ρ_M respectively denote the densities of the graphene platelets and epoxy polymer.

Based on Halpin-Tsai model [1], the effective Young modulus $E_c^{(k)}$ of the k th layer for the FGGP reinforced rotating pretwisted composite cantilever plate is calculated as

$$E_c^{(k)} = \frac{3}{8} \frac{1 + \xi_L \eta_L V_G^{(k)}}{1 - \eta_L V_G^{(k)}} \times E_M + \frac{5}{8} \frac{1 + \xi_w \eta_w V_G^{(k)}}{1 - \eta_w V_G^{(k)}} \times E_M, \quad (10)$$

where

$$\eta_L = \frac{\left(\frac{E_G}{E_M}\right) - 1}{\left(\frac{E_G}{E_M}\right) + \xi_L}, \quad \xi_L = \frac{2l_G}{h_G}, \quad (11a)$$

$$\eta_w = \frac{\left(\frac{E_G}{E_M}\right) - 1}{\left(\frac{E_G}{E_M}\right) + \xi_w}, \quad \xi_w = \frac{2w_G}{h_G}, \quad (11b)$$

where l_G , w_G and h_G are the length, width and height of the graphene platelets, E_M

and E_G respectively denote Young's moduli of the epoxy polymer and graphene platelets.

The $\nu_c^{(k)}$ and $\rho_c^{(k)}$ are Poisson ratios and density of the k th layer for the graphene platelets, respectively

$$\nu_c^{(k)} = \nu_G V_G^{(k)} + \nu_M (1 - V_G^{(k)}), \quad \rho_c^{(k)} = \rho_G V_G^{(k)} + \rho_M (1 - V_G^{(k)}). \quad (12)$$

The displacement components u_0 , v_0 and w_0 along the directions O_1x , O_1y and O_1z of the FGGP reinforced rotating pretwisted composite cantilever plate are obtained by using the first-order shear deformation theory

$$u = u_0 + z\phi_x, \quad (13a)$$

$$v = v_0 + z\phi_y, \quad (13b)$$

$$w = w_0, \quad (13c)$$

where u_0 , v_0 and w_0 are located in the middle surface along the directions (x, y, z) , respectively, ϕ_x and ϕ_y are the angles along the axes y and x , respectively.

The strain displacement relations of the FGGP reinforced rotating pretwisted composite cantilever plate are

$$\varepsilon_{xx} = \frac{\partial u}{\partial x} + \frac{w}{R_x} + \frac{1}{2} \left(\frac{\partial w}{\partial x} \right)^2, \quad \varepsilon_{yy} = \frac{\partial v}{\partial y} + \frac{w}{R_y} + \frac{1}{2} \left(\frac{\partial w}{\partial y} \right)^2, \quad (14a)$$

$$\gamma_{xy} = \frac{\partial u}{\partial y} + \frac{\partial v}{\partial x} + \frac{\partial w}{\partial x} \frac{\partial w}{\partial y} + \frac{2w}{R_{xy}}, \quad \gamma_{yz} = \frac{\partial v}{\partial z} + \frac{\partial w}{\partial y} - \frac{v_0}{R_y} - \frac{u_0}{R_{xy}}, \quad (14b)$$

$$\gamma_{xz} = \frac{\partial u}{\partial z} + \frac{\partial w}{\partial x} - \frac{u_0}{R_x} - \frac{v_0}{R_{xy}}. \quad (14c)$$

Substituting equation (14) into equation (13), the strains can be written as

$$\varepsilon_{xx} = \varepsilon_{xx}^{(0)} + z\varepsilon_{xx}^{(1)}, \quad \varepsilon_{yy} = \varepsilon_{yy}^{(0)} + z\varepsilon_{yy}^{(1)}, \quad \gamma_{xy} = \gamma_{xy}^{(0)} + z\gamma_{xy}^{(1)}, \quad \gamma_{xz} = \gamma_{xz}^{(0)}, \quad \gamma_{yz} = \gamma_{yz}^{(0)}, \quad (15)$$

where

$$\varepsilon_{xx}^{(0)} = \frac{\partial u_0}{\partial x} + \frac{1}{2} \left(\frac{\partial w_0}{\partial x} \right)^2, \quad \varepsilon_{yy}^{(0)} = \frac{\partial v_0}{\partial y} + \frac{1}{2} \left(\frac{\partial w_0}{\partial y} \right)^2, \quad \gamma_{xy}^{(0)} = \frac{\partial u_0}{\partial y} + \frac{\partial v_0}{\partial x} + \frac{\partial w_0}{\partial x} \frac{\partial w_0}{\partial y} + \frac{2w_0}{R_{xy}}, \quad (16a)$$

$$\gamma_{xz}^{(0)} = \phi_x + \frac{\partial w_0}{\partial x} - \frac{v_0}{R_{xy}}, \quad \gamma_{yz}^{(0)} = \phi_y + \frac{\partial w_0}{\partial y} - \frac{u_0}{R_{xy}}, \quad (16b)$$

$$\varepsilon_{xx}^{(1)} = \frac{\partial \phi_x}{\partial x}, \quad \varepsilon_{yy}^{(1)} = \frac{\partial \phi_y}{\partial y}, \quad \gamma_{xy}^{(1)} = \frac{\partial \phi_x}{\partial y} + \frac{\partial \phi_y}{\partial x}. \quad (16c)$$

The relation between the stress and the strain of the k th layer FGGP reinforced rotating pretwisted composite cantilever plate are given as

$$\begin{bmatrix} \sigma_{xx}^{(k)} \\ \sigma_{yy}^{(k)} \\ \tau_{xz}^{(k)} \\ \tau_{yz}^{(k)} \\ \tau_{xy}^{(k)} \end{bmatrix} = \begin{bmatrix} Q_{11}^{(k)} & Q_{12}^{(k)} & 0 & 0 & 0 \\ Q_{21}^{(k)} & Q_{22}^{(k)} & 0 & 0 & 0 \\ 0 & 0 & Q_{44}^{(k)} & 0 & 0 \\ 0 & 0 & 0 & Q_{55}^{(k)} & 0 \\ 0 & 0 & 0 & 0 & Q_{66}^{(k)} \end{bmatrix} \begin{bmatrix} \varepsilon_{xx} \\ \varepsilon_{yy} \\ \gamma_{xz} \\ \gamma_{yz} \\ \gamma_{xy} \end{bmatrix}, \quad (17)$$

where

$$Q_{11}^{(k)} = Q_{22}^{(k)} = \frac{E_c^{(k)}}{1 - \nu_c^{(k)^2}}, \quad Q_{12}^{(k)} = Q_{21}^{(k)} = \frac{\nu_c^{(k)} E_c^{(k)}}{1 - \nu_c^{(k)^2}}, \quad Q_{44}^{(k)} = Q_{55}^{(k)} = Q_{66}^{(k)} = \frac{E_c^{(k)}}{2(1 + \nu_c^{(k)})}. \quad (18)$$

The strain energy for the FGGP reinforced rotating pretwisted composite cantilever plate is expressed as

$$\begin{aligned} U &= \iiint_V \frac{1}{2} (\sigma_{xx}^{(k)} \varepsilon_{xx} + \sigma_{yy}^{(k)} \varepsilon_{yy} + \tau_{xy}^{(k)} \gamma_{xy} + \tau_{xz}^{(k)} \gamma_{xz} + \tau_{yz}^{(k)} \gamma_{yz}) dV \\ &= \iint_S \frac{1}{2} (N_{xx} \varepsilon_{xx}^{(0)} + M_{xx} \varepsilon_{xx}^{(1)} + N_{yy} \varepsilon_{yy}^{(0)} + M_{yy} \varepsilon_{yy}^{(1)} + N_{xy} \gamma_{xy}^{(0)} + M_{xy} \gamma_{xy}^{(1)} \\ &\quad + Q_x \gamma_{xz}^{(0)} + Q_y \gamma_{yz}^{(0)}) dS, \end{aligned} \quad (19)$$

where

$$\begin{bmatrix} N_{xx} \\ N_{yy} \\ N_{xy} \end{bmatrix} = \begin{bmatrix} A_{11} & A_{12} & 0 \\ A_{21} & A_{22} & 0 \\ 0 & 0 & A_{66} \end{bmatrix} \begin{bmatrix} \varepsilon_{xx}^{(0)} \\ \varepsilon_{yy}^{(0)} \\ \gamma_{xy}^{(0)} \end{bmatrix} + \begin{bmatrix} B_{11} & B_{12} & 0 \\ B_{21} & B_{22} & 0 \\ 0 & 0 & B_{66} \end{bmatrix} \begin{bmatrix} \varepsilon_{xx}^{(1)} \\ \varepsilon_{yy}^{(1)} \\ \gamma_{xy}^{(1)} \end{bmatrix}, \quad (20a)$$

$$\begin{bmatrix} M_{xx} \\ M_{yy} \\ M_{xy} \end{bmatrix} = \begin{bmatrix} B_{11} & B_{12} & 0 \\ B_{21} & B_{22} & 0 \\ 0 & 0 & B_{66} \end{bmatrix} \begin{bmatrix} \varepsilon_{xx}^{(0)} \\ \varepsilon_{yy}^{(0)} \\ \gamma_{xy}^{(0)} \end{bmatrix} + \begin{bmatrix} D_{11} & D_{12} & 0 \\ D_{21} & D_{22} & 0 \\ 0 & 0 & D_{66} \end{bmatrix} \begin{bmatrix} \varepsilon_{xx}^{(1)} \\ \varepsilon_{yy}^{(1)} \\ \gamma_{xy}^{(1)} \end{bmatrix}, \quad (20b)$$

$$\begin{bmatrix} Q_y \\ Q_x \end{bmatrix} = K \begin{bmatrix} A_{44} & 0 \\ 0 & A_{55} \end{bmatrix} \begin{bmatrix} \gamma_{yz}^{(0)} \\ \gamma_{xz}^{(0)} \end{bmatrix}, \quad (20c)$$

$$A_{ij} = \sum_{k=1}^{N_L} \int_{z_k}^{z_{k+1}} Q_{ij}^{(k)} dz, \quad B_{ij} = \sum_{k=1}^{N_L} \int_{z_k}^{z_{k+1}} Q_{ij}^{(k)} z dz, \quad D_{ij} = \sum_{k=1}^{N_L} \int_{z_k}^{z_{k+1}} Q_{ij}^{(k)} z^2 dz, \quad (20d)$$

where the K is shear correction factor and equal to 5/6.

Considering the effect of the deformation, any point location vector of the FGGP reinforced rotating pretwisted composite cantilever plate is written as

$$\mathbf{r} = x\mathbf{i} + y \cos(\kappa x)\mathbf{j} + y \sin(\kappa x)\mathbf{k} + u\mathbf{a}_1 + v\mathbf{a}_2 + (w + z)\mathbf{a}_3$$

$$= \left(x - \frac{zy\kappa}{A} + \frac{u}{A} - \frac{y\kappa w}{A} \right) \mathbf{i} + \left(-\frac{1}{A} (z + uy\kappa + w) \sin(\kappa x) + (y + v) \cos(\kappa x) \right) \\ + \left(\frac{1}{A} (z + uy\kappa + w) \cos(\kappa x) + (y + v) \sin(\kappa x) \right) \mathbf{k}. \quad (21)$$

Considering a small periodic perturbation, the rotation speed vector $\mathbf{\Omega}$ can be derived as

$$\mathbf{\Omega} = \Omega \cos(\varphi) \mathbf{j} - \Omega \sin(\varphi) \mathbf{k}, \quad (22a)$$

$$\Omega = \Omega_0 + f \cos(\Omega_p) t, \quad (22b)$$

where Ω_0 is the steady-state rotating speed, f and Ω_p respectively represent the periodic perturbation amplitude and frequency of the rotating speed.

The total speed \mathbf{v}_T about the rotating pretwisted composite cantilever plate consists of the rotating speed component \mathbf{v}_s and deformation speed component \mathbf{v}_d . The rotating speed component \mathbf{v}_s is obtained as

$$\mathbf{v}_s = \mathbf{\Omega} \times \mathbf{r} = V_x \mathbf{i} + V_y \mathbf{j} + V_z \mathbf{k}, \quad (23)$$

where

$$V_x = \Omega \left((y + v) \sin(\kappa x + \varphi) + \frac{1}{A} (z + y\kappa w + w) \cos(\kappa x + \varphi) \right), \quad (24a)$$

$$V_y = \Omega \left(R + x - \frac{1}{A} (zy\kappa + u - y\kappa w) \right) \sin(\varphi), \quad (24b)$$

$$V_z = \Omega \left(R + x - \frac{1}{A} (zy\kappa + u - y\kappa w) \right) \cos(\varphi). \quad (24c)$$

The deformation speed component \mathbf{v}_d is given as

$$\mathbf{v}_d = \frac{d\mathbf{r}}{dt} = \frac{du}{dt} \mathbf{a}_1 + \frac{dv}{dt} \mathbf{a}_2 + \frac{dw}{dt} \mathbf{a}_3. \quad (25)$$

The total speed \mathbf{v}_T can be expressed as

$$\mathbf{v}_T = \mathbf{v}_d + \mathbf{v}_s. \quad (26)$$

Substituting equations (24) and (25) to equation (26), the components (V_1, V_2, V_3) of the total speed \mathbf{v}_T in the direction (x, y, z) are derived as

$$V_1 = \mathbf{v}_T \cdot \mathbf{a}_1 = \dot{u} + \frac{V_x}{A} - \frac{yq\Omega \cos(\kappa x + \varphi)}{A} \left(R + x - \frac{zy\kappa}{A} + \frac{u}{A} - \frac{y\kappa w}{A} \right), \quad (27a)$$

$$V_2 = \mathbf{v}_T \cdot \mathbf{a}_2 = \dot{v} - \Omega \sin(\kappa x + \varphi) \left(R + x - \frac{zy\kappa}{A} + \frac{u}{A} - \frac{y\kappa w}{A} \right), \quad (27b)$$

$$V_3 = \mathbf{v}_T \cdot \mathbf{a}_3 = \dot{w} - \frac{y\kappa V_x}{A} - \frac{\Omega \cos(\kappa x + \varphi)}{A} \left(R + x - \frac{zy\kappa}{A} + \frac{u}{A} - \frac{y\kappa w}{A} \right), \quad (27c)$$

where a point denotes the first-order derivative with respect to the time.

The kinetic energy T of the FGGP reinforced rotating pretwisted composite cantilever plate is derived as

$$\begin{aligned} T &= \iiint \sum_{k=1}^{N_L} \int_{z_k}^{z_{k+1}} \frac{1}{2} \rho_c^{(k)} V_i^2 dV \\ &= \iiint \sum_{k=1}^{N_L} \int_{z_k}^{z_{k+1}} \frac{1}{2} \rho_c^{(k)} \left(\dot{u}^2 + \dot{v}^2 + \dot{w}^2 + \Omega^2 \left(y \sin(\kappa x + \varphi) + \frac{z \cos(\kappa x + \varphi)}{A} \right. \right. \\ &\quad \left. \left. + \frac{uyq \cos(\kappa x + \varphi)}{A} + v \sin(\kappa x + \varphi) + \frac{w \cos(\kappa x + \varphi)}{A} \right)^2 + \Omega^2 \left(R + x - \frac{zy\kappa}{A} \right. \right. \\ &\quad \left. \left. + \frac{u}{A} - \frac{y\kappa w}{A} \right)^2 + 2\Omega \dot{u} \left(\frac{y \sin(\kappa x + \varphi)}{A} + \frac{z \cos(\kappa x + \varphi)}{A^2} \right) - \frac{2\Omega y\kappa \cos(\kappa x + \varphi) \dot{u}}{A} \right. \\ &\quad \left. + x - \frac{zy\kappa}{A} \right) - 2\Omega \sin(\kappa x + \varphi) \dot{v} \left(R + x - \frac{zy\kappa}{A} \right) - \frac{2\Omega y\kappa \dot{w}}{A} (y \sin(\kappa x + \varphi) \\ &\quad \left. + \frac{z \cos(\kappa x + \varphi)}{A} \right) - \frac{2\Omega \cos(\kappa x + \varphi) \dot{w}}{A} \left(R + x - \frac{zy\kappa}{A} \right) + \Omega \left(\frac{2\dot{u}v}{A} \sin(\kappa x + \varphi) \right. \\ &\quad \left. - \frac{2u\dot{v}}{A} \sin(\kappa x + \varphi) + 2\dot{u}w \cos(\kappa x + \varphi) - 2u\dot{w} \cos(\kappa x + \varphi) + \frac{2y\kappa w \dot{v}}{A} \sin(\kappa x + \varphi) \right. \\ &\quad \left. - \frac{2y\kappa \dot{w}v}{A} \sin(\kappa x + \varphi) \right) dV, \end{aligned} \quad (28)$$

The components N_{c1} , N_{c2} and N_{c3} of the centrifugal force in the directions $(\mathbf{a}_1, \mathbf{a}_2, \mathbf{a}_3)$ are obtained as

$$N_{c1} = \int_x^a \mathbf{F}_c \cdot \mathbf{a}_1 A dx, \quad N_{c2} = \int_y^{+b/2} \mathbf{F}_c \cdot \mathbf{a}_2 dy, \quad N_{c3} = \mathbf{F}_c \cdot \mathbf{a}_3, \quad (29)$$

where

$$\mathbf{F}_c = -\boldsymbol{\Omega} \times (\boldsymbol{\Omega} \times \mathbf{r}) = F_{cx} \mathbf{i} + F_{cy} \mathbf{j} + F_{cz} \mathbf{k}, \quad (30a)$$

$$F_{cx} = \rho_c^{(k)} \Omega^2 \left(R + x + \frac{zy\kappa}{A} \right), \quad (30b)$$

$$F_{cy} = \rho_c^{(k)} \Omega^2 \left(y \sin(\kappa x + \varphi) + \frac{z}{A} \cos(\kappa x + \varphi) \right) \sin(\varphi), \quad (30c)$$

$$F_{cz} = \rho_c^{(k)} \Omega^2 \left(y \sin(\kappa x + \varphi) + \frac{z}{A} \cos(\kappa x + \varphi) \right) \cos(\varphi). \quad (30d)$$

The potential energy U_p of the centrifugal force is given as

$$U_p = \iint \sum_{k=1}^{N_L} \int_{z_k}^{z_{k+1}} (N_{c1}u_1 + N_{c2}u_2 + N_{c3}u_3) dV, \quad (31)$$

where displacements u_i ($i=1, 2, 3$) of the centrifugal force [12,13] are given as

$$u_1 = u_0 + \frac{1}{2} \left(\left(\frac{\partial w_0}{\partial x} \right)^2 + \left(\frac{\partial v_0}{\partial x} \right)^2 \right), \quad (32a)$$

$$u_2 = v_0 + \frac{1}{2} \left(\left(\frac{\partial w_0}{\partial y} \right)^2 + \left(\frac{\partial u_0}{\partial y} \right)^2 \right), \quad (32b)$$

$$u_3 = w_0. \quad (32c)$$

Rayleigh dissipation function D_f on the structural damping of the rotating pretwisted composite cantilever plate is written as follows

$$D_f = \iint \frac{1}{2} \gamma \dot{w}_0^2 dS, \quad (33)$$

where γ is the damping coefficient.

The potential energy U_{in} of the non-uniform axial excitation P_{in} and energy W_F of the transverse excitation F are expressed as

$$U_{in} = \frac{1}{2} \int_v \frac{P_{in}}{h} \left(\frac{\partial w_0}{\partial x} \right)^2 dV = \int_s \frac{1}{4} (P_{\max} + P_{03}) \left(\frac{\partial w_0}{\partial x} \right)^2 dS, \quad (34a)$$

$$W_F = \int_s F w_0 dS. \quad (34b)$$

The cantilever boundary of the FGGP reinforced rotating pretwisted composite plate is clamped at the edge $x=0$ and is free at the edges $x=a$, $y=-\frac{b}{2}$ and $y=\frac{b}{2}$, namely

$$x=0: w_0 = u_0 = v_0 = \phi_x = \phi_y = \psi_x = \psi_y = 0. \quad (35)$$

The first-order bending, second-order bending and first-order torsional vibration modes are considered, as shown in Figure 4. According to reference [43], the expansion of the middle surface displacement w_0 for the rotating pretwisted composite cantilever plate is given as

$$w_0(x, y, t) = w_1(t)X_1(x)Y_1(y) + w_2(t)X_1(x)Y_2(y) + w_3(t)X_2(x)Y_1(y), \quad (36)$$

where

$$X_i(x) = \sin\left(\frac{\lambda_i x}{a}\right) - \sinh\left(\frac{\lambda_i x}{a}\right) + \alpha_i \left(\cosh\left(\frac{\lambda_i x}{a}\right) - \cos\left(\frac{\lambda_i x}{a}\right) \right), \quad (i = 1, 2), \quad (37a)$$

$$Y_1(y) = 1, \quad Y_2(y) = \sqrt{3} \left(\frac{2y}{b} \right), \quad (37b)$$

where

$$\alpha_i = \frac{\sinh \lambda_i + \sin \lambda_i}{\cosh \lambda_i + \cos \lambda_i}, \quad (i = 1, 2), \quad (38)$$

and λ_i is the solution of the equation as follows

$$\cos \lambda_i \cosh \lambda_i + 1 = 0, \quad (i = 1, 2). \quad (39)$$

The u_0 , v_0 , ϕ_x , ϕ_y , ψ_x and ψ_y are given as

$$\begin{aligned} u_0(x, y, t) = & u_1(t) \frac{\lambda_1}{a} \left[\cos\left(\frac{\lambda_1 x}{a}\right) - \cosh\left(\frac{\lambda_1 x}{a}\right) + a_1 \left(\sinh\left(\frac{\lambda_1 x}{a}\right) - \sin\left(\frac{\lambda_1 x}{a}\right) \right) \right] \\ & + u_2(t) \frac{\lambda_1}{a} \left[\cos\left(\frac{\lambda_1 x}{a}\right) - \cosh\left(\frac{\lambda_1 x}{a}\right) + a_1 \left(\sinh\left(\frac{\lambda_1 x}{a}\right) - \sin\left(\frac{\lambda_1 x}{a}\right) \right) \right] \left[\sqrt{3} \frac{2y}{b} \right] \\ & + u_3(t) \frac{\lambda_2}{a} \left[\cos\left(\frac{\lambda_2 x}{a}\right) - \cosh\left(\frac{\lambda_2 x}{a}\right) + a_2 \left(\sinh\left(\frac{\lambda_2 x}{a}\right) - \sin\left(\frac{\lambda_2 x}{a}\right) \right) \right], \end{aligned} \quad (40a)$$

$$v_0(x, y, t) = v_1(t) \left[\sin\left(\frac{\lambda_1 x}{a}\right) - \sinh\left(\frac{\lambda_1 x}{a}\right) + a_1 \left(\cosh\left(\frac{\lambda_1 x}{a}\right) - \cos\left(\frac{\lambda_1 x}{a}\right) \right) \right] \left[\sqrt{3} \left(\frac{2}{b} \right) \right], \quad (40b)$$

$$\begin{aligned} \phi_x(x, y, t) = & \phi_{x1}(t) \frac{\lambda_1}{a} \left[\cos\left(\frac{\lambda_1 x}{a}\right) - \cosh\left(\frac{\lambda_1 x}{a}\right) + a_1 \left(\sinh\left(\frac{\lambda_1 x}{a}\right) - \sin\left(\frac{\lambda_1 x}{a}\right) \right) \right] \\ & + \phi_{x2}(t) \frac{\lambda_1}{a} \left[\cos\left(\frac{\lambda_1 x}{a}\right) - \cosh\left(\frac{\lambda_1 x}{a}\right) + a_1 \left(\sinh\left(\frac{\lambda_1 x}{a}\right) - \sin\left(\frac{\lambda_1 x}{a}\right) \right) \right] \left[\sqrt{3} \frac{2y}{b} \right] \\ & + \phi_{x3}(t) \frac{\lambda_2}{a} \left[\cos\left(\frac{\lambda_2 x}{a}\right) - \cosh\left(\frac{\lambda_2 x}{a}\right) + a_2 \left(\sinh\left(\frac{\lambda_2 x}{a}\right) - \sin\left(\frac{\lambda_2 x}{a}\right) \right) \right], \end{aligned} \quad (40c)$$

$$\phi_y(x, y, t) = \phi_{y1}(t) \left[\sin\left(\frac{\lambda_1 x}{a}\right) - \sinh\left(\frac{\lambda_1 x}{a}\right) + a_1 \left(\cosh\left(\frac{\lambda_1 x}{a}\right) - \cos\left(\frac{\lambda_1 x}{a}\right) \right) \right] \left[\sqrt{3} \left(\frac{2}{b} \right) \right], \quad (40d)$$

$$\psi_x(x, y, t) = \psi_{x1}(t) \frac{\lambda_1}{a} \left[\cos\left(\frac{\lambda_1 x}{a}\right) - \cosh\left(\frac{\lambda_1 x}{a}\right) + a_1 \left(\sinh\left(\frac{\lambda_1 x}{a}\right) - \sin\left(\frac{\lambda_1 x}{a}\right) \right) \right]$$

$$\begin{aligned}
& + \psi_{x2}(t) \frac{\lambda_1}{a} \left[\cos\left(\frac{\lambda_1 x}{a}\right) - \cosh\left(\frac{\lambda_1 x}{a}\right) + a_1 \left(\sinh\left(\frac{\lambda_1 x}{a}\right) - \sin\left(\frac{\lambda_1 x}{a}\right) \right) \right] \left[\sqrt{3} \frac{2y}{b} \right] \\
& + \psi_{x3}(t) \frac{\lambda_2}{a} \left[\cos\left(\frac{\lambda_2 x}{a}\right) - \cosh\left(\frac{\lambda_2 x}{a}\right) + a_2 \left(\sinh\left(\frac{\lambda_2 x}{a}\right) - \sin\left(\frac{\lambda_2 x}{a}\right) \right) \right], \quad (40e)
\end{aligned}$$

$$\psi_y(x, y, t) = \psi_{y1}(t) \left[\sin\left(\frac{\lambda_1 x}{a}\right) - \sinh\left(\frac{\lambda_1 x}{a}\right) + a_1 \left(\cosh\left(\frac{\lambda_1 x}{a}\right) - \cos\left(\frac{\lambda_1 x}{a}\right) \right) \right] \left[\sqrt{3} \left(\frac{2}{b} \right) \right]. \quad (40f)$$

Based on Lagrange function, the governing equations of motion for the FGGP reinforced rotating pretwisted composite cantilever plate are derived as

$$\frac{d}{dt} \left(\frac{\partial T}{\partial \dot{q}_i} \right) - \frac{\partial T}{\partial q_i} + \frac{\partial U}{\partial q_i} + \frac{\partial U_p}{\partial q_i} + \frac{\partial U_{in}}{\partial q_i} + \frac{\partial D_f}{\partial \dot{q}_i} = \frac{\partial W_F}{\partial q_i}, \quad (41)$$

where $\mathbf{q}_i = [u_1(t), u_2(t), u_3(t), v_1(t), w_1(t), w_2(t), w_3(t), \phi_{x1}(t), \phi_{x2}(t), \phi_{x3}(t), \phi_{y1}(t), \psi_{x1}(t), \psi_{x2}(t), \psi_{x3}(t), \psi_{y1}(t)]^T$.

The transverse vibration is the main vibration of the rotating pretwisted composite cantilever plate. Solving equation (41) on the in-plane displacement terms u_0 , v_0 and rotatory terms ϕ_x , ϕ_y , ψ_x and ψ_y , the in-plane displacements and rotatory inertia terms are transformed into the transverse displacement w_0 . Substituting the displacements u_0 , v_0 , ϕ_x , ϕ_y , ψ_x and ψ_y into the ordinary differential equation of the transverse displacement w_0 , three-degree-of-freedom nonlinear dynamical system on the transverse vibration of the FGGP reinforced rotating pretwisted composite cantilever plate are written as

$$\begin{aligned}
& \ddot{w}_1 + \mu_{11} \dot{w}_1 + \left(n_{11} f^2 \cos^2(\Omega_p t) + n_{12} f \cos(\Omega_p t) + n_{13} P_{02} \cdot \cos(\underline{\alpha}) \right) w_1 \\
& + \left(m_{11} + n_{14} (P_{01} + 2P_{03}) \right) w_1 + \left(n_{15} f^2 \cos^2(\Omega_p t) + n_{16} f \cos(\Omega_p t) + n_{17} P_{02} \cdot \cos(\underline{\alpha}) \right) w_3 \\
& + \mu_{12} \dot{w}_3 + \left(m_{12} + n_{18} (P_{01} + 2P_{03}) \right) w_3 + m_{13} w_1 w_2 + m_{14} w_2 w_3 + m_{15} w_1^3 + m_{16} w_1^2 w_3 \\
& + m_{17} w_1 w_2^2 + m_{18} w_1 w_3^2 + m_{19} w_2^2 w_3 + m_{110} w_3^3 = m_{111} F_\tau \cdot \cos(\Omega_1 t), \quad (42a)
\end{aligned}$$

$$\begin{aligned}
& \ddot{w}_2 + \mu_{21} \dot{w}_2 + \left(n_{21} f^2 \cos^2(\Omega_p t) + n_{22} f \cos(\Omega_p t) + n_{23} P_{02} \cdot \cos(\underline{\alpha}) \right) w_2 \\
& + \left(m_{21} + n_{24} (P_{01} + 2P_{03}) \right) w_2 + m_{22} w_1^2 + m_{23} w_1 w_3 + m_{24} w_2^2 + m_{25} w_3^2 + m_{26} w_1^2 w_2 \\
& + m_{27} w_2^3 + m_{28} w_1 w_2 w_3 + m_{29} w_2 w_3^2 = m_{210} F_\tau \cdot \cos(\Omega_1 t), \quad (42b)
\end{aligned}$$

$$\ddot{w}_3 + \mu_{31} \dot{w}_1 + \left(n_{31} f^2 \cos^2(\Omega_p t) + n_{32} f \cos(\Omega_p t) + n_{33} P_{02} \cdot \cos(\underline{\alpha}) \right) w_1$$

$$\begin{aligned}
& + (m_{31} + n_{34}(P_{01} + 2P_{03}))w_1 + (n_{35}f^2 \cos^2(\Omega_p t) + n_{36}f \cos(\Omega_p t) + n_{37}P_{02} \cdot \cos(\underline{\omega}))w_3 \\
& + \mu_{32}\dot{w}_3(m_{32} + n_{38}(P_{01} + 2P_{03}))w_3 + m_{33}w_1w_2 + m_{34}w_2w_3 + m_{35}w_1^3 + m_{36}w_1^2w_3 \\
& + m_{37}w_1w_2^2 + m_{38}w_1w_3^2 + m_{39}w_2^2w_3 + m_{310}w_3^3 = m_{311}F_\tau \cdot \cos(\Omega_1 t), \tag{42c}
\end{aligned}$$

where μ_{ij} ($i=1, 2, 3, j=1, 2, 3$) are the damping coefficients, m_{ij} ($i=1, 2, 3$) ($j=1, 2, \dots, 11$) are the stiffness coefficients, and n_{ij} ($i=1, 2, 3, j=1, 2, \dots, 8$) are the excitation coefficients.

In the following analyses, we will investigate the primary resonance and nonlinear dynamic behaviors of the FGGP reinforced rotating pretwisted composite cantilever plate under the axial and transverse excitations in equation (42). The amplitude-frequency response curves, bifurcation diagrams, maximum Lyapunov exponent, phase portraits, waveforms and Poincare map are obtained by using Runge-Kutta method.

3. Amplitude-Frequency and Force- Amplitude Response Curves

Runge-Kutta methods are used to analyze the primary resonance of the FGGP reinforced rotating pretwisted composite cantilever plate under combined the external and multiple parametric excitations. Unless otherwise stated, the physical dimension and material parameters are given as follows

$$\begin{aligned}
& a = 0.28m, \quad b = 0.1m, \quad h = 0.004m, \quad \varphi = 45^\circ, \quad R = 0.1m, \quad \theta = 18^\circ, \quad \Omega_0 = 4000rpm, \\
& N = 20, \quad \rho_G = 1060kg/m^3, \quad \rho_M = 1200kg/m^3, \quad E_G = 1.01TPa, \quad E_M = 3.0GPa, \\
& \nu_M = 0.34, \quad \nu_G = 0.186, \quad f_G = 1\%, \quad l_G = 2.5\mu m, \quad w_G = 1.5\mu m, \quad h_G = 1.5nm, \\
& f = 1N, \quad \Omega_p = 191Hz, \quad \Omega_1 = 191Hz, \quad P_{01} = 1600N, \quad \underline{\omega} = 191Hz, \quad P_{02} = 4000N, \\
& P_{03} = 200N, \quad F_\tau = 7000N.
\end{aligned}$$

Figure 5(a) depicts the amplitude-frequency response curves of the X pattern graphene platelet reinforced rotating pretwisted composite cantilever plate with three different vibration modes. Ignoring the nonlinear and damping terms, and external load in equation (42), the natural frequencies are determined from the eigenvalue problem of equation (42). The ω_1 is the first-order natural frequency of the X pattern graphene platelet reinforced rotating pretwisted composite cantilever plate. The blue solid line indicates forward direction sweep frequency and the red dotted line denotes backward direction sweep frequency. It is found that the amplitudes of three different vibration

modes all increase when the primary resonance occurs and the hardening-spring characteristics of three different vibration modes exist for the X pattern graphene platelet reinforced rotating pretwisted composite cantilever plate. The amplitude is the highest value of the first-order bending vibration mode and is the lowest value of the first-order torsional vibration mode when the primary resonance of the first-order bending vibration mode occurs.

The amplitude-frequency response curves of the first-order bending vibration mode are demonstrated for the graphene platelet reinforced rotating pretwisted composite cantilever plate under three different distribution types, as shown in Figure 5(b). Obviously, the hardening-spring characteristics are kept for the graphene platelet reinforced rotating pretwisted composite cantilever plate under three different distribution types. The frequency ratio Ω_1/ω_1 reaching the peak value of the primary resonance amplitude with the O pattern distribution has the least value and with the X pattern distribution has the highest value. The amplitude of the primary resonance peak with the O pattern distribution is the largest value in forward direction sweep frequency. The amplitude of the primary resonance peak with the X pattern distribution is the smallest value in forward direction sweep frequency. It is noticed that the amplitudes of the primary resonance peak for the O and X pattern distributions are close in backward direction sweep frequency.

Figure 6(a) describes the amplitude-frequency response curves of the first-order bending vibration mode for the X pattern distribution graphene platelet reinforced rotating pretwisted composite cantilever plate under three different axial loads P_{01} . The larger the axial load P_{01} is, the earlier the primary resonance occurs. The primary resonance peak is bigger under the larger axial load P_{01} . Moreover, the system remains the hardening-spring characteristic under three different axial loads P_{01} . Figure 6(b) gives the influence of three different transverse excitations F_τ on the amplitude-frequency curves of the first-order bending vibration mode for the X pattern distribution graphene platelet reinforced rotating pretwisted composite cantilever plate. It is observed that the hardening-spring characteristics remain for the X pattern graphene platelet reinforced rotating pretwisted composite cantilever plate under three different transverse excitations F_τ . The larger the transverse excitation F_τ is, the more obvious the hard spring characteristics is. The larger transverse excitation F_τ of the system has the larger primary

resonance peak and primary resonance region.

Figure 7(a) presents the influence of three different axial excitations P_{02} on the amplitude-frequency response curves of the first-order bending vibration mode for the X pattern distribution graphene platelet reinforced rotating pretwisted composite cantilever plate. The frequency ratio Ω_1/ω_1 almost is same under three different axial excitations P_{02} when the primary resonance occurs. A hardening-spring characteristic under three different axial excitations P_{02} is obtained for the system. The larger the axial excitation P_{02} is, the bigger the primary resonance peak is. Figure 7(b) describes the amplitude-frequency response curves of the first-order bending vibration mode for the X pattern distribution graphene platelet reinforced rotating pretwisted composite cantilever plate under three different rotating speeds Ω_0 . The primary resonance peak is highest when $\Omega_0 = 4000 \text{ rpm}$ and is lowest when $\Omega_0 = 10000 \text{ rpm}$. The hardening-spring characteristics are more obvious for the lower speed. The frequency ratio Ω_1/ω_1 reaching the peak value of the primary resonance is low when the low speed Ω_0 exists.

Figure 8(a) exhibits the force-amplitude response curves of the X pattern graphene platelet reinforced rotating pretwisted composite cantilever plate with three different vibration modes. It is found that the amplitudes among three different vibration modes increase for the X pattern graphene platelet reinforced rotating pretwisted composite cantilever plate with the increase of the transverse excitations F_τ . The increase of the transverse excitation F_τ obviously affects the amplitude w_1 of the first-order bending vibration mode. The effect on the amplitude w_2 of the first-order torsional vibration mode is least. Figure 8(b) portrays the force-amplitude response curves of the first-order bending vibration for the graphene platelet reinforced rotating pretwisted composite cantilever plate under three different distribution types. It is concluded that the amplitudes increase with the increase of the transverse excitations F_τ . Obviously, when $F_\tau < 1930N$, the X pattern cantilever plate has the largest amplitude and the O pattern cantilever plate has the least amplitude. When $1930N < F_\tau < 2440N$, the U pattern cantilever plate has the largest amplitude and the O pattern cantilever plate has the least amplitude. When $2440N < F_\tau < 2540N$, the U pattern cantilever plate has the largest amplitude and the X pattern cantilever plate has the least amplitude. When $F_\tau > 2540N$, the O pattern cantilever plate has the largest amplitude and the X pattern cantilever plate has the least

amplitude.

The force-amplitude response curves of the first-order bending vibration mode are illustrated for the X pattern graphene platelet reinforced rotating pretwisted composite cantilever plate under three different axial loads P_{01} , as shown in Figure 9(a). When $F_\tau < 1600N$, the amplitudes with three different axial loads P_{01} nearly equal. When $F_\tau > 1600N$, the amplitude of the rotating pretwisted composite cantilever plate is larger with the increase of the axial loads P_{01} . Figure 9(b) demonstrates the effect of the frequency ratio ($\Omega_1/\omega_1 = 0.5, 1.0, 1.5$) on the force-amplitude response curves of the first-order bending vibration mode for the X pattern graphene platelet reinforced rotating pretwisted composite cantilever plate. When the frequency ratio $\Omega_1/\omega_1 = 1.0$, the amplitude of the rotating pretwisted composite cantilever plate is the largest value. In this case, the nonlinear characteristic of the curve is most obvious. The rotating pretwisted composite cantilever plate with the frequency ratio $\Omega_1/\omega_1 = 0.5$ has the second larger amplitude. The rotating pretwisted composite cantilever plate with the frequency ratio $\Omega_1/\omega_1 = 1.5$ has the smallest amplitude.

Figure 10(a) represents the influences of three different axial excitations P_{02} on the force-amplitude response curves of the first-order bending vibration mode for the X pattern graphene platelet reinforced rotating pretwisted composite cantilever plate. It is found that the amplitudes are closer under three different axial excitations P_{02} when $F_\tau < 1300N$. When $F_\tau > 1300N$, the amplitude is larger with the increase of the axial excitation P_{02} . Figure 10(b) describes the force-amplitude response curves of the first-order bending vibration mode for the X pattern graphene platelet reinforced rotating pretwisted composite cantilever plate with three different rotating speeds Ω_0 . It is noticed that the nonlinear characteristic is not obvious with the $\Omega_0 = 7000rpm$ and $\Omega_0 = 10000rpm$. Due to the dynamic stiffness of the rotating pretwisted composite cantilever plate, the amplitude is smaller with the increase of the rotating speed Ω_0 .

4. Effect of Axial Excitation on Nonlinear Vibrations

In this section, Runge-Kutta methods are used to analyze the nonlinear vibrations of the FGGP reinforced rotating pretwisted composite cantilever plates under combined the

external and multiple parametric excitations. The geometric and material parameters of the FGGP reinforced rotating pretwisted composite cantilever plate are listed as follows

$$\begin{aligned} a &= 0.28m, \quad b = 0.1m, \quad h = 0.004m, \quad \varphi = 45^\circ, \quad R = 0.1m, \quad \theta = 18^\circ, \quad \Omega = 4000rpm, \\ N &= 20, \quad \rho_G = 1060kg/m^3, \quad \rho_M = 1200kg/m^3, \quad E_G = 1.01TPa, \quad E_M = 3.0GPa, \\ f &= 1N, \quad \Omega_p = 191Hz, \quad v_M = 0.34, \quad v_G = 0.186, \quad f_G = 1\%, \quad l_G = 2.5\mu m, \\ w_G &= 1.5\mu m, \quad h_G = 1.5nm. P_{01} = 1600N, P_{03} = 200N. \end{aligned}$$

According to equation (42), we research the influences of the axial excitations P_{02} on the nonlinear dynamic characteristics of the FGGP reinforced rotating pretwisted composite cantilever plate with three different distribution types.

Figures 11-13 demonstrate the bifurcation diagrams and maximum Lyapunov exponent diagram of the graphene platelet reinforced rotating pretwisted composite cantilever plate with the X, U and O distribution patterns when the axial excitations P_{02} increase from $2.4 \times 10^5 N$ to $4.6 \times 10^5 N$, respectively. Figure (a) denotes the bifurcation diagram of the first-order bending vibration mode, namely, the relation of w_1 versus P_{02} . Figure (b) represents the bifurcation diagram on the relation of w_2 versus P_{02} for the first-order torsion vibration mode. Figure (c) is the bifurcation diagram on the relation of w_3 versus P_{02} for the second-order bending vibration mode. Figure (d) illustrates the relation on the maximum Lyapunov exponent versus P_{02} . The transverse excitation frequency Ω_1 and axial excitation frequency ω all are $191Hz$. The transverse excitation is $F_\tau = 7 \times 10^3 N$. The initial conditions are chosen as $w_1 = -0.0014$, $\dot{w}_1 = -0.0026$, $w_2 = -0.002$, $\dot{w}_2 = -0.0011$, $w_3 = -0.006$, $\dot{w}_3 = -0.002$ and $t = 0$. It is clearly observed that the vibration laws of the FGGP reinforced rotating pretwisted composite cantilever plates are the periodic to chaotic vibrations through twice periodic doubling bifurcations, as shown in Figures 11-13. For the cases of the U and O distribution patterns shown in Figures 12 and 13, the FGGP reinforced rotating pretwisted composite cantilever plates have a small periodic window after the chaotic vibrations. In the X distribution pattern shown in Figure 11, the periodic window does not appear in the FGGP reinforced rotating pretwisted composite cantilever plate.

Figure 11 demonstrates that in the periodic region $P_{02} \in (2.40 \times 10^5 N \sim 4.60 \times 10^5 N)$, twice period-doubling bifurcations occur for the X pattern graphene platelet reinforced rotating pretwisted composite cantilever plate when the axial excitations are

$P_{02} = 3.566 \times 10^5 N$ and $P_{02} = 3.876 \times 10^5 N$. The short chaotic vibrations appear between the periodic vibrations when the axial excitation P_{02} is around $4.0 \times 10^5 N$. When the axial excitation increases to $P_{02} = 4.20 \times 10^5 N$, the chaotic vibrations happen in the X pattern graphene platelet reinforced rotating pretwisted composite cantilever plate.

Figure 12 exhibits that through a periodic region $P_{02} \in (2.40 \times 10^5 N \sim 3.76 \times 10^5 N)$, the chaotic vibrations occur for the U pattern graphene platelet reinforced rotating pretwisted composite cantilever plate when the axial excitation is $P_{02} = 3.76 \times 10^5 N$. In addition, a short periodic window exists when $P_{02} \in (4.34 \times 10^5 N \sim 4.40 \times 10^5 N)$ in the chaotic region, which is denoted by a red circle. In the periodic region $P_{02} \in (2.40 \times 10^5 N \sim 3.76 \times 10^5 N)$, twice period-doubling bifurcations happen in the U pattern graphene platelet reinforced rotating pretwisted composite cantilever plate when the $P_{02} = 3.22 \times 10^5 N$ and $P_{02} = 3.58 \times 10^5 N$.

It is seen from Figure 13 that the periodic regions of the O pattern graphene platelet reinforced rotating pretwisted composite cantilever plate are respectively located in $P_{02} \in (2.40 \times 10^5 N \sim 3.40 \times 10^5 N)$ and $P_{02} \in (3.94 \times 10^5 N \sim 4.07 \times 10^5 N)$. The chaotic regions of the O pattern graphene platelet reinforced rotating pretwisted composite cantilever plate are respectively located in $P_{02} \in (3.40 \times 10^5 N \sim 3.94 \times 10^5 N)$ and $P_{02} \in (4.07 \times 10^5 N \sim 4.60 \times 10^5 N)$. The periodic region between two chaotic vibration regions in $P_{02} \in (3.94 \times 10^5 N \sim 4.07 \times 10^5 N)$ is indicated by a green circle. When the axial excitations respectively are $P_{02} = 2.86 \times 10^5 N$ and $P_{02} = 3.24 \times 10^5 N$, there are two periodic doubling bifurcation windows in the bifurcation diagram. Lyapunov exponent shown in Figure 13(d) completely corresponds to the nonlinear vibrations in the bifurcation diagrams for the O pattern graphene platelet reinforced rotating pretwisted composite cantilever plate.

Based on the aforementioned analyses, it is found that the stiffness of the X pattern graphene platelet reinforced rotating pretwisted composite cantilever plate is greater than that of the U pattern distribution thin plate. The stiffness of the U pattern graphene platelet reinforced rotating pretwisted composite cantilever plate is greater than that of the O pattern distribution thin plate. Therefore, it is observed from Figures 11-13 that the nonlinear vibrations of the O pattern graphene platelet reinforced rotating pretwisted

composite cantilever plate have the largest amplitude. The nonlinear vibrations of the U pattern distribution graphene platelet reinforced rotating pretwisted composite cantilever plate have the second larger amplitude. The nonlinear vibrations of the X pattern graphene platelet reinforced rotating pretwisted composite cantilever plate are of the smallest amplitude.

Figure 14 plots the chaotic vibrations of the X pattern graphene platelet reinforced rotating pretwisted composite cantilever plate when the axial excitation is $P_{02} = 4.40 \times 10^5 N$. Figures (a), (c) and (e) respectively represent the phase portraits on the planes (w_1, \dot{w}_1) , (w_2, \dot{w}_2) and (w_3, \dot{w}_3) . Figures (b), (d) and (f) respectively give the waveforms of the first-order bending, first-order torsional and second-order bending vibration modes on the planes (t, w_1) , (t, w_2) and (t, w_3) . Figure (g) demonstrates three-dimensional phase portrait in the space (w_1, w_2, w_3) . Figure (h) denotes Poincare map of the first-order bending vibration mode. Figure 15 illustrates the chaotic vibrations of the O pattern graphene platelet reinforced rotating pretwisted composite cantilever plate when the axial excitation is $P_{02} = 4.40 \times 10^5 N$. We obtain a conclusion from Figures 14 and 15 that the amplitudes w_1 and w_3 of the bending vibration modes are larger than the amplitude w_2 of the torsional vibration mode in the graphene platelet reinforced rotating pretwisted composite cantilever plate.

5. Effect of Transverse Excitation on Nonlinear Vibrations

We investigate the effects of the transverse excitations F_τ on the nonlinear dynamic characteristics of the FGGP reinforced rotating pretwisted composite cantilever plate under three different distribution types.

Figures 16-18 respectively depict the bifurcation diagrams and maximum Lyapunov exponent of the FGGP reinforced rotating pretwisted composite cantilever plates with the X, U and O distribution patterns when the transverse excitations F_τ increase from $1.00 \times 10^5 N$ to $1.30 \times 10^5 N$. Figure (a) denotes the bifurcation diagram of the first-order bending vibration mode, namely, the relation of w_1 versus F_τ . Figure (b) represents the bifurcation diagram of the first-order torsion vibration mode, namely, the relation of w_2 versus F_τ . Figure (c) is the bifurcation diagram of the second-order bending vibration

mode, namely, the relation of w_3 versus F_τ . Figure (d) illustrates the maximum Lyapunov exponent diagram of the FGGP reinforced rotating pretwisted composite cantilever plate. The transverse excitation frequency Ω_1 and axial excitation frequency ω all are 318.3Hz . The axial excitation P_{02} is $2 \times 10^3 N$. The initial conditions are chosen as $w_1 = -0.0014$, $\dot{w}_1 = -0.0026$, $w_2 = -0.002$, $\dot{w}_2 = -0.0011$, $w_3 = -0.006$, $\dot{w}_3 = -0.002$ and $t = 0$. The vibration laws of the X, U and O distribution patterns for the FGGP reinforced rotating pretwisted composite cantilever plate are demonstrated as follows, the periodic vibration \rightarrow periodic doubling bifurcation \rightarrow chaotic vibrations.

It is observed from Figure 16 that the nonlinear vibrations of the X pattern graphene platelet reinforced rotating pretwisted composite cantilever plate vary from the periodic to chaotic vibrations when the transverse excitation is $F_\tau = 1.18 \times 10^5 N$. The periodic doubling bifurcation occurs in the periodic region $F_\tau \in (1.00 \times 10^5 N \sim 1.18 \times 10^5 N)$ when the transverse excitation increases to $F_\tau = 1.12 \times 10^5 N$. It is noticed that a quasi-periodic region $F_\tau \in (1.238 \times 10^5 N \sim 1.274 \times 10^5 N)$ exists in the X pattern graphene platelet reinforced rotating pretwisted composite cantilever plate after the chaotic vibrations happen, which is indicated by a blue circle.

When the transverse excitation increases to $F_\tau = 1.21 \times 10^5 N$, it is found from Figure 17 that the nonlinear vibrations change from the periodic to chaotic vibrations in the U pattern graphene platelet reinforced rotating pretwisted composite cantilever plate. The periodic doubling bifurcation happens when $F_\tau = 1.158 \times 10^5 N$. Figure 18 demonstrates that through a periodic region $F_\tau \in (1.00 \times 10^5 N \sim 1.23 \times 10^5 N)$, the chaotic vibrations appear in the U pattern graphene platelet reinforced rotating pretwisted composite cantilever plate when $F_\tau = 1.232 \times 10^5 N$. A periodic doubling bifurcation again happens in the FGGP reinforced rotating pretwisted composite cantilever plate when the transverse excitation is $F_\tau = 1.196 \times 10^5 N$.

It is seen from Figures 19-20 that the amplitudes of the nonlinear vibrations have little difference for the FGGP reinforced rotating pretwisted composite cantilever plate with the U and O distribution patterns when the transverse excitations F_τ increase from $1.00 \times 10^5 N$ to $1.30 \times 10^5 N$. Figure 19 illustrates the chaotic vibrations of the U pattern graphene platelet reinforced rotating pretwisted composite cantilever thin plate when the

transverse excitation is $F_\tau = 1.25 \times 10^5 N$. Figures (a), (c) and (e) respectively denote the phase portraits on the planes (w_1, \dot{w}_1) , (w_2, \dot{w}_2) and (w_3, \dot{w}_3) . Figure (b), (d) and (f) respectively gives the waveforms of the first-order bending, first-order torsional and second-order bending vibration modes on the plane (t, w_1) , (t, w_2) and (t, w_3) . Figure (g) illustrates three-dimensional phase portrait in the space (w_1, w_2, w_3) . Figure (h) is Poincare map of the first-order bending vibration mode. Figures 20 demonstrates the chaotic vibrations of the O pattern graphene platelet reinforced rotating pretwisted composite cantilever thin plates when the transverse excitations all are $F_\tau = 1.25 \times 10^5 N$. It is found from Figures 19 and 20 that the relationships among the amplitudes w_1 , w_2 and w_3 are similar to the results obtained in Figures 14-15 for the FGGP reinforced rotating pretwisted composite cantilever plate under combined the external and multiple parametric excitations.

6. Conclusions

The primary resonance and nonlinear vibrations are investigated for the FGGP reinforced rotating pretwisted composite cantilever plate under combined the external and multiple parametric excitations. Utilizing von-Karman nonlinear geometric relationship and Lagrange equation, three-degree-of-freedom nonlinear governing equations of motion are obtained. The primary resonance and nonlinear dynamic behaviors are analyzed by Runge Kutta method. The hardening-spring characteristics are found for the graphene platelet reinforced rotating pretwisted composite cantilever plate. The primary resonant amplitude of the O pattern distribution plate reaches the peak firstly and is largest. The vibration amplitude of the X pattern distribution plate reaches the peak latest and is minimum. The primary resonant amplitude of the X pattern distribution plate reaches the peak earlier and is larger with the increase of the axial loads P_{01} . The larger the transverse excitation F_τ is, the more obvious the hardening-spring characteristics is.

With the increase of the axial excitations P_{02} , the bigger primary resonant peak occurs. The primary resonant amplitude of the X pattern distribution plate reaches the peak later and is larger with the decrease of the rotating speed Ω_0 . For the force-amplitude response curves, when $F_\tau > 2540N$, the O pattern rotating pretwisted

composite cantilever plate has the largest amplitude and X pattern rotating pretwisted composite cantilever plate has the least amplitude. When $F_{\tau} > 1300N$, the amplitude is larger with the increase of the axial excitations P_{01} and P_{02} . The amplitude of the X pattern distribution plate is larger with the decrease of the rotating speed Ω_0 . When the frequency ratio $\Omega_1/\omega_1 = 1.0$ or rotating speed $\Omega_0 = 4000rpm$, the nonlinear characteristic of the curve is obvious.

When the axial excitations P_{02} increase from $2.4 \times 10^5 N$ to $4.6 \times 10^5 N$, the FGGP reinforced rotating pretwisted composite cantilever plate under the transverse excitation has the chaotic vibrations through twice periodic doubling bifurcations. When the transverse excitations F_{τ} increase from $1.00 \times 10^5 N$ to $1.30 \times 10^5 N$, the FGGP reinforced rotating pretwisted composite cantilever plate under the axial excitation has the chaotic vibrations through once periodic doubling bifurcation. When the transverse excitations F_{τ} increase from $1.00 \times 10^5 N$ to $1.30 \times 10^5 N$, the amplitudes of the nonlinear vibrations for the X, U and O pattern graphene platelet reinforced rotating pretwisted composite cantilever plate have little difference.

When the axial excitations P_{02} increase from $2.4 \times 10^5 N$ to $4.6 \times 10^5 N$, the nonlinear vibrations of the O pattern graphene platelet reinforced rotating pretwisted composite cantilever plate have the largest amplitude. The nonlinear vibrations of the U pattern graphene platelet reinforced rotating pretwisted composite cantilever plate have the second larger amplitude. The nonlinear vibrations of the X pattern graphene platelet reinforced rotating pretwisted composite cantilever plate have the smallest amplitude.

Acknowledgements

The authors gratefully acknowledge the support of National Natural Science Foundation of China (NNSFC) through Grant Nos. 11832002, 11672188 and 11427801, the Funding Project for Academic Human Resources Development in Institutions of Higher Learning under the Jurisdiction of Beijing Municipality (PHRIHLB).

Declaration on Conflict of Interest

The authors declare that there is no conflict of interest regarding the publication of

this paper.

References

1. J. Yang, H. Wu and S. Kitipornchai, Buckling and postbuckling of functionally graded multilayer graphene platelets platelet-reinforced composite beams, *Composite Structures* 161, p111-118, 2016.
2. D. Chen, J. Yang, and S. Kitipornchai, Nonlinear vibration and postbuckling of functionally graded graphene reinforced porous nanocomposite beams, *Composites Science and Technology* 142, pp235-245, 2017.
3. Y. Kiani, Isogeometric large amplitude free vibration of graphene platelets reinforced laminated plates in thermal environment using NURBS formulation, *Computer Methods in Applied Mechanics and Engineering* 332, p86-101, 2018.
4. J. J. Mao and W. Zhang, Linear and nonlinear free and forced vibrations of graphene platelets reinforced piezoelectric composite plate under external voltage excitation, *Composite Structures* 203, p551-565, 2018.
5. J. J. Mao and W. Zhang, Buckling and post-buckling analyses of functionally graded graphene platelets reinforced piezoelectric plate subjected to electric potential and axial forces, *Composite Structures* 216, p392-405, 2019.
6. A. W. Wang, H. Y. Chen, Y. X. Hao, and W. Zhang, Vibration and bending behavior of functionally graded nanocomposite doubly-curved shallow shells reinforced by graphene nanoplatelets, *Results in Physics* 9, p550-559, 2018.
7. Z. Zhao, C. Feng, Y. H. Dong, Y. Wang and J. Yang, Geometrically nonlinear bending of functionally graded nanocomposite trapezoidal plates reinforced with graphene platelets (GPLs), *International Journal of Mechanics and Materials in Design*, p1-10, 2019.
8. M. Tam, Z. Yang, S. Zhao, H. Zhang, Y. Zhang, and J. Yang, Nonlinear bending of elastically restrained functionally graded graphene nanoplatelet reinforced beams with an open edge crack, *Thin-Walled Structures* 156, 106972, 2020.
9. K. Gupta and J. S. Rao, Torsional vibrations of pretwisted cantilever plates, *Journal of Mechanical Design, Transactions of the ASME* 100, p528-534, 1978.
10. L. W. Chen and C. L. Chen, Vibration and stability of cracked thick rotating blades, *Composite Structures* 28, p67-74, 1988.
11. J. Sun, L. Kari, and I. Lopez Arteaga, A dynamic rotating blade model at an arbitrary

- stagger angle based on classical plate theory and the Hamilton's principle, *Journal of Sound and Vibration*, 332, p1355-1371, 2013.
12. J. Sun, I. L. Arteaga, and L. Kari, General shell model for a rotating pretwisted blade, *Journal of Sound and Vibration* 332, 22, p5804-5820, 2013.
 13. D. X. Cao, B. Y. Liu, M. M. Yao and W. Zhang, Free vibration analysis of a pretwisted sandwich blade with thermal barrier coatings layers, *Science China-technological Sciences* 60, p1747-1761, 2017.
 14. L. T. Liu, Y. X. Hao, W. Zhang and J. Chen, Free vibration analysis of rotating pretwisted functionally graded sandwich blades, *International Journal of Aerospace Engineering*, p1-18, 2018.
 15. Y. Oh and H. H. Yoo, Vibration analysis of a rotating pre-twisted blade considering the coupling effects of stretching , bending , and torsion, *Journal of Sound and Vibration* 431, p20–39, 2018.
 16. X. J. Gu, Y. X. Hao, W. Zhang, L. T. Liu and J. Chen, Free vibration of rotating cantilever pretwisted panel with initial exponential function type geometric imperfection, *Applied Mathematical Modelling* 68, p327-352, 2019.
 17. Y. Niu, W. Zhang and X. Y. Guo, Free vibration of rotating pretwisted functionally graded composite cylindrical panel reinforced with graphene platelets, *European Journal of Mechanics /A Solids* 77, 103798, 2019.
 18. W. Zhang, Y. Niu and K. behdinin, vibration characteristics of rotating pretwisted composite tapered blade with graphene platelets coating layers, *Aerospace Science and Technology* 98, 105644, 2019.
 19. V. Ondra and B. Titurus, Free vibration analysis of a rotating pre-twisted beam subjected to tendon-induced axial loading, *Journal of Sound and Vibration* 461, 114912, 2019.
 20. X. J. Gu, Y. X. Hao, W. Zhang, and J. Chen, Dynamic stability of rotating cantilever composite thin walled twisted plate with initial geometric imperfection under in-plane load, *Thin-Walled Structures* 144, 106267, 2019.
 21. T. Y. Zhao, L. P. Jiang, H. G. Pan, J. Yang and S. Kitipornchai, Coupled free vibration of a functionally graded pre-twisted blade-shaft system reinforced with graphene nanoplatelets, *Composite Structures* 262, 113362, 2021.
 22. P. Maji and B. N. Singh, Free vibration responses of 3D braided rotating cylindrical shells based on third-order shear deformation, *Composite Structures*, 113255, 2020.
 23. C. Li and H. Cheng, Free vibration analysis of a rotating varying-thickness-twisted

- blade with arbitrary boundary conditions, *Journal of Sound and Vibration*, 492, 115791, 2021.
24. R. Xiang, Z. Z. Pan, H. Ouyang and L. W. Zhang, A study of the vibration and lay-up optimization of rotating cross-ply laminated nanocomposite blades, *Composite Structures* 235, 111775, 2020.
 25. K. V. Avramov, O. S. Galas, O. K. Morachkovskii and C. Pierre, Analysis of flexural-flexural-torsional nonlinear vibrations of twisted rotating beams with cross-sectional deplanation, *Strength of Materials* 41, p200-208, 2009.
 26. F. X. Wang and W. Zhang, Stability analysis of a nonlinear rotating blade with torsional vibrations, *Journal of Sound and Vibration* 331, p5755-5773, 2012.
 27. H. Arvin, W. Lacarbonara, and F. Bakhtiari-Nejad, A geometrically exact approach to the overall dynamics of elastic rotating blades - part 2: Flapping nonlinear normal modes, *Nonlinear Dynamics* 70, p2279-2301, 2012.
 28. M. H. Yao, Y. P. Chen and W. Zhang, Nonlinear vibrations of blade with varying rotating speed, *Nonlinear Dynamics* 68, p487-504, 2012.
 29. F. Bekhoucha, S. Rechak, L. Duigou, and J. M. Cadou, Nonlinear forced vibrations of rotating anisotropic beams, *Nonlinear Dynamics* 74, p1281-1296, 2013.
 30. H. Arvin and W. Lacarbonara, A fully nonlinear dynamic formulation for rotating composite beams: Nonlinear normal modes in flapping, *Composite Structures* 109, p93-105, 2014.
 31. M. H. Yao, W. Zhang and Y.P. Chen, Analysis on nonlinear oscillations and resonant responses of a compressor blade, *Acta Mechanica* 225, p3483-3510, 2014.
 32. B. Zhang and Y. Li, Nonlinear vibration of rotating pre-deformed blade with thermal gradient, *Nonlinear Dynamics* 86, p459-478, 2016.
 33. D. Wang, Y. S. Chen, Z. F. Hao, and Q. J. Cao, Bifurcation analysis for vibrations of a turbine blade excited by air flows, *Science China Technological Sciences* 59, p1217-1231, 2016.
 34. P. A. Roy and S. A. Meguid, Nonlinear transient dynamic response of a blade subject to a pulsating load in a decaying centrifugal force field, *International Journal of Mechanics and Materials in Design* 14, p709-728, 2018.
 35. B. Bai, H. Li, W. Zhang and Y. C. Cui, Application of extremum response surface method-based improved substructure component modal synthesis in mistuned turbine bladed disk, *Journal of Sound and Vibration* 472, 115210, 2020.
 36. M. H. Yao, Y. Niu and Y. X. Hao, Nonlinear dynamic responses of rotating pretwisted

- cylindrical shells, *Nonlinear Dynamics* 95, p151-174, 2019.
37. W. Zhang, G. Liu, and B. Siriguleng, Saturation phenomena and nonlinear resonances of rotating pretwisted laminated composite blade under subsonic air flow excitation, *Journal of Sound and Vibration* 478, 115353, 2020.
 38. Y. Niu, M. H. Yao, and W. Zhang, Nonlinear transient responses of rotating twisted FGM cylindrical panels, *Science China Technological Sciences* 64(2), p317-330, 2020.
 39. Y. F. Zhang, Y. Niu, and W. Zhang, Nonlinear vibrations and internal resonance of pretwisted rotating cantilever rectangular plate with varying cross-section and aerodynamic force, *Engineering Structures* 225, 111259, 2020.
 40. Y. X. Hao, X. J. Gu, W. Zhang, and J. Chen, Transient response of high dimensional nonlinear dynamic system for a rotating cantilever twisted plate, *Advances in Applied Mathematics and Mechanics* 12, p1542-1564, 2020.
 41. B. Zhang, H. Ding and L. Q. Chen, Super-harmonic resonances of a rotating pre-deformed blade subjected to gas pressure, *Nonlinear Dynamics* 98, p 2531-2549, 2019.
 42. J. D. Denton, Loss mechanisms in turbo machines, *ASME Journal of Turbo machinery* 115(4), p.621–656, 1993.
 43. W. Zhang, M. H. Zhao and X. Y. Guo, Nonlinear responses of a symmetric cross-ply composite laminated cantilever rectangular plate under in-plane and moment excitations, *Composite Structures* 100, p554-565, 2013.

Figure Captions

- Figure 1 The dynamic model of the functionally graded graphene platelet (FGGP) reinforced rotating pretwisted composite blade under the axial and transverse excitations is given, (a) model, (b) cantilever plate model and coordinate systems.
- Figure 2 The sketch map of the airflow and axial load on the tip clearance of the blade is given, (a) airflow passes through tip clearance, (b) distribution for axial load in tip clearance
- Figure 3 The sketch map of different graphene platelet distribution types is obtained.
- Figure 4 The first third vibration mode shapes are obtained for the FGGP reinforced rotating pretwisted composite cantilever rectangular plate, (a) first-order bending vibration mode, (b) first-order torsional vibration mode, (c) second-order bending vibration mode.
- Figure 5 The amplitude-frequency response curves are obtained for the graphene platelet reinforced rotating pretwisted composite cantilever plate with three different vibration modes and three different distribution types, (a) amplitude-frequency response curves of X pattern graphene platelet reinforced plate with three different vibration modes, (b) amplitude-frequency response curves of first-order bending vibration with three different distribution types.
- Figure 6 The amplitude-frequency response curves of the first-order bending vibration mode are depicted for the X pattern distribution graphene platelet reinforced rotating pretwisted composite cantilever plate with three different axial load P_{01} and three different transverse excitations F_{τ} , (a) amplitude-frequency response curves with three different axial load P_{01} , (b) amplitude-frequency response curves with three different transverse excitations F_{τ} .
- Figure 7 The amplitude-frequency response curves of the first-order bending vibration mode are given for the X distribution graphene platelet reinforced rotating pretwisted cantilever plate with three different axial excitations P_{02} and three different rotating speeds Ω_0 , (a) amplitude-frequency response curves with three different axial excitations P_{02} , (b) amplitude-frequency response

curves with three different rotating speeds Ω_0 .

Figure 8 The force-amplitude response curves are obtained for the graphene platelet reinforced rotating pretwisted composite cantilever plate with three different vibration modes and three different distribution types, (a) force-amplitude response curves of X pattern graphene platelet reinforced plate with three different vibration modes, (b) force-amplitude response curves of first-order bending vibration mode with three different distribution types.

Figure 9 The force-amplitude response curves of the first-order bending vibration mode are depicted for the X distribution graphene platelet reinforced rotating pretwisted cantilever plate with three different axial loads P_{01} and three different frequency ratios $(\Omega_1/\omega_1 = 0.5, 1.0, 1.5)$, (a) force-amplitude response curves with three different axial loads P_{01} , (b) force-amplitude response curves with three different frequency ratios $(\Omega_1/\omega_1 = 0.5, 1.0, 1.5)$.

Figure 10 The force-amplitude response curves of the first-order bending vibration mode are obtained for the X distribution graphene platelet reinforced rotating pretwisted cantilever plate with three different axial excitations P_{02} and three different rotating speeds Ω_0 , (a) force-amplitude response curves with three different axial excitations P_{02} , (b) force-amplitude response curves with three different rotating speeds Ω_0 .

Figure 11 The bifurcation diagram and maximum Lyapunov exponent are depicted for the X distribution graphene platelet reinforced rotating pretwisted cantilever plate when the axial excitations P_{02} increase from $2.4 \times 10^5 N$ to $4.6 \times 10^5 N$ and transverse excitation is $F_\tau = 7 \times 10^3 N$, (a) bifurcation diagram of first-order bending vibration mode, (b) bifurcation diagram of first-order torsional vibration mode, (c) bifurcation diagram of second-order bending vibration mode, (d) maximum Lyapunov exponent diagram of first-order bending vibration mode.

Figure 12 The bifurcation diagram and maximum Lyapunov exponent of the U pattern graphene platelet reinforced rotating pretwisted composite cantilever plate are shown when the axial excitations P_{02} increase from $2.4 \times 10^5 N$ to $4.6 \times 10^5 N$ and transverse excitation is $F_\tau = 7 \times 10^3 N$, (a) bifurcation

diagram of the first-order bending vibration mode, (b) bifurcation diagram of the first-order torsional vibration mode, (c) bifurcation diagram of the second-order bending vibration mode, (d) maximum Lyapunov exponent diagram of first-order bending vibration mode.

Figure 13 The bifurcation diagram and maximum Lyapunov exponent of the O pattern graphene platelet reinforced rotating pretwisted composite cantilever plate are indicated when the axial excitations P_{02} increases from $2.4 \times 10^5 N$ to $4.6 \times 10^5 N$ and transverse excitation is $F_\tau = 7 \times 10^3 N$, (a) bifurcation diagram of the first-order bending vibration mode, (b) bifurcation diagram of the first-order torsional vibration mode, (c) bifurcation diagram of the second-order bending vibration mode, (d) maximum Lyapunov exponent diagram of first-order bending vibration mode.

Figure 14 The chaotic vibrations of the X pattern graphene platelet reinforced rotating pretwisted composite cantilever plate are obtained when the axial excitation is $P_{02} = 4.4 \times 10^5 N$ and transverse excitation is $F_\tau = 7 \times 10^3 N$, (a), (c) and (e) phase portraits on planes (w_1, \dot{w}_1) , (w_2, \dot{w}_2) and (w_3, \dot{w}_3) , (b), (d) and (f) waveforms of first-order bending, first-order torsional and second-order bending vibration modes, (g) three-dimensional phase portrait in space (w_1, w_2, w_3) , (h) Poincare map of first-order bending vibration mode.

Figure 15 The chaotic vibrations of the O pattern graphene platelet reinforced rotating pretwisted composite cantilever plate are depicted when the axial excitation is $P_{02} = 4.4 \times 10^5 N$ and transverse excitation is $F_\tau = 7 \times 10^3 N$.

Figure 16 The bifurcation diagram and maximum Lyapunov exponent of the X pattern graphene platelet reinforced rotating pretwisted composite cantilever plate are obtained when the transverse excitations F_τ increase from $1.0 \times 10^5 N$ to $1.3 \times 10^5 N$ and axial excitation P_{02} is $4 \times 10^2 N$, (a) bifurcation diagram of the first-order bending vibration mode, (b) bifurcation diagram of the first-order torsional vibration mode, (c) bifurcation diagram of the second-order bending vibration mode, (d) maximum Lyapunov exponent diagram of first-order bending vibration mode.

Figure 17 The bifurcation diagram and maximum Lyapunov exponent of the U pattern graphene platelet reinforced rotating pretwisted cantilever plate are illustrated

when the transverse excitations F_τ increase from $1.0 \times 10^5 N$ to $1.3 \times 10^5 N$ and axial excitation P_{02} is $4 \times 10^2 N$, (a) bifurcation diagram of the first-order bending vibration mode, (b) bifurcation diagram of the first-order torsional vibration mode, (c) bifurcation diagram of the second-order bending vibration mode, (d) maximum Lyapunov exponent diagram of first-order bending vibration mode.

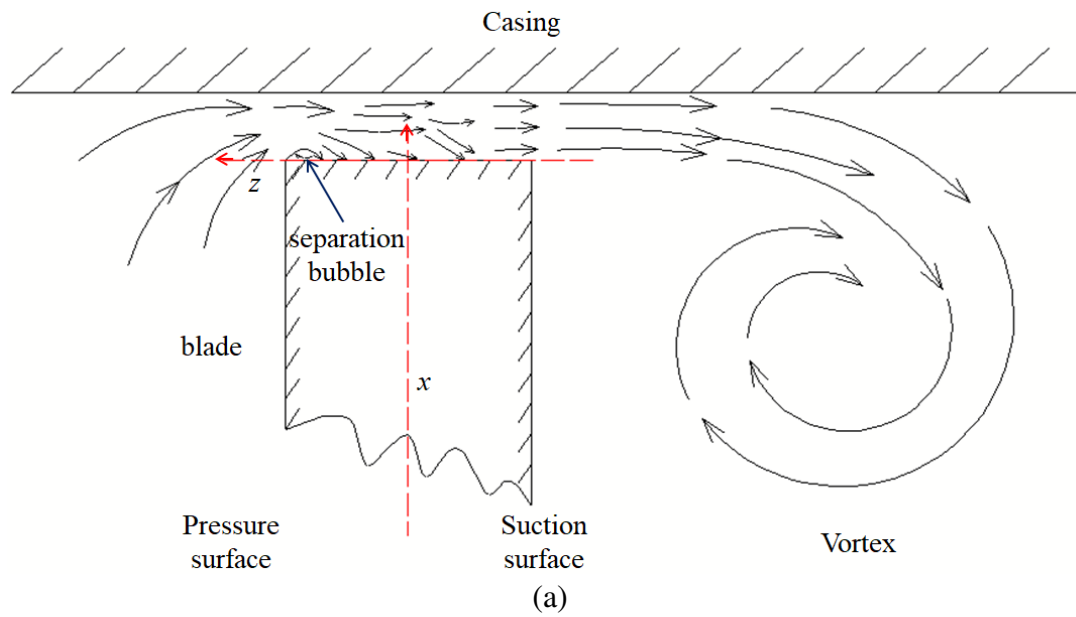
Figure 18 The bifurcation diagram and maximum Lyapunov exponent of the O pattern graphene platelet reinforced rotating pretwisted composite cantilever plate are shown when the transverse excitations F_τ increases from $1.0 \times 10^5 N$ to $1.3 \times 10^5 N$ and axial excitation P_{02} is $4 \times 10^2 N$, (a) bifurcation diagram of the first-order bending vibration mode, (b) bifurcation diagram of the first-order torsional vibration mode, (c) bifurcation diagram of the second-order bending vibration mode, (d) maximum Lyapunov exponent diagram of first-order bending vibration mode.

Figure 19 The chaotic vibrations of the U pattern graphene platelet reinforced rotating pretwisted composite cantilever plate are obtained when the transverse excitation is $F_\tau = 1.25 \times 10^5 N$ and axial excitation P_{02} is $4 \times 10^2 N$, (a), (c) and (e) phase portraits on the planes (w_1, \dot{w}_1) , (w_2, \dot{w}_2) and (w_3, \dot{w}_3) , (b), (d) and (f) waveforms of first-order bending, first-order torsional and second-order bending vibration modes, (h) three-dimensional phase portrait in space (w_1, w_2, w_3) , (f) Poincare map of first-order bending vibration mode.

Figure 20 The chaotic vibrations of the O pattern graphene platelet reinforced rotating pretwisted composite cantilever plate are given when the transverse excitation is $F_\tau = 1.25 \times 10^5 N$ and axial excitation P_{02} is $2 \times 10^2 N$.



35



The maximum amplitude
of axial excitation
 $P_{\max} = P_{01} + P_{02} \cos(\omega t) + P_{03}$

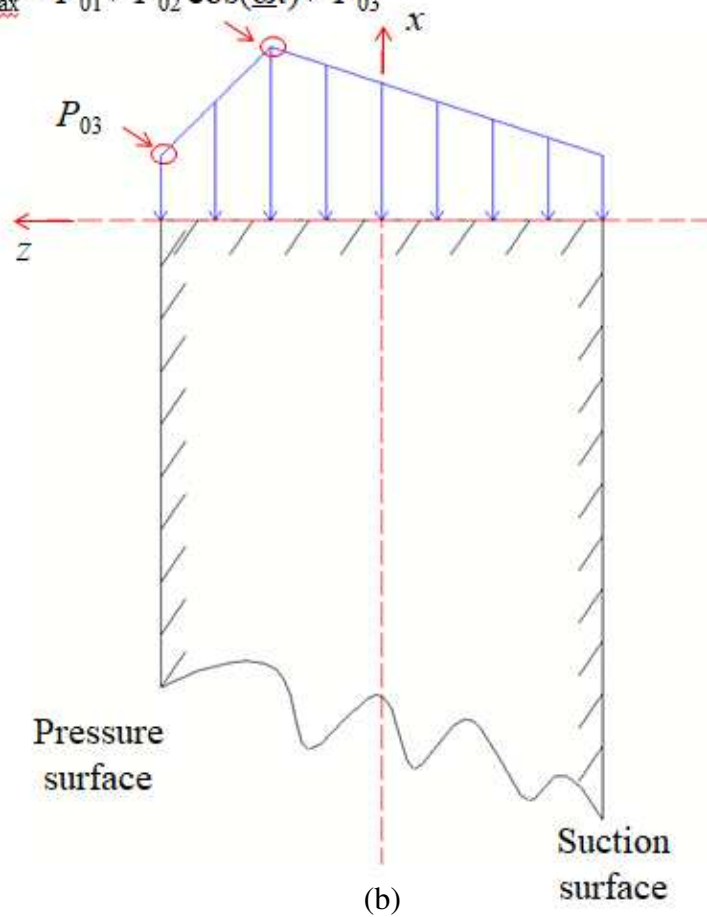
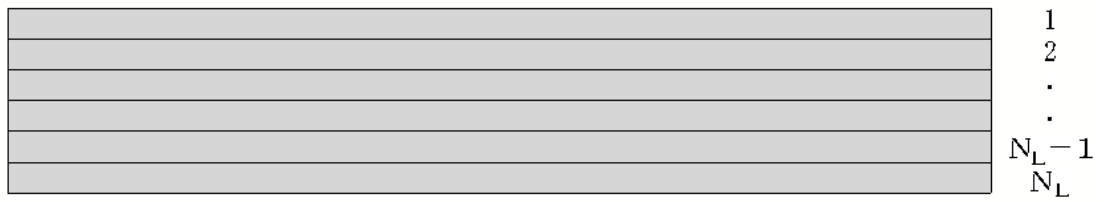
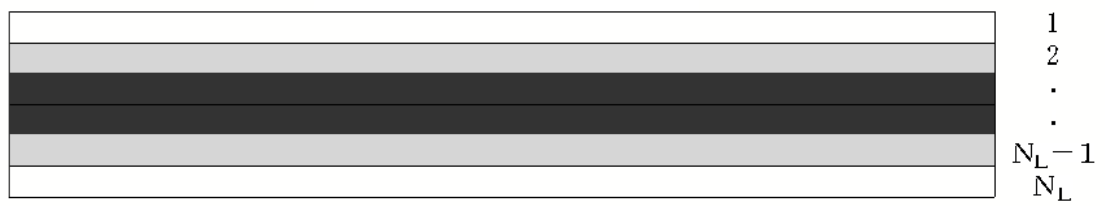


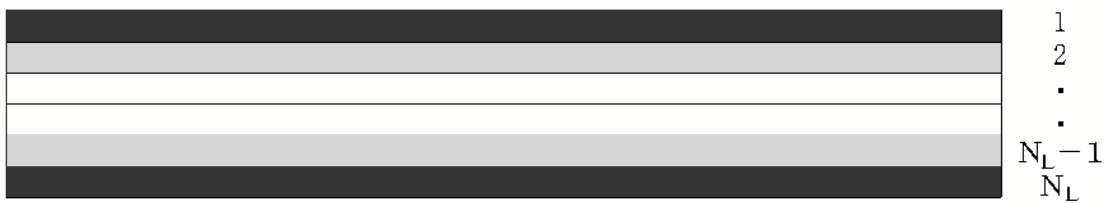
Figure 2



(a) U Pattern

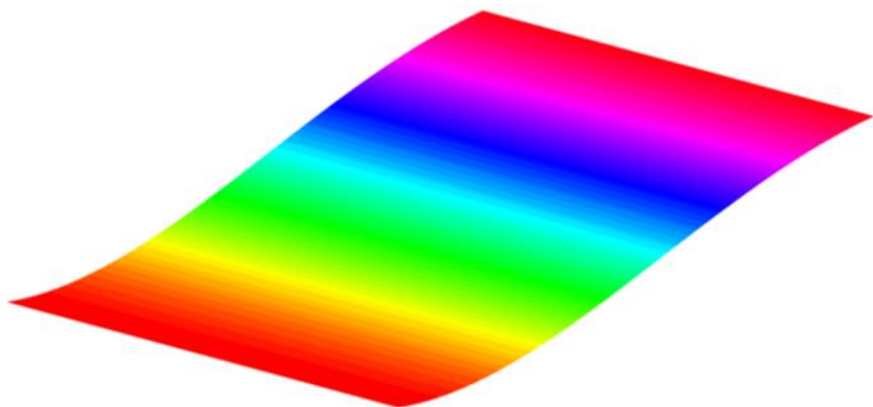


(b) O Pattern

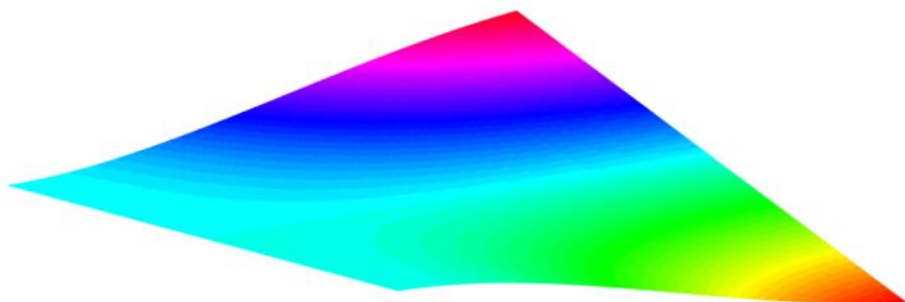


(c) X Pattern

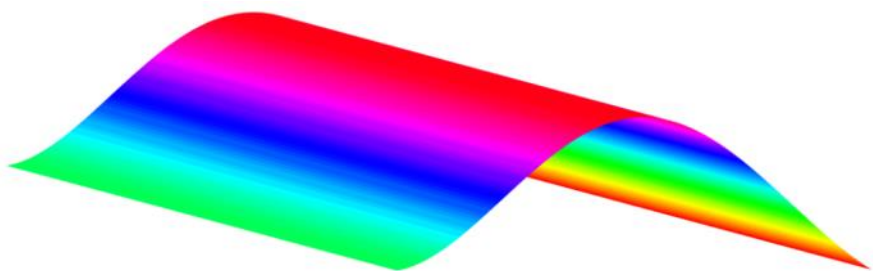
Figure 3



(a)

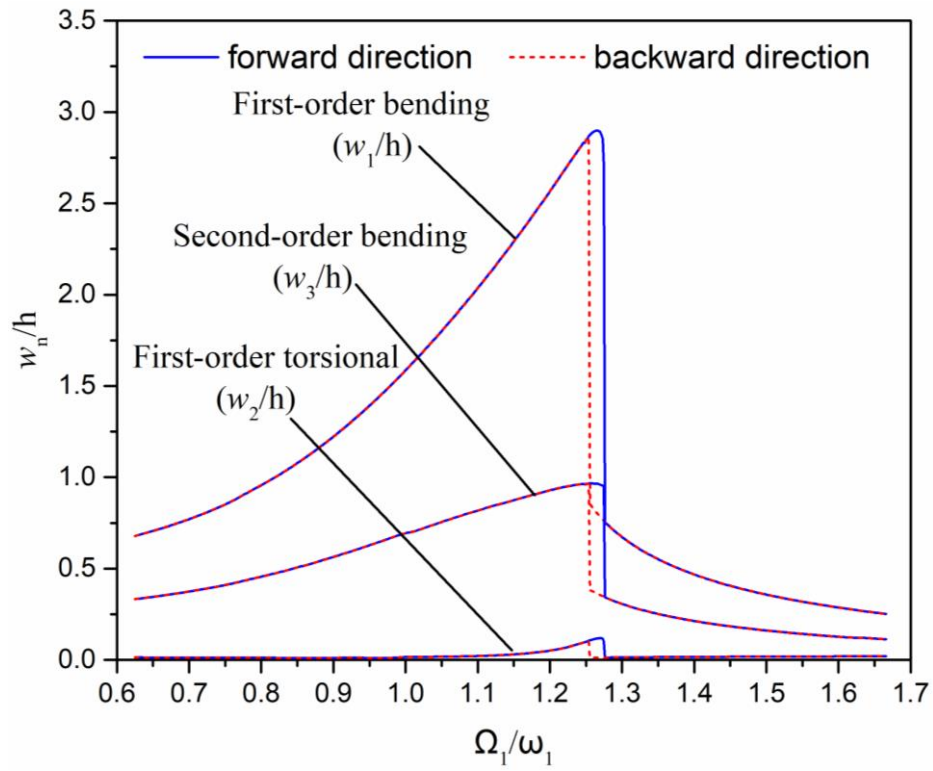


(b)

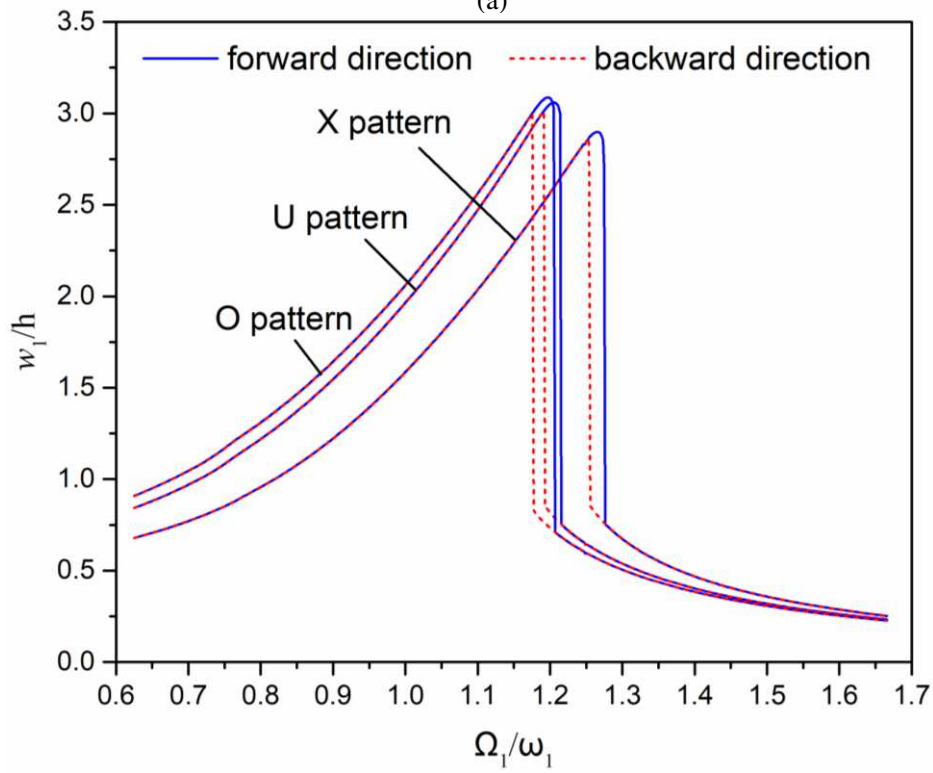


(c)

Figure 4



(a)



(b)

Figure 5

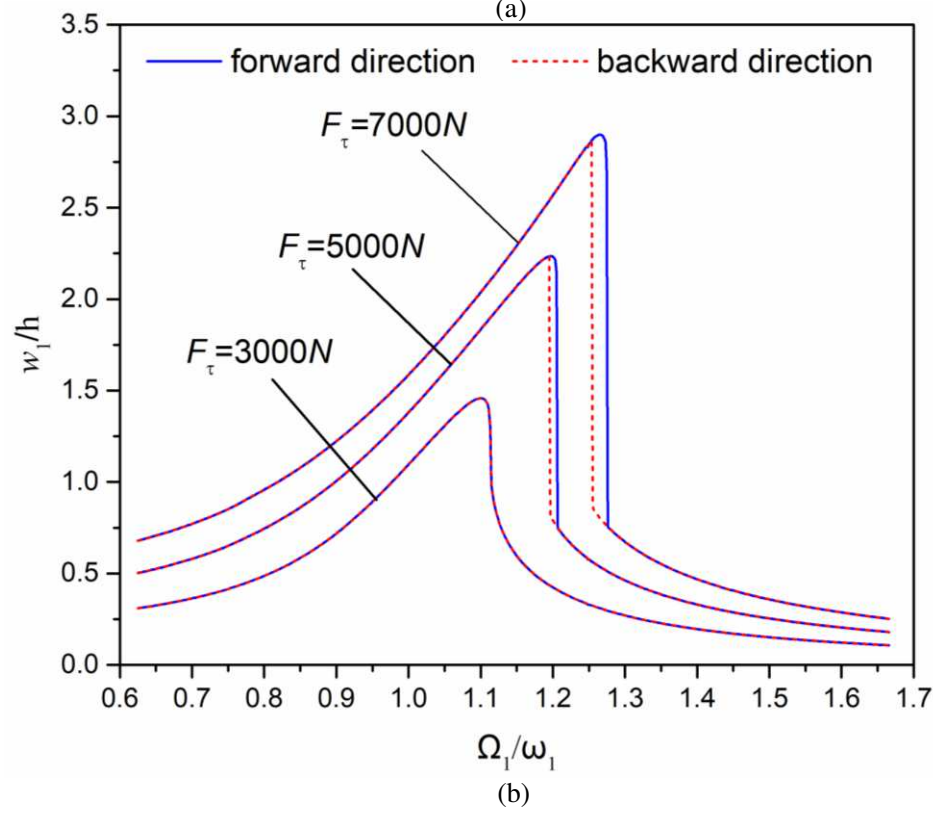
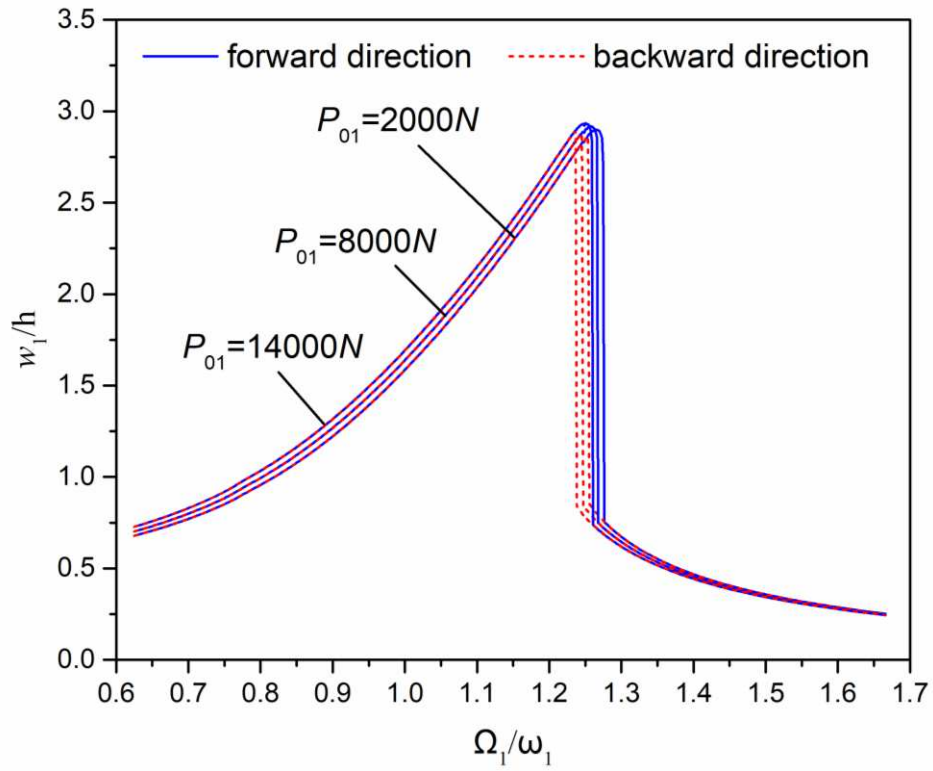


Figure 6

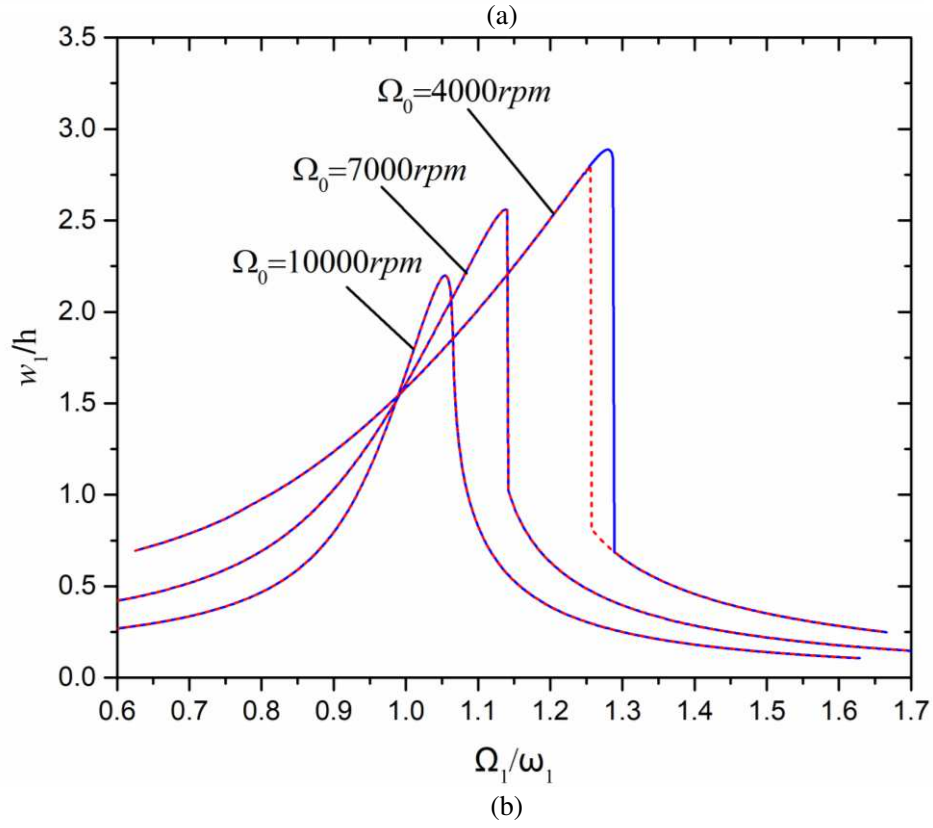
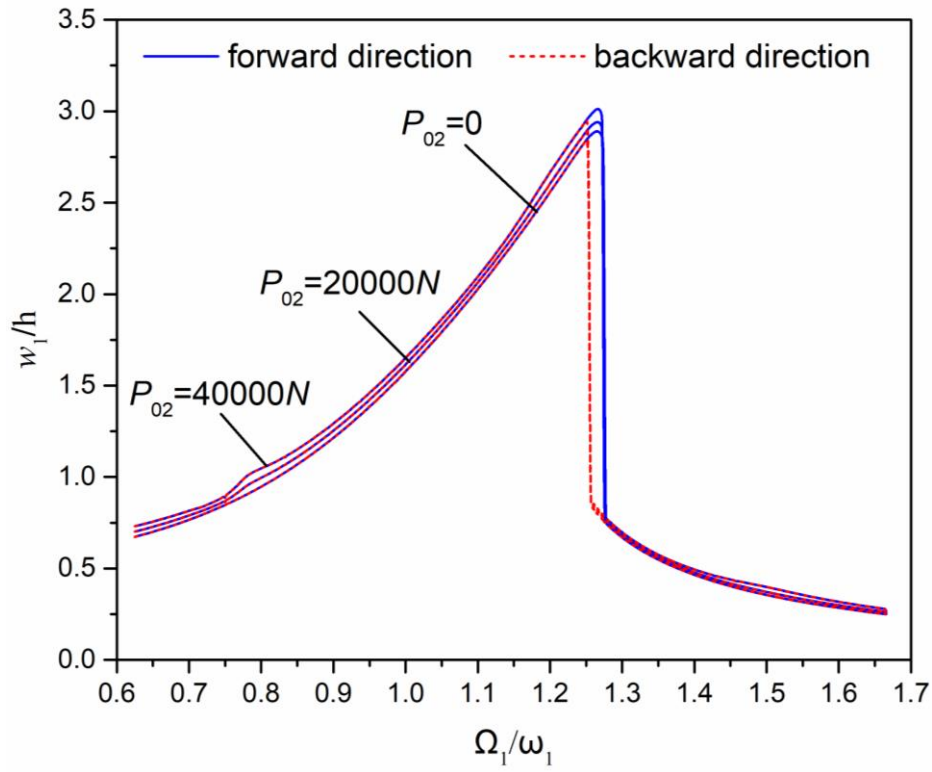
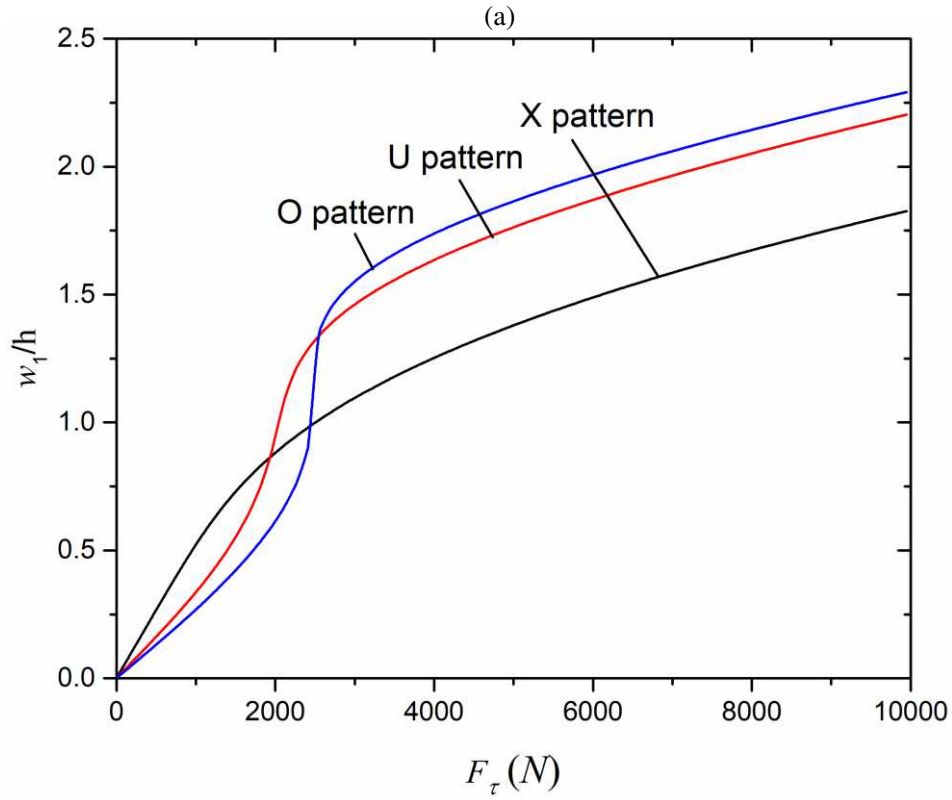
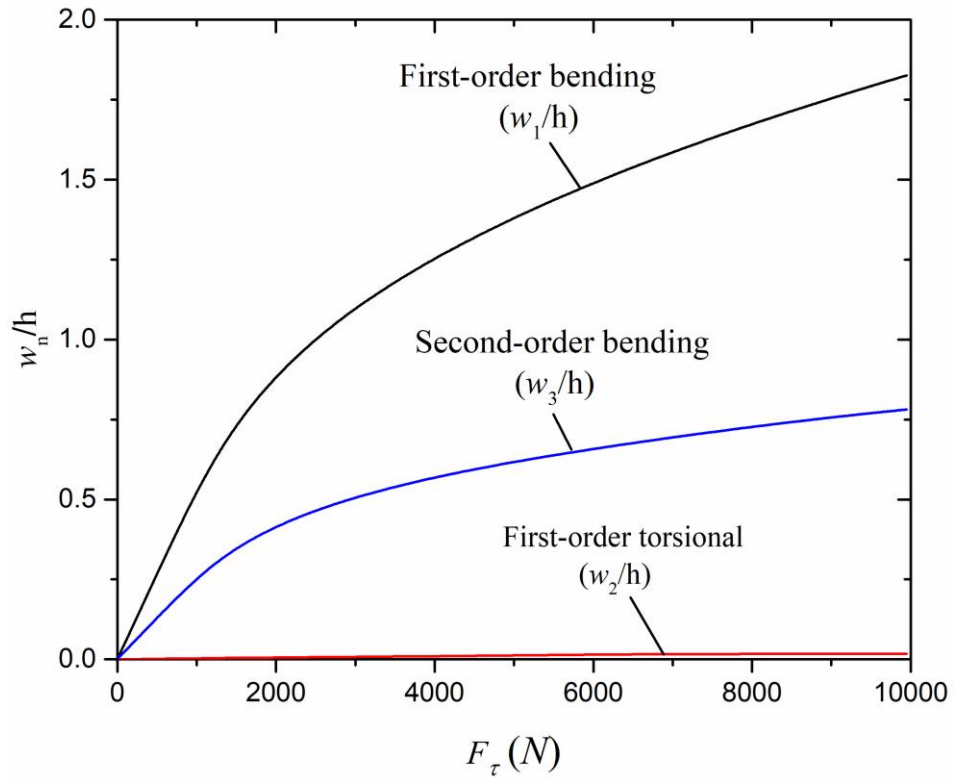


Figure 7



(b)
Figure 8

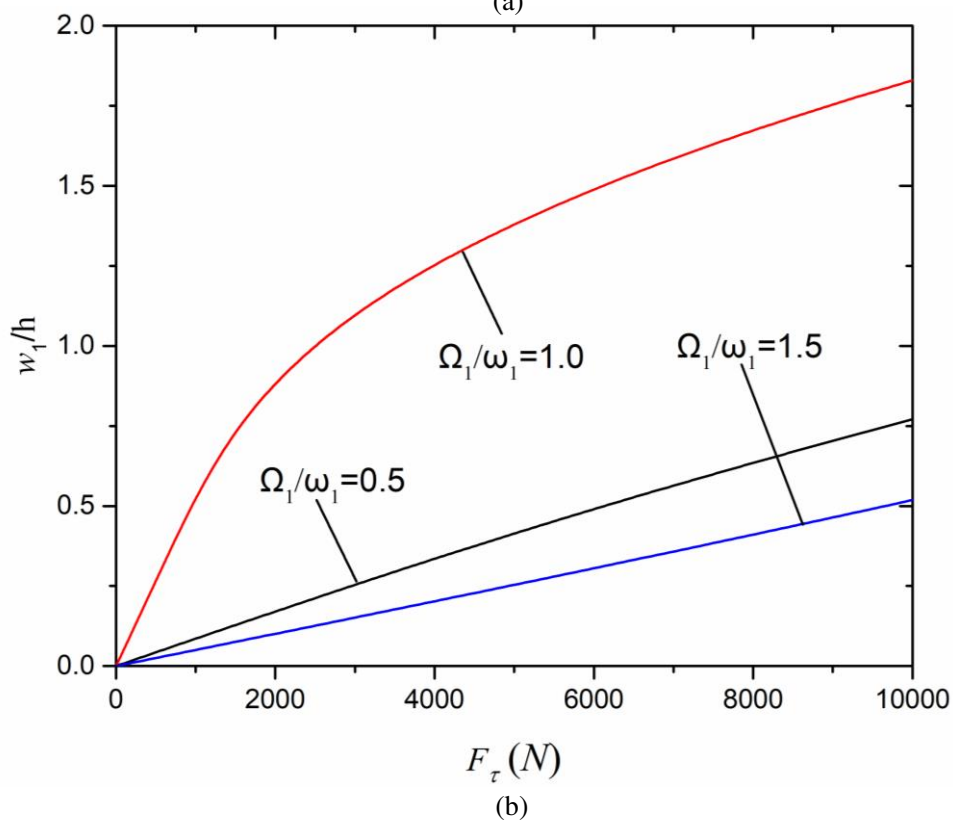
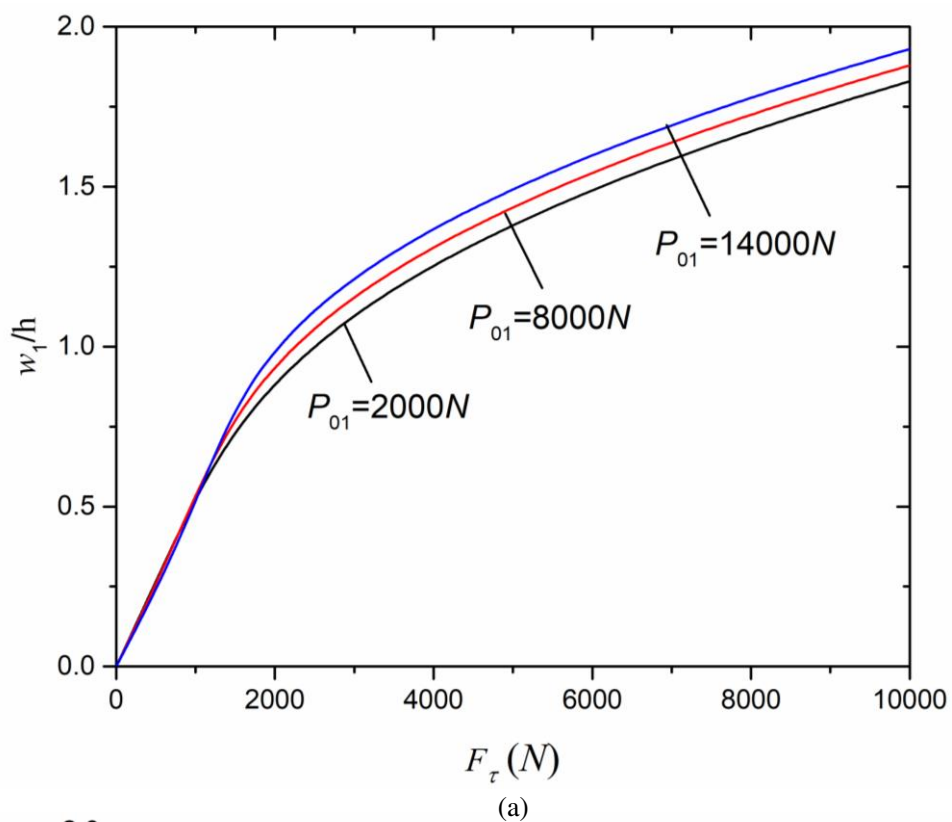


Figure 9

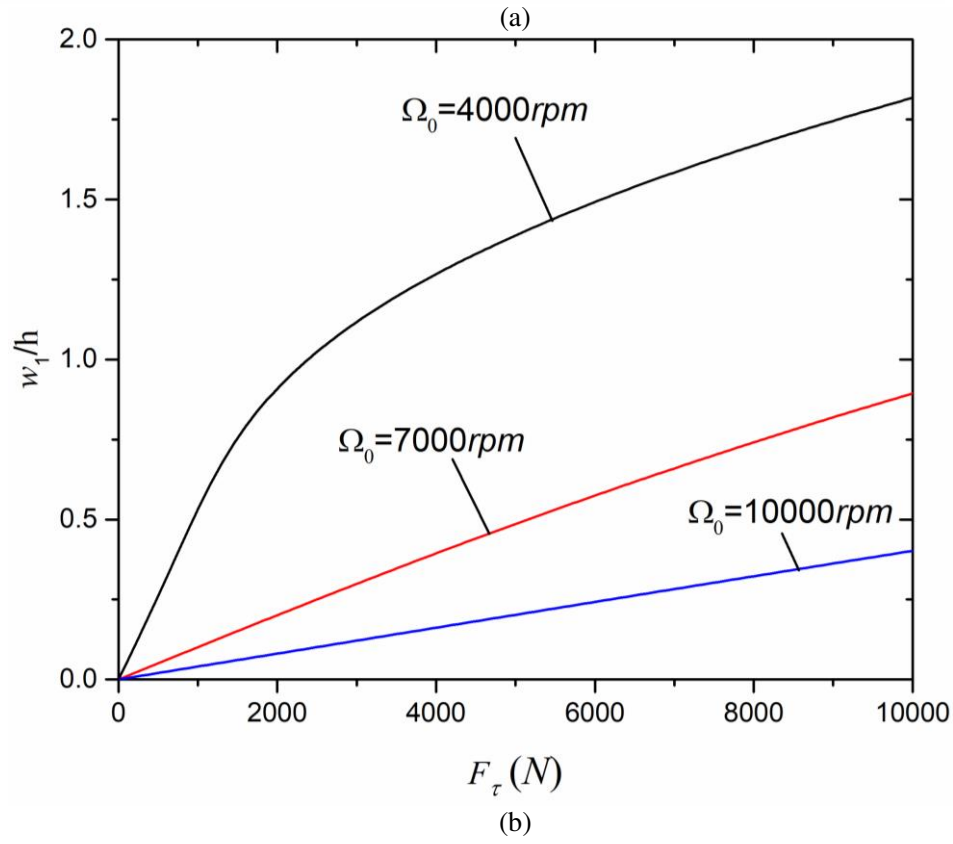
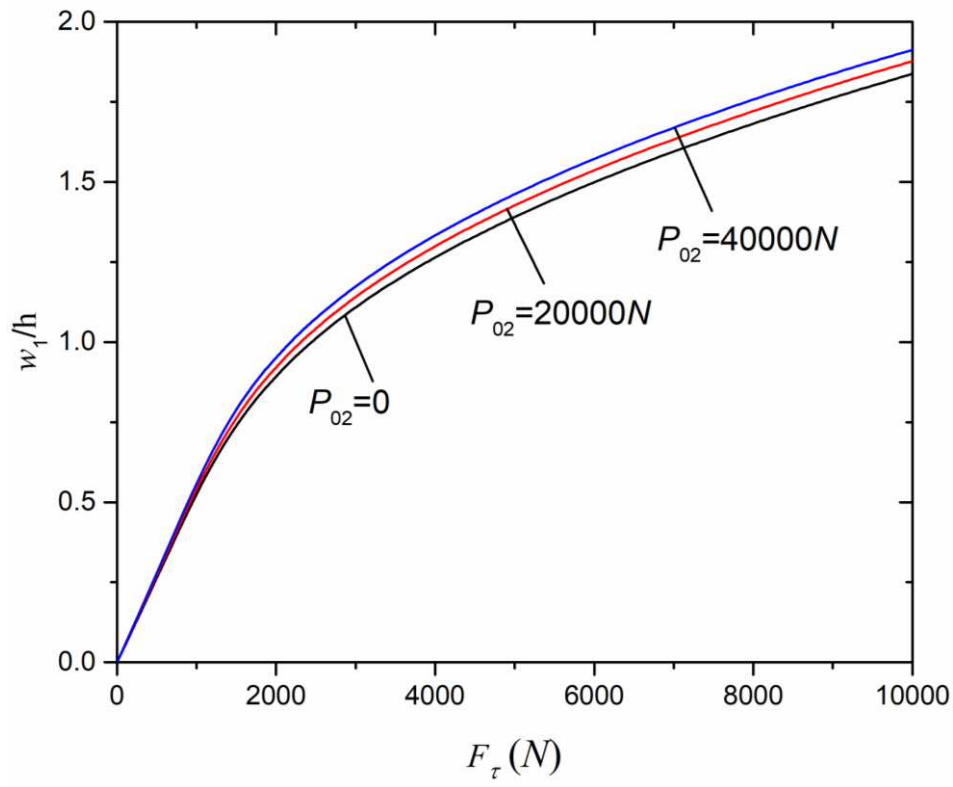


Figure 10

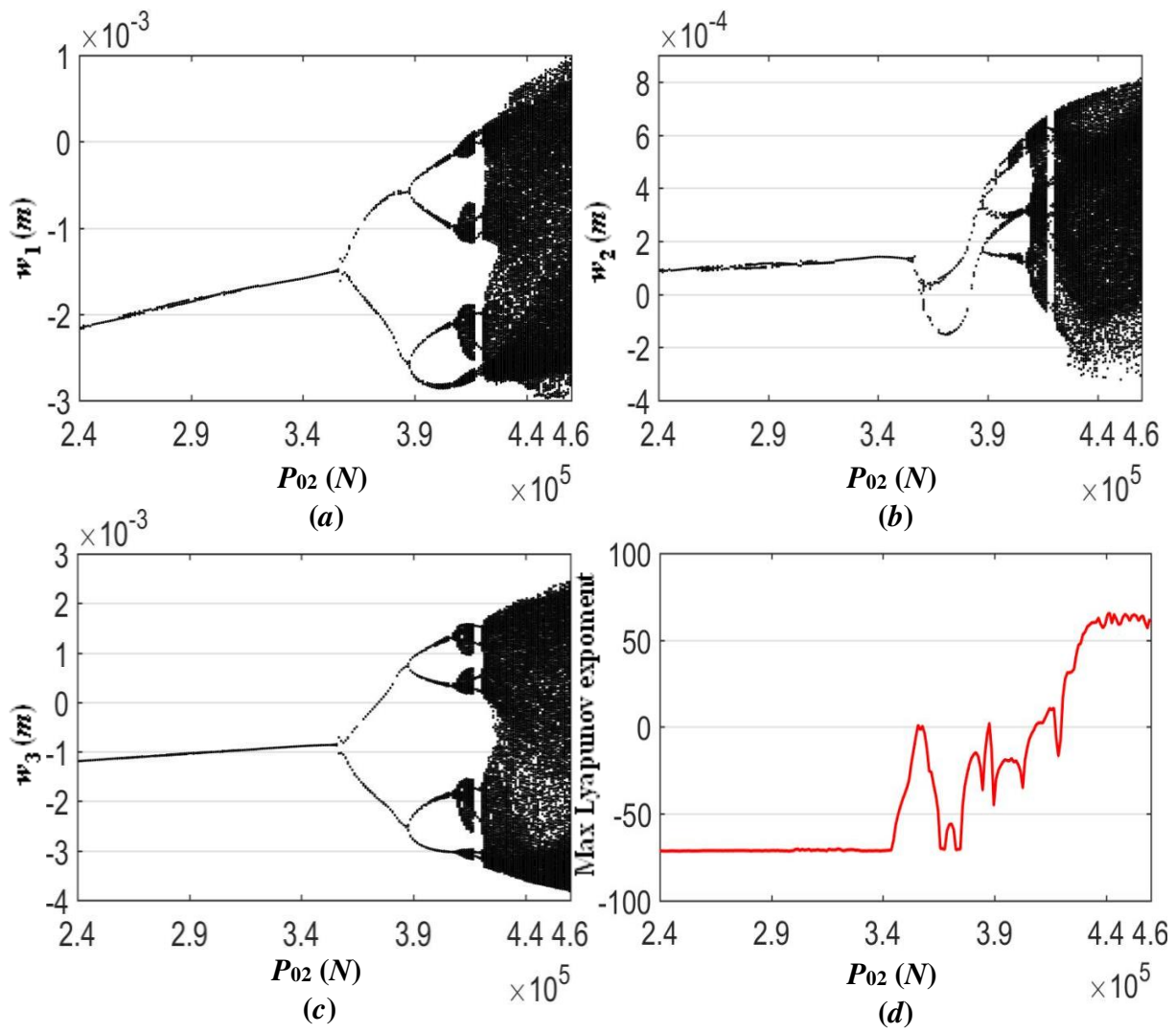


Figure 11

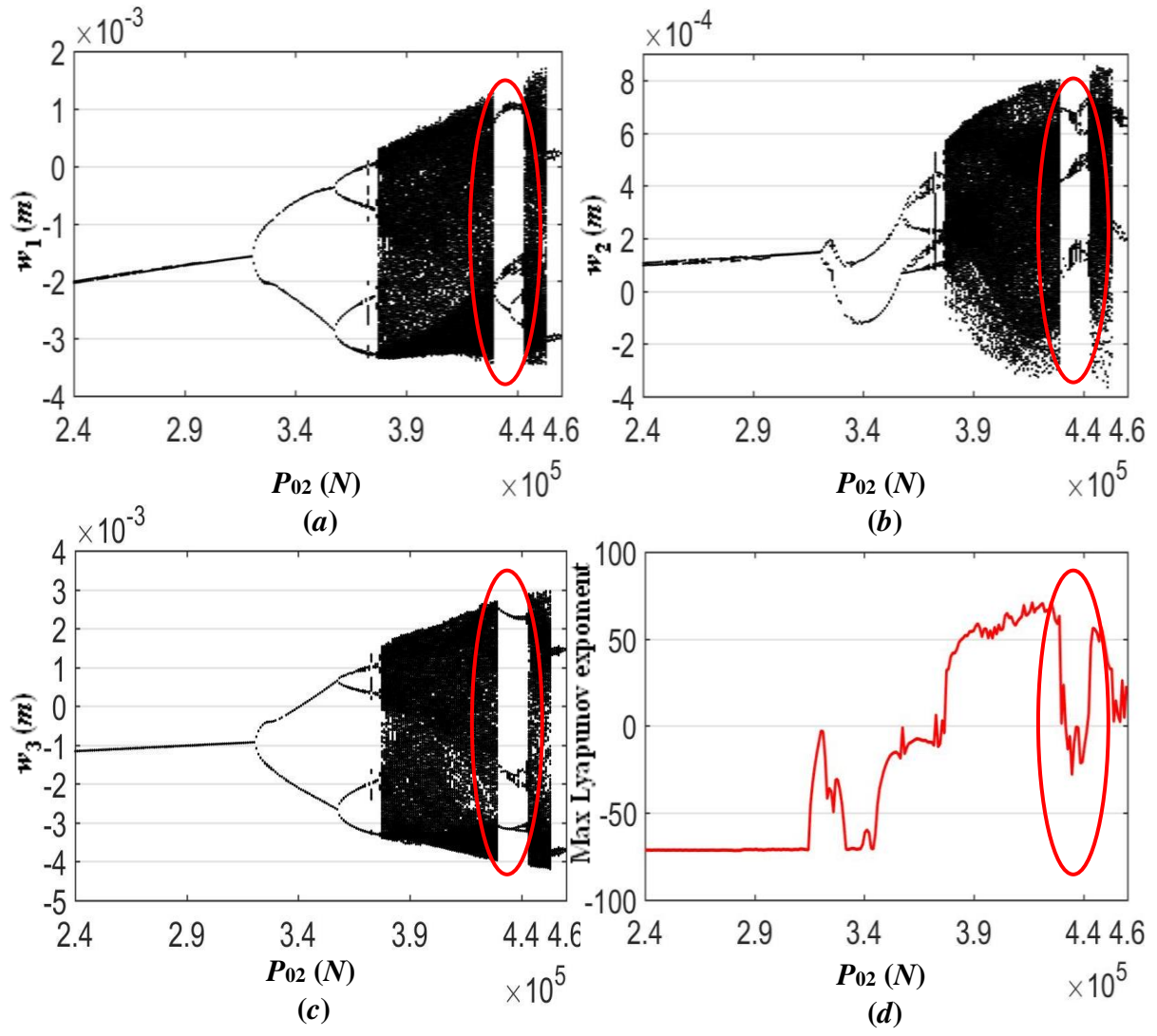


Figure 12

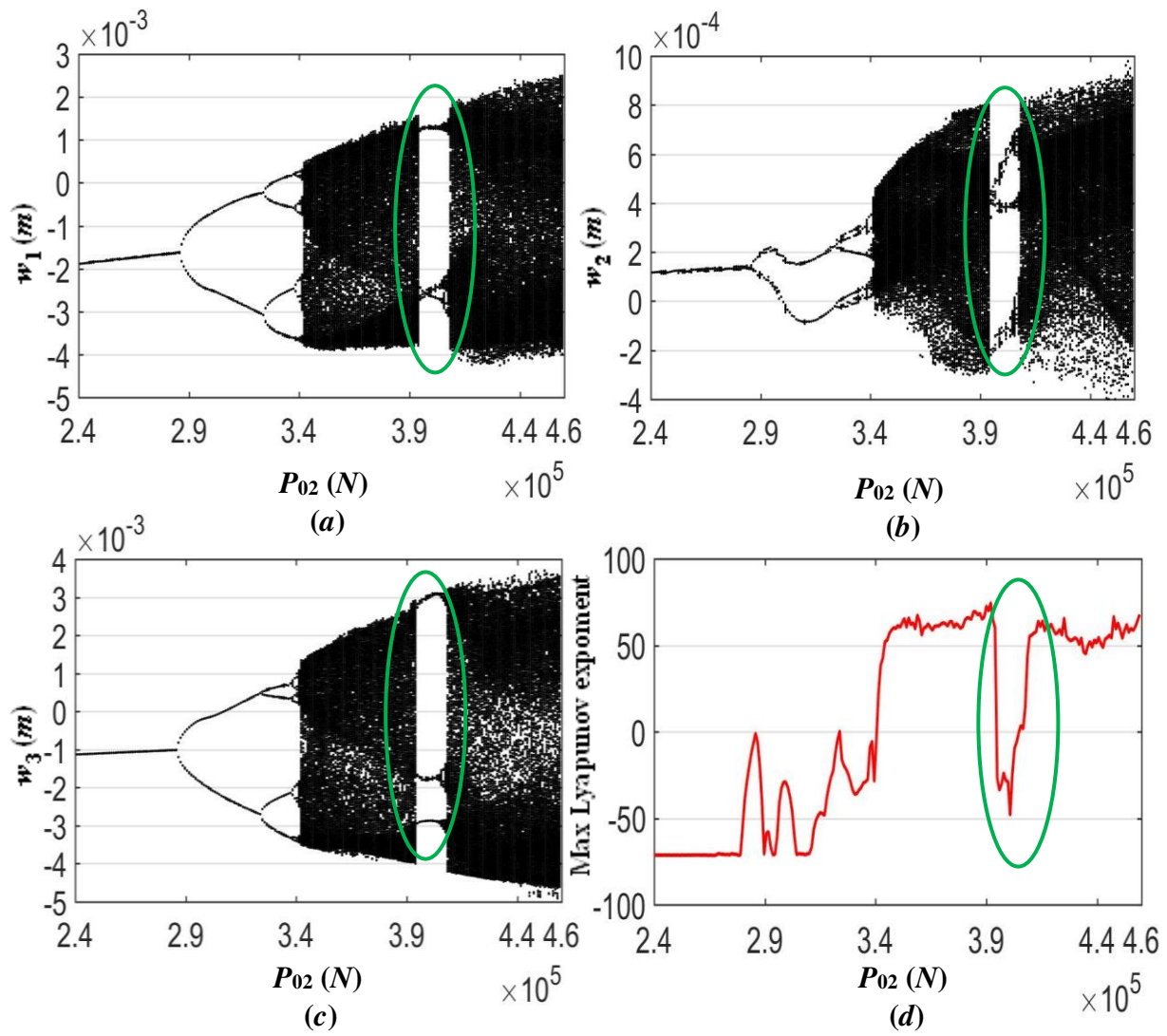


Figure 13

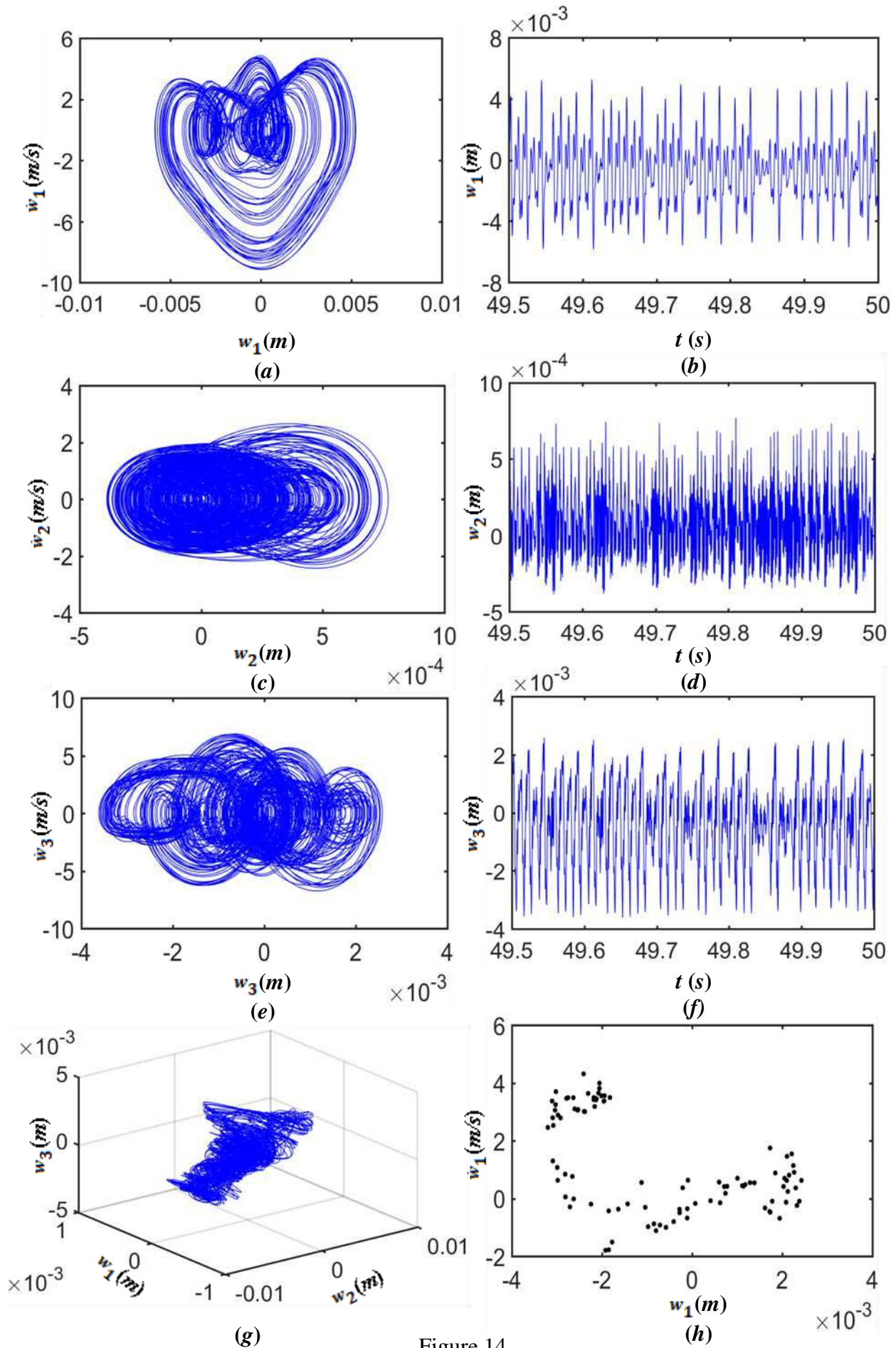


Figure 14

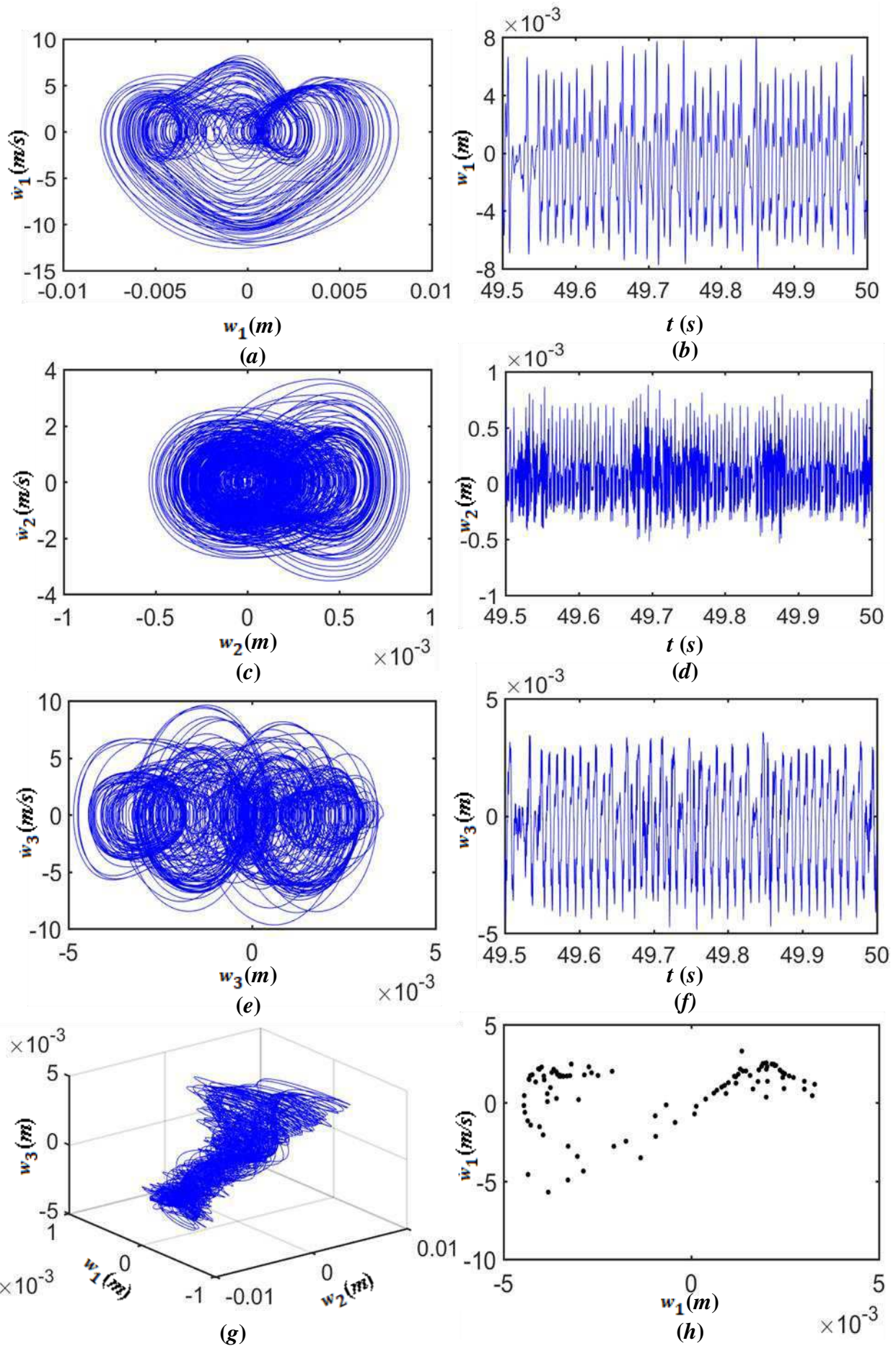


Figure 15

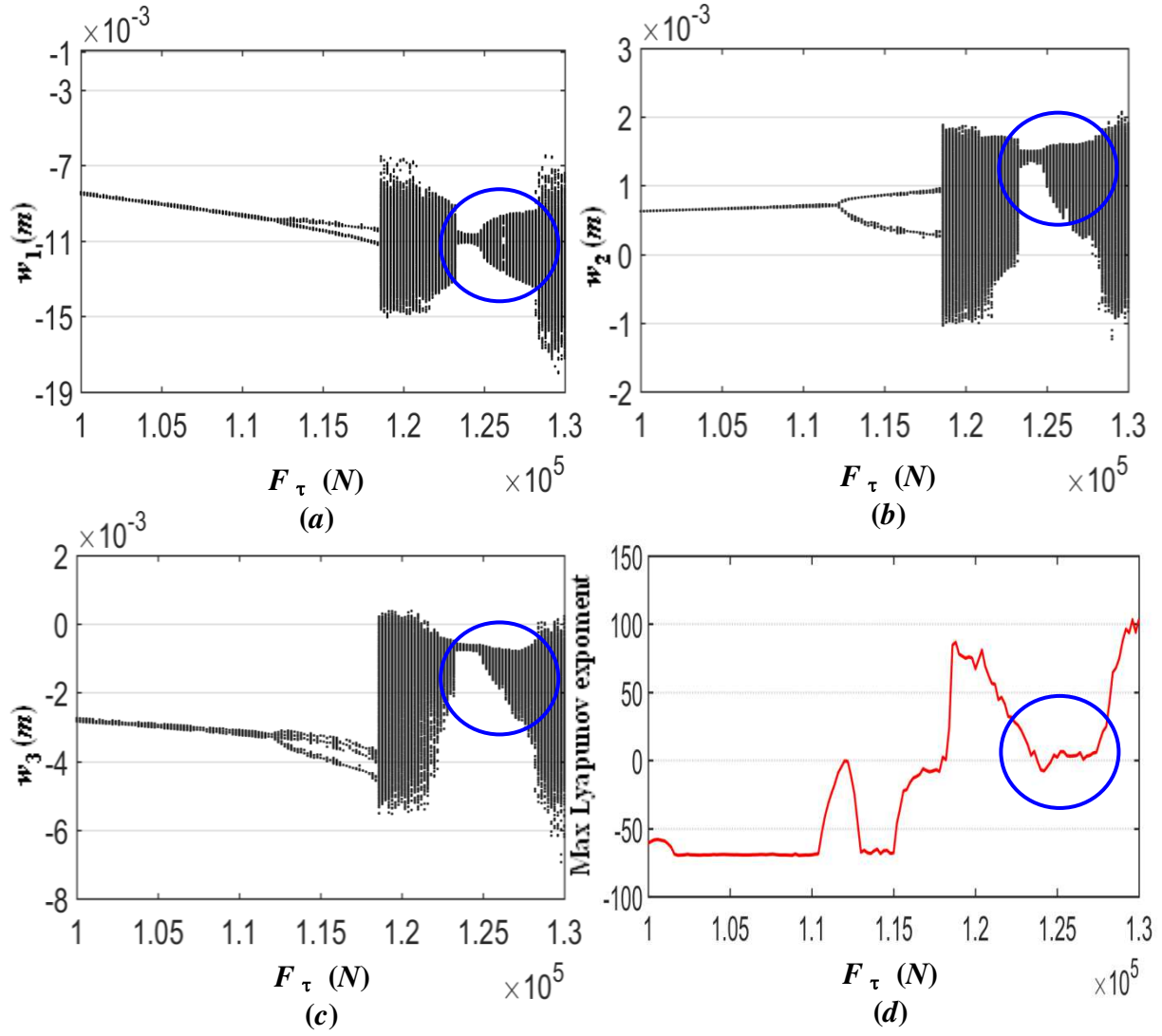


Figure 16

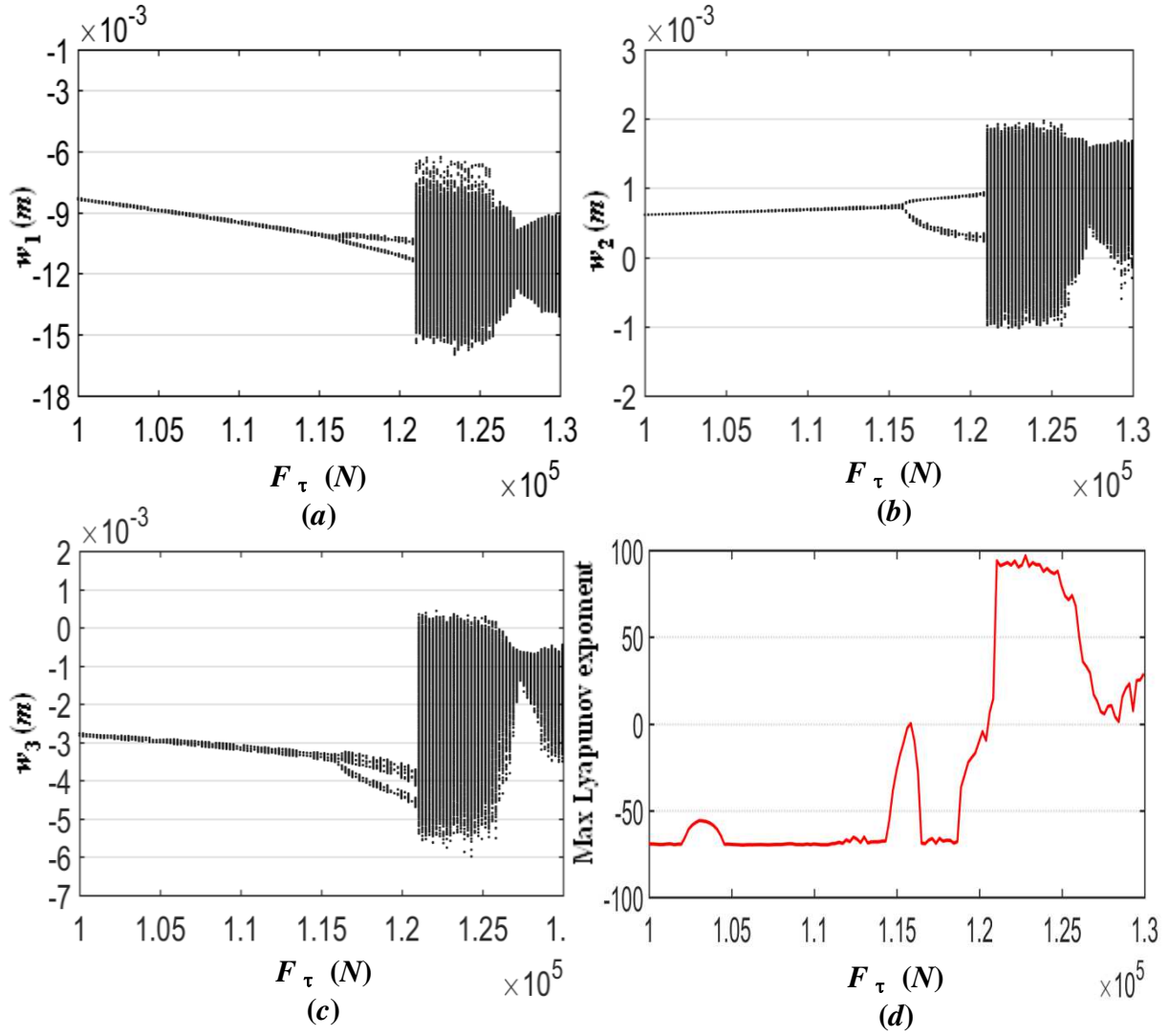


Figure 17

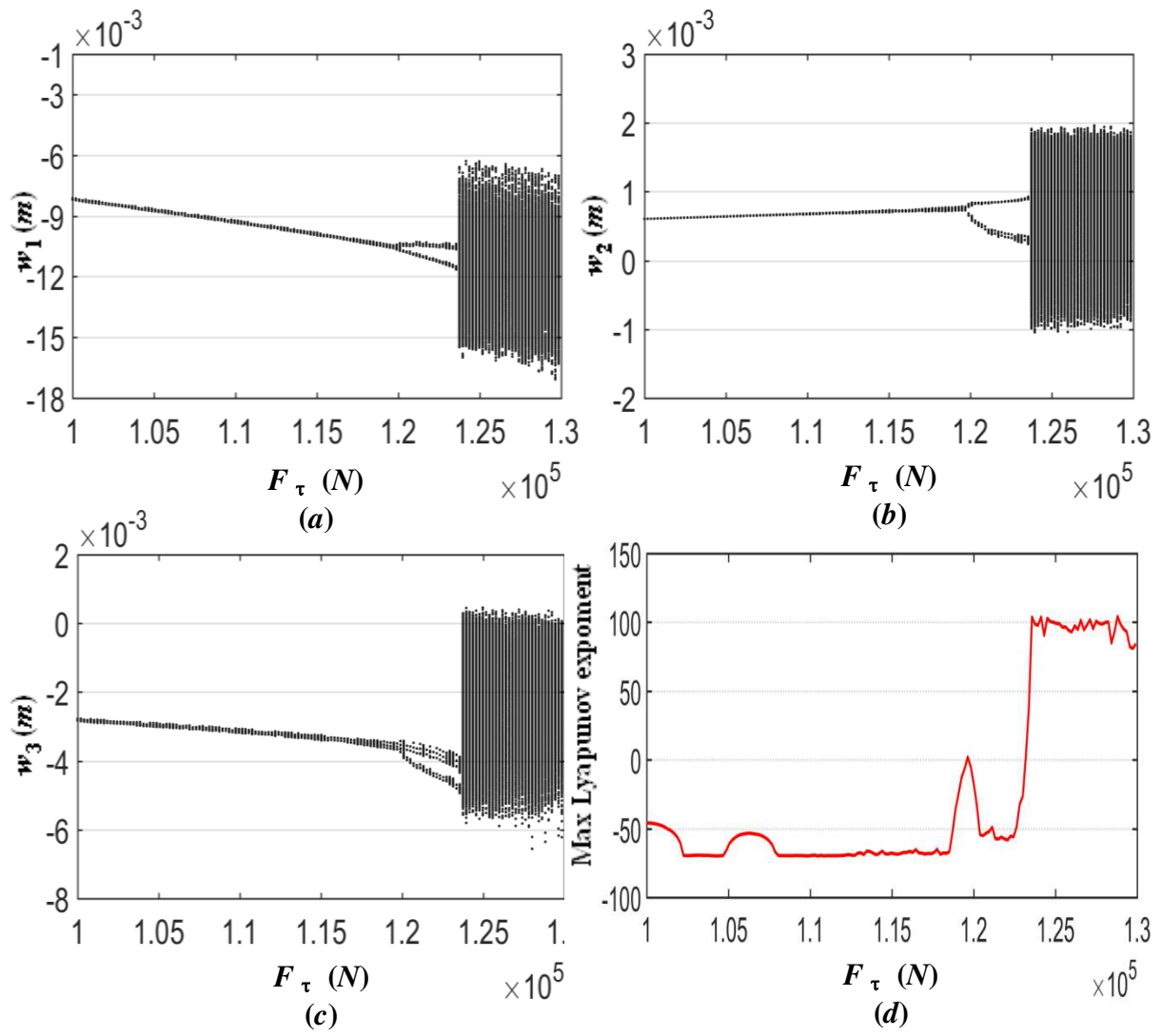


Figure 18

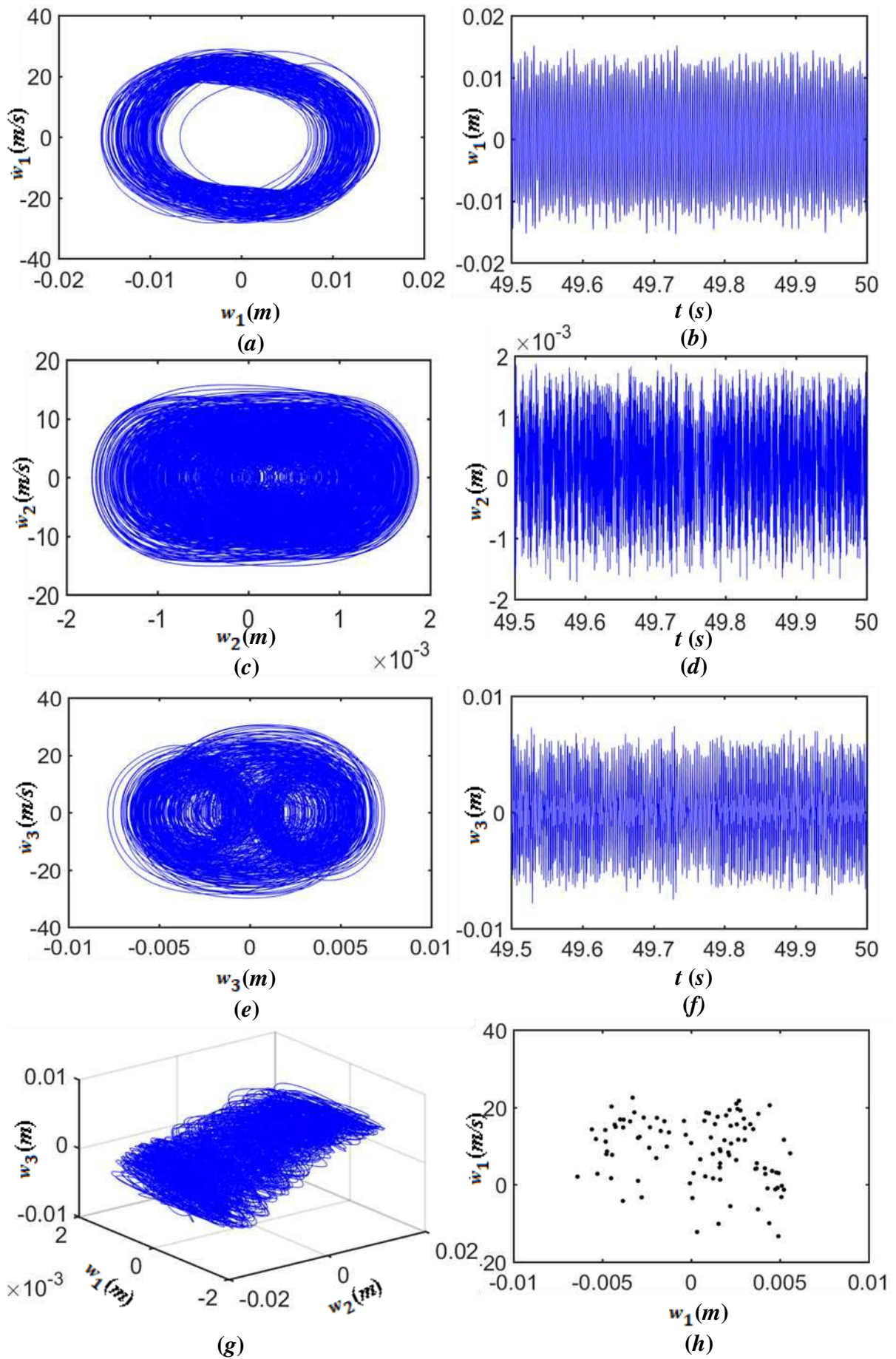


Figure 19

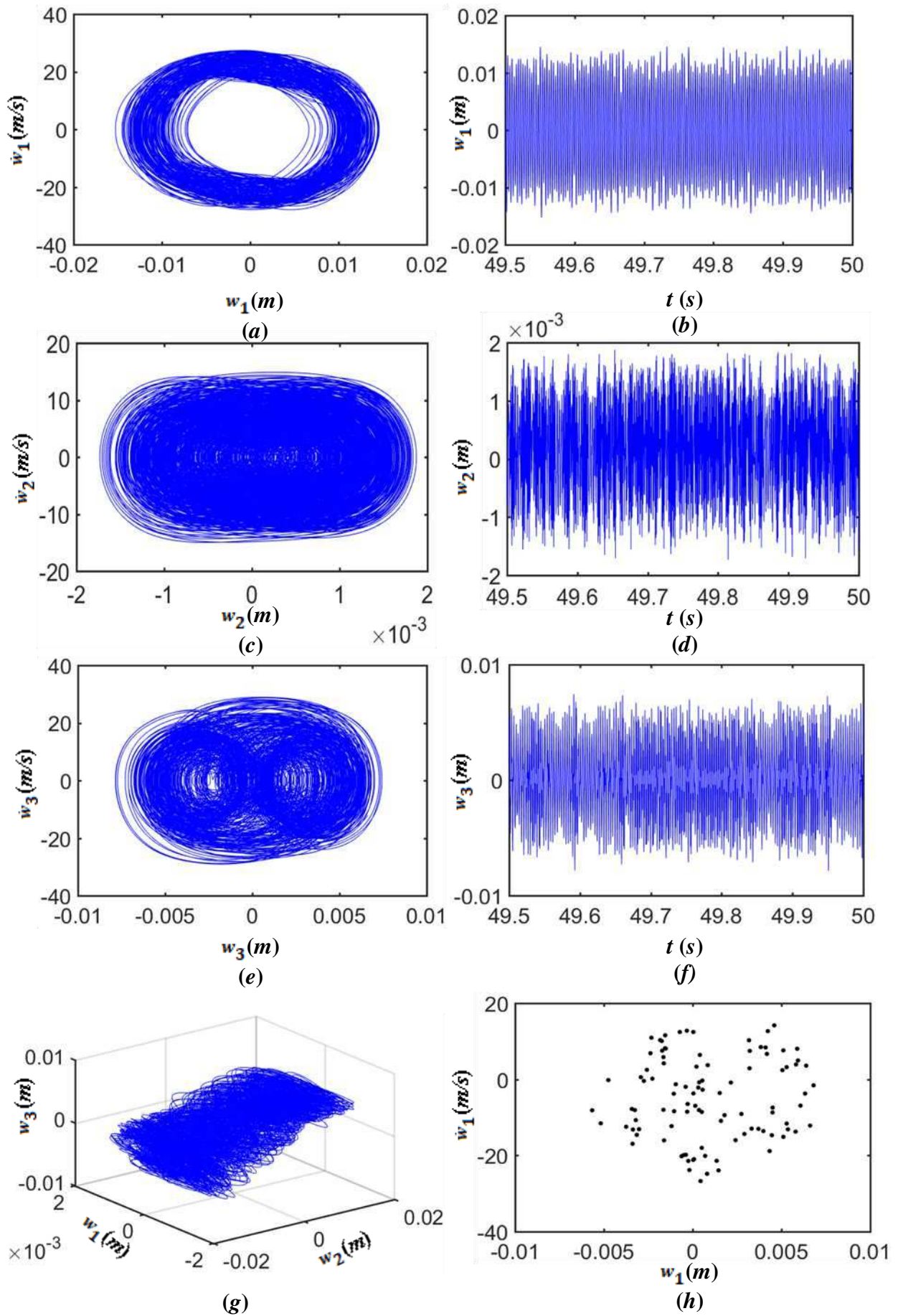


Figure 20

Figures

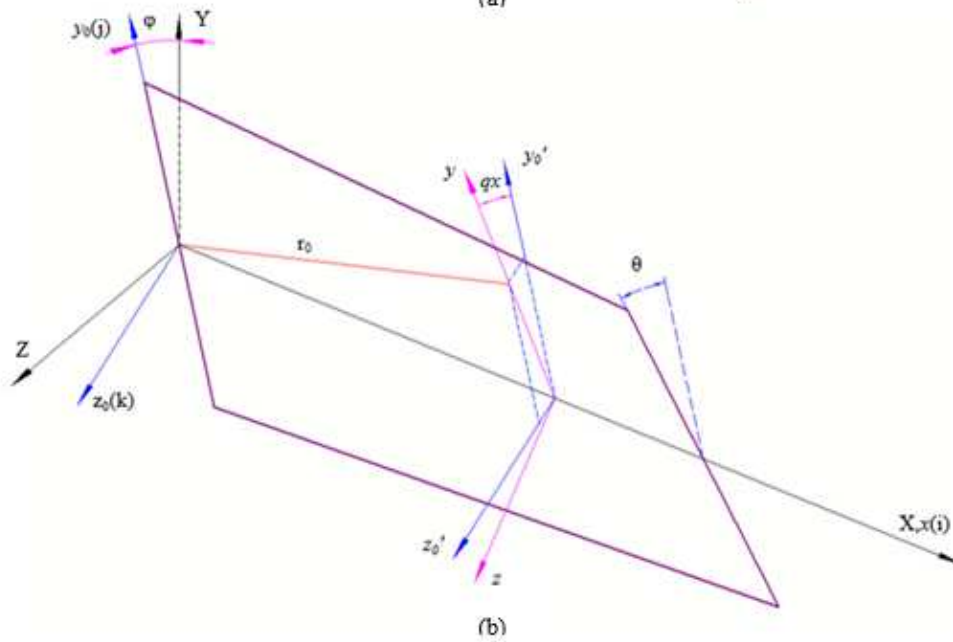
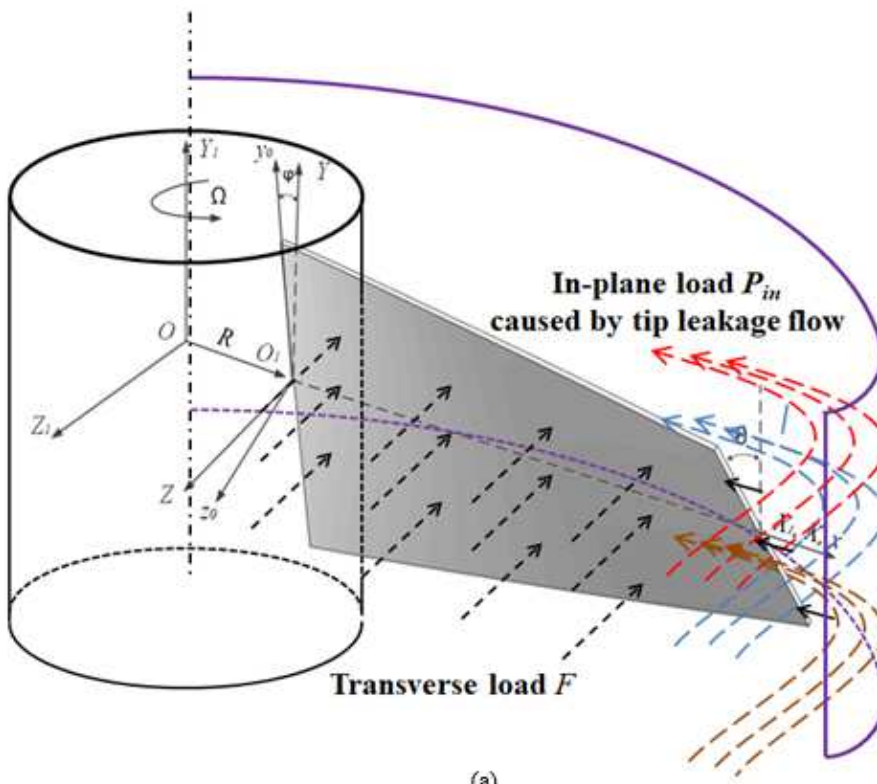


Figure 1

Figure 1

The dynamic model of the functionally graded graphene platelet (FGGP) reinforced rotating pretwisted composite blade under the axial and transverse excitations is given, (a) model, (b) cantilever plate model and coordinate systems.

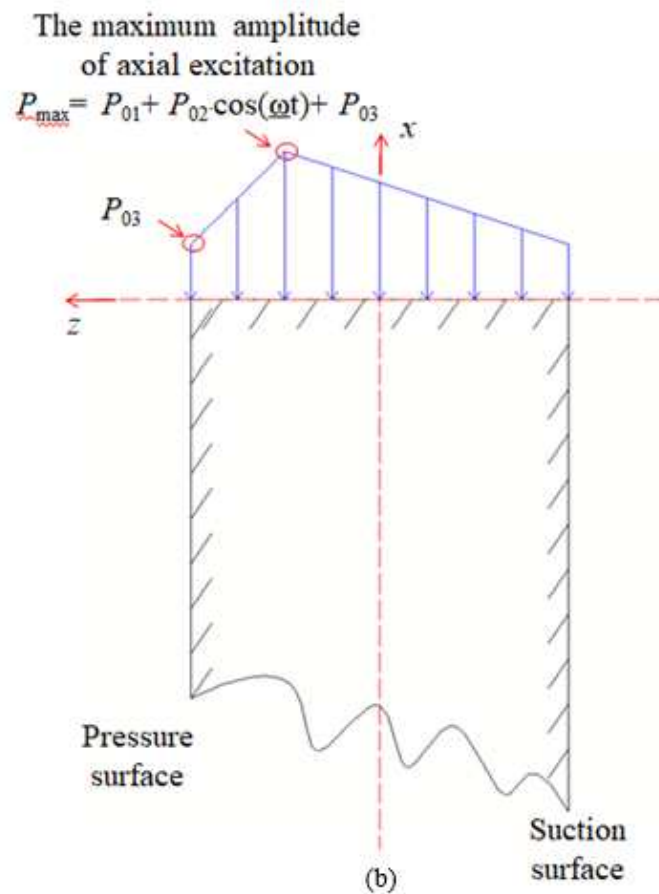
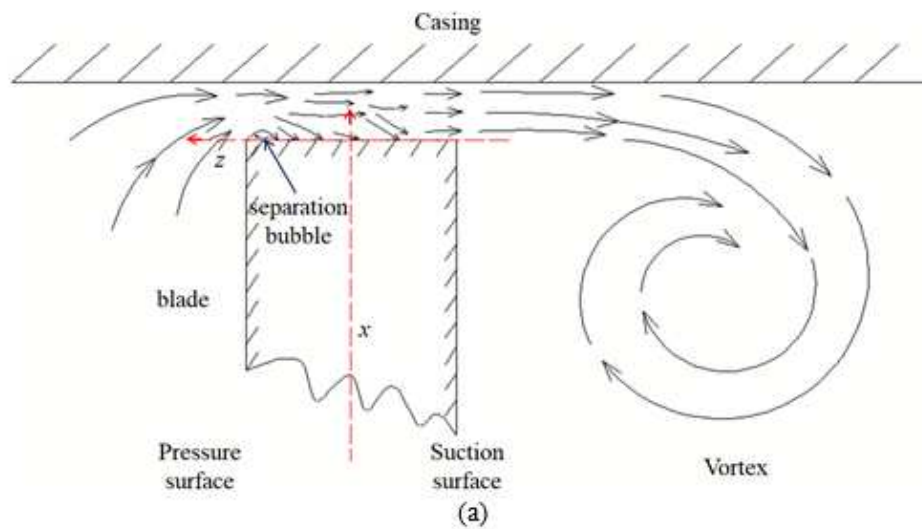


Figure 2

Figure 2

The sketch map of the airflow and axial load on the tip clearance of the blade is given, (a) airflow passes through tip clearance, (b) distribution for axial load in tip clearance

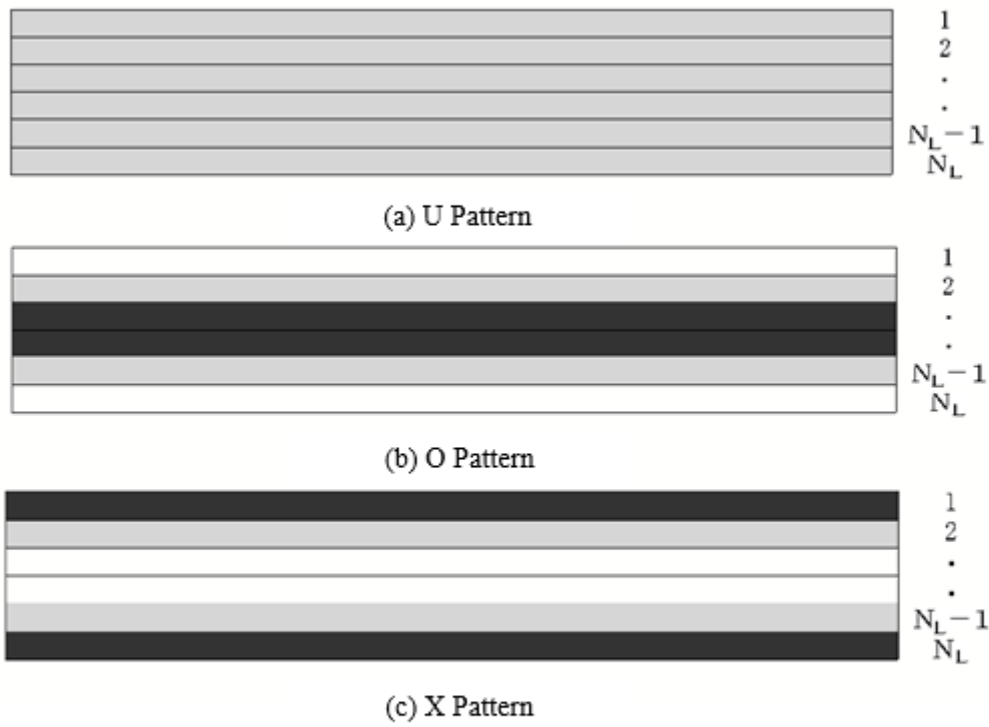


Figure 3

Figure 3

The sketch map of different graphene platelet distribution types is obtained.

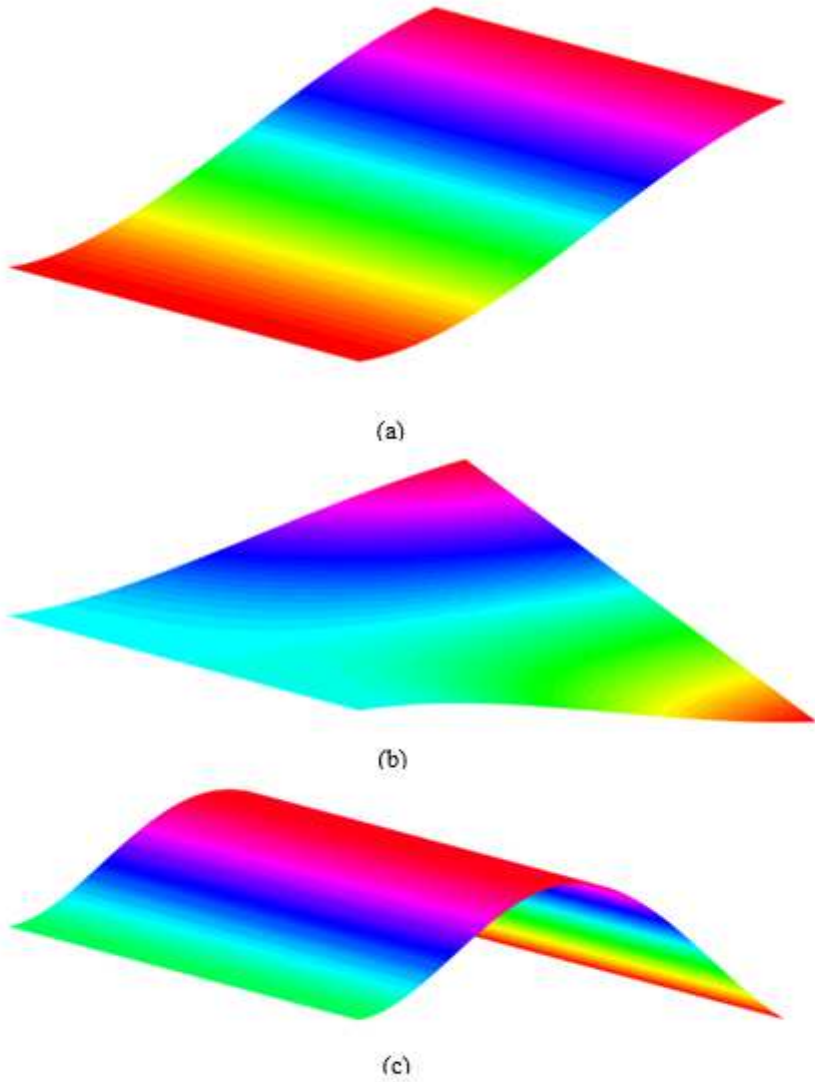


Figure 4

Figure 4

The first third vibration mode shapes are obtained for the FGGP reinforced rotating pretwisted composite cantilever rectangular plate, (a) first-order bending vibration mode, (b) first-order torsional vibration mode, (c) second-order bending vibration mode.

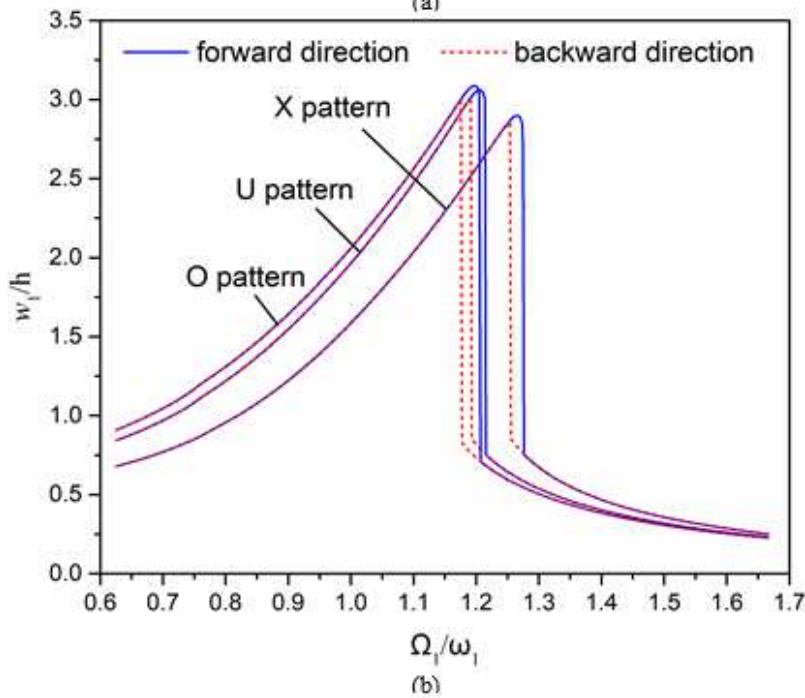
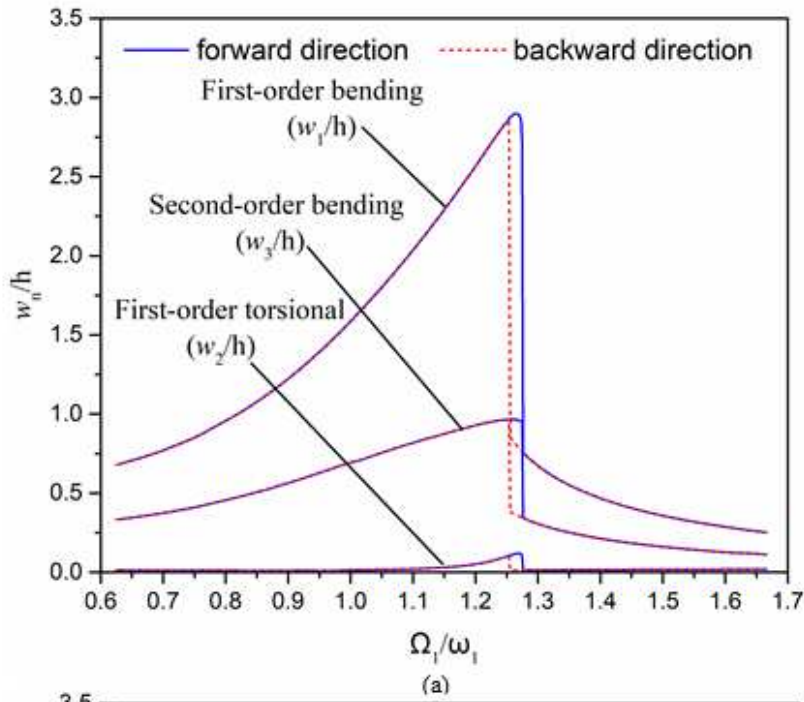


Figure 5

Figure 5

The amplitude-frequency response curves are obtained for the graphene platelet reinforced rotating pretwisted composite cantilever plate with three different vibration modes and three different distribution types, (a) amplitude-frequency response curves of X pattern graphene platelet reinforced plate with three different vibration modes, (b) amplitude-frequency response curves of first-order bending vibration with three different distribution types.

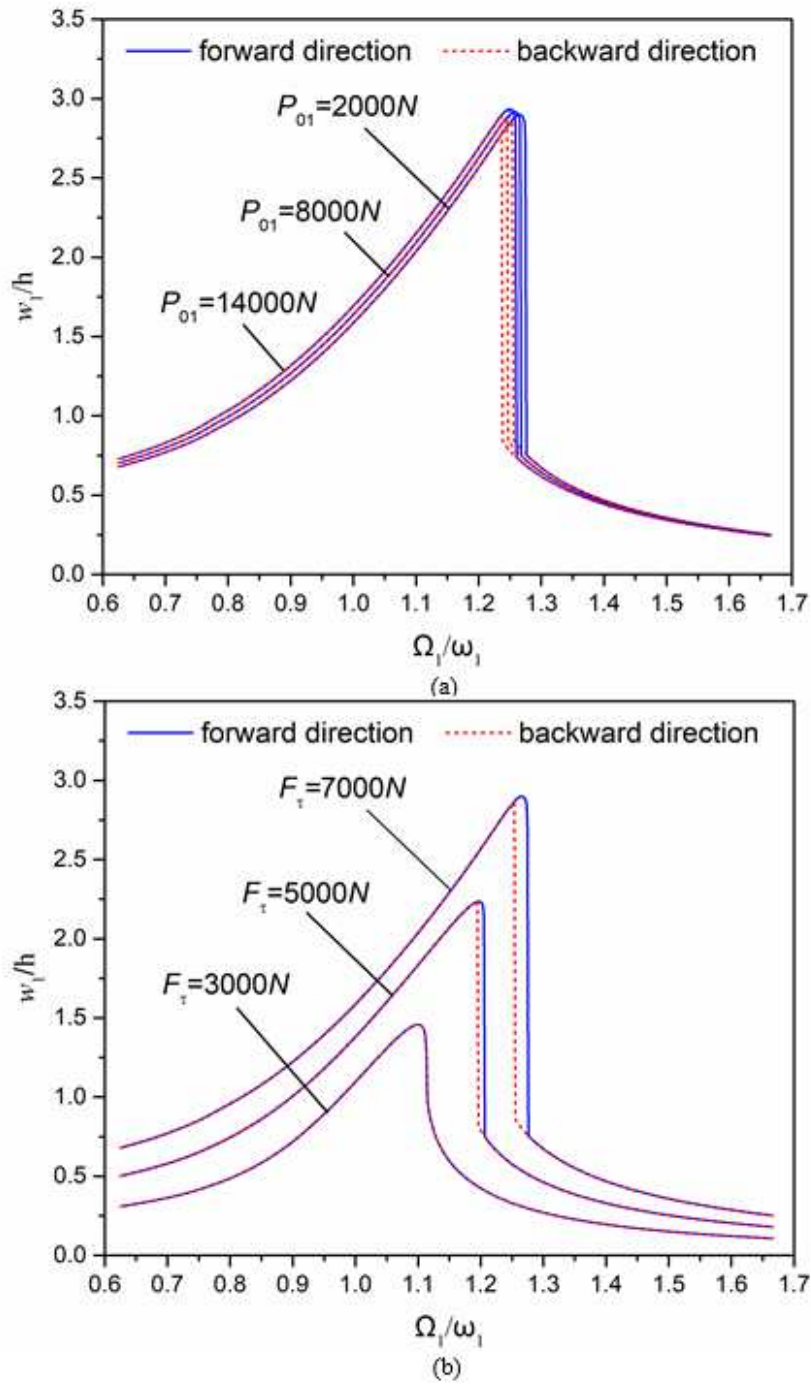


Figure 6

Figure 6

Please see the Manuscript PDF file for the complete figure caption.

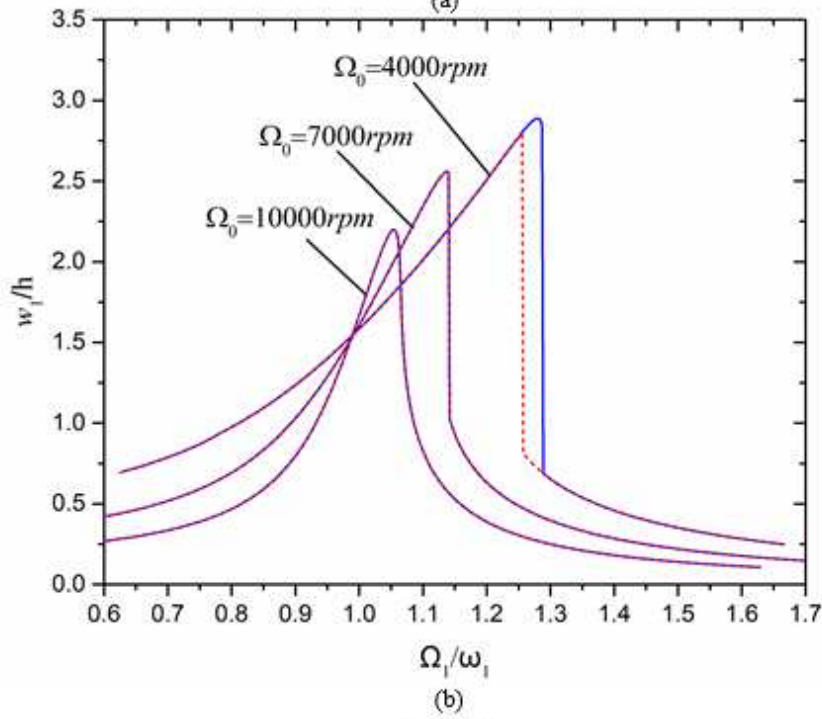
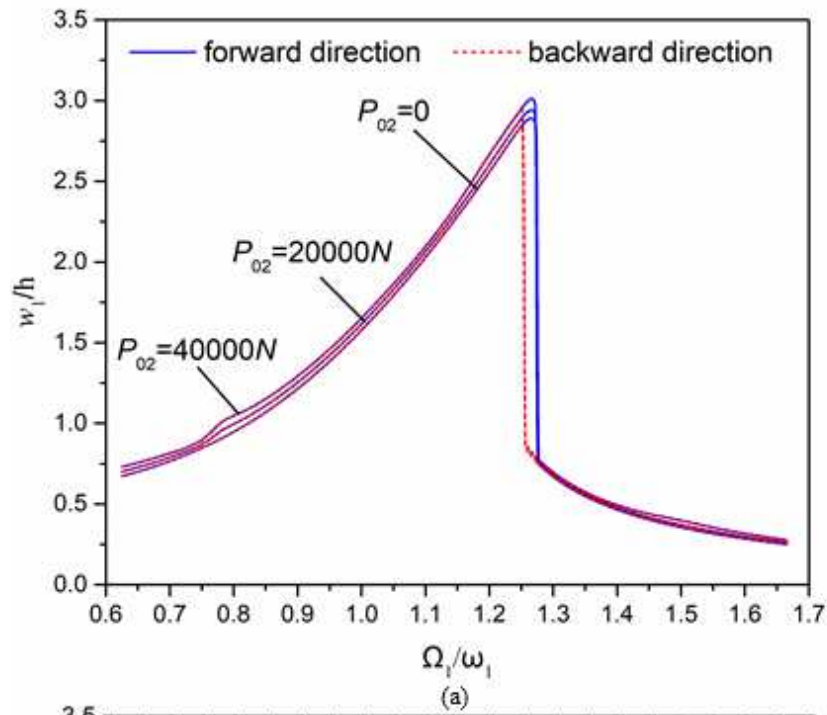


Figure 7

Figure 7

Please see the Manuscript PDF file for the complete figure caption.

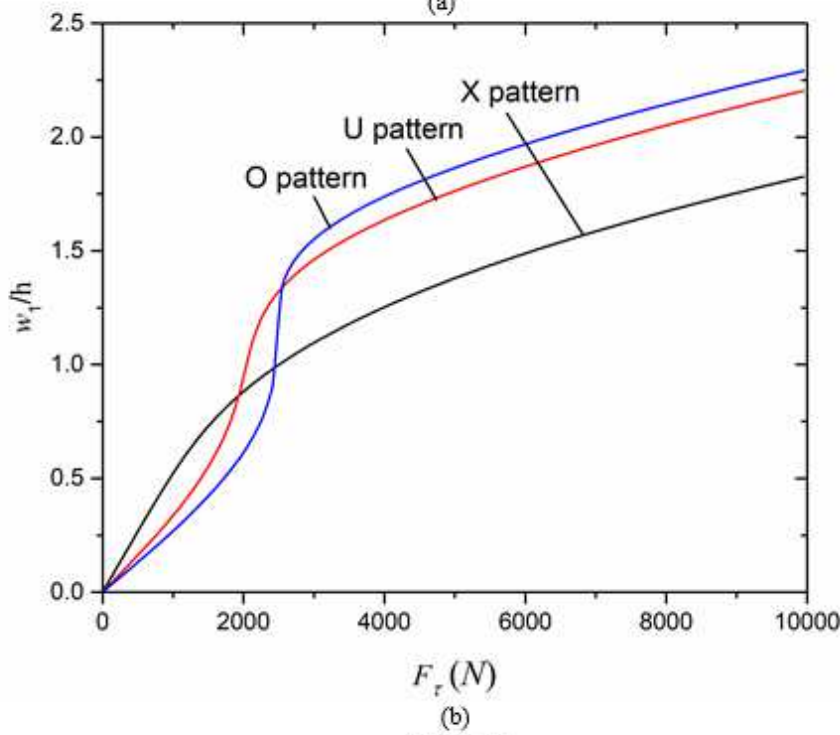
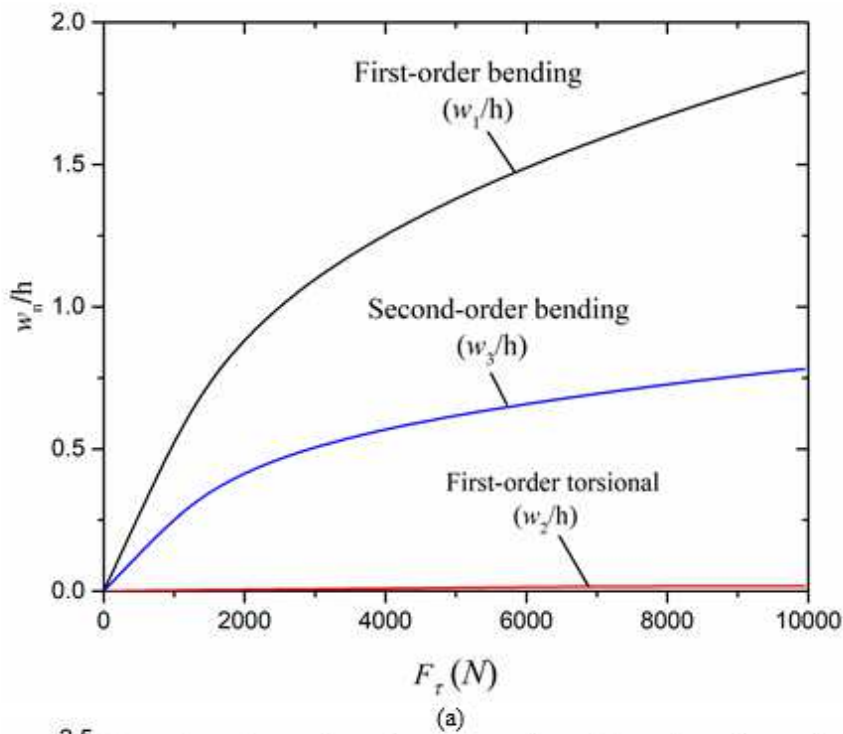
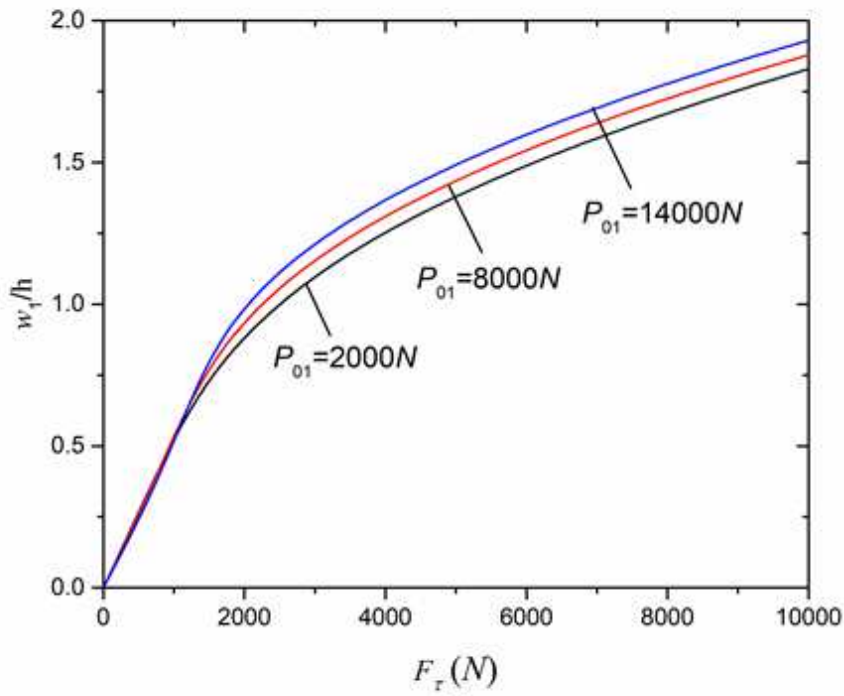


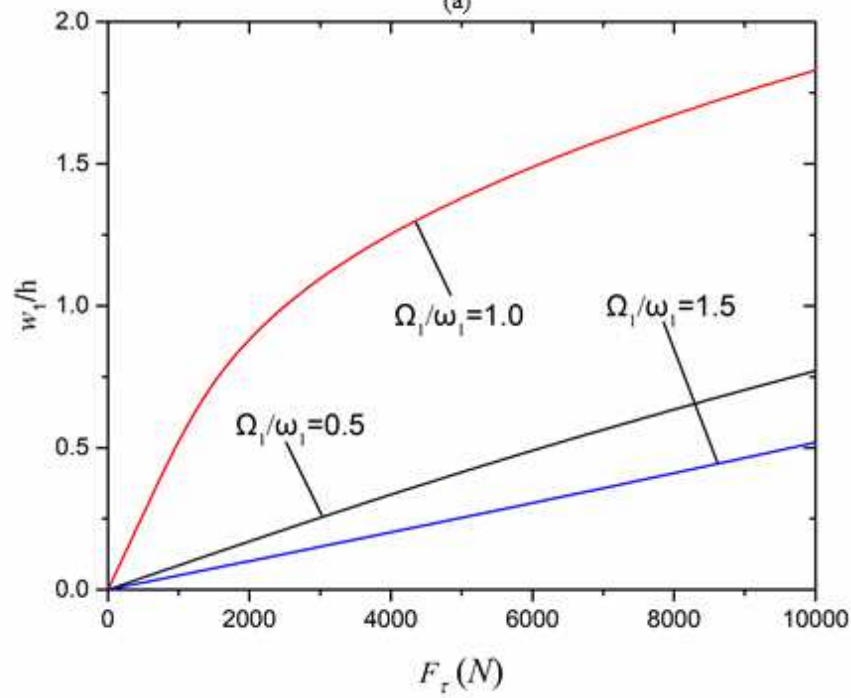
Figure 8

Figure 8

The force-amplitude response curves are obtained for the graphene platelet reinforced rotating pretwisted composite cantilever plate with three different vibration modes and three different distribution types, (a) force-amplitude response curves of X pattern graphene platelet reinforced plate with three different vibration modes, (b) force-amplitude response curves of first-order bending vibration mode with three different distribution types.



(a)

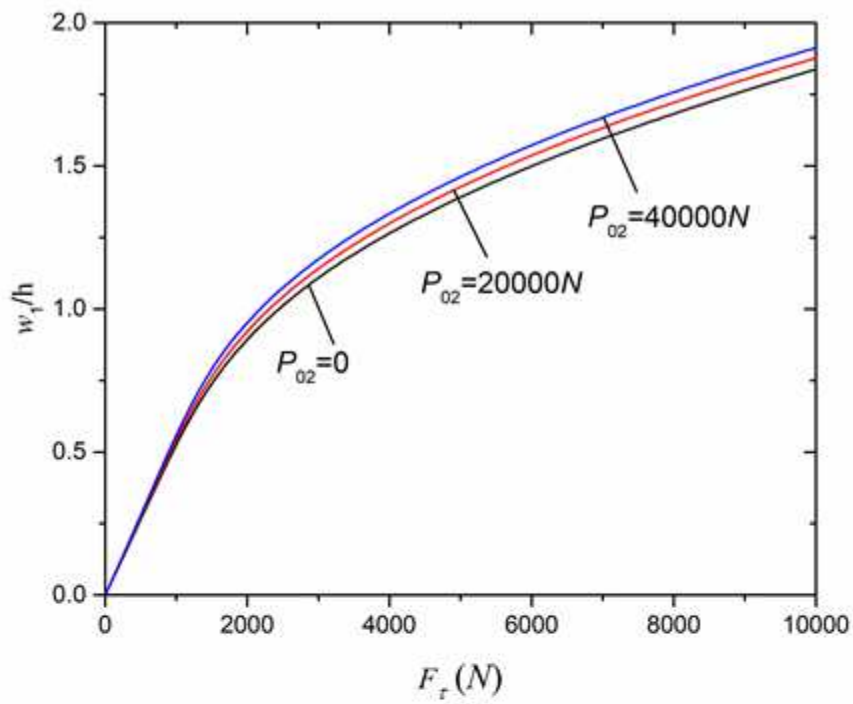


(b)

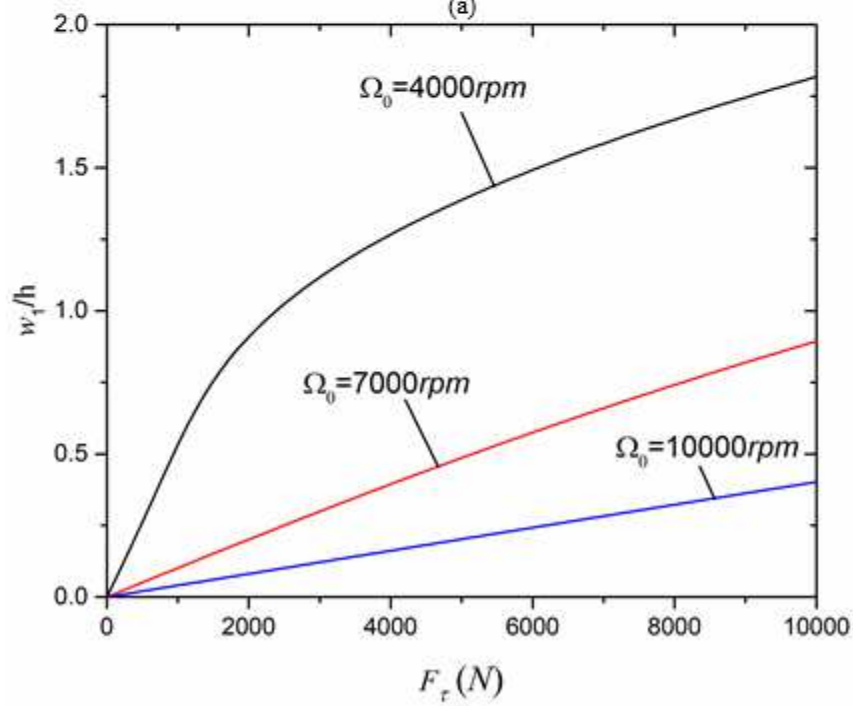
Figure 9

Figure 9

Please see the Manuscript PDF file for the complete figure caption.



(a)



(b)

Figure 10

Figure 10

Please see the Manuscript PDF file for the complete figure caption.

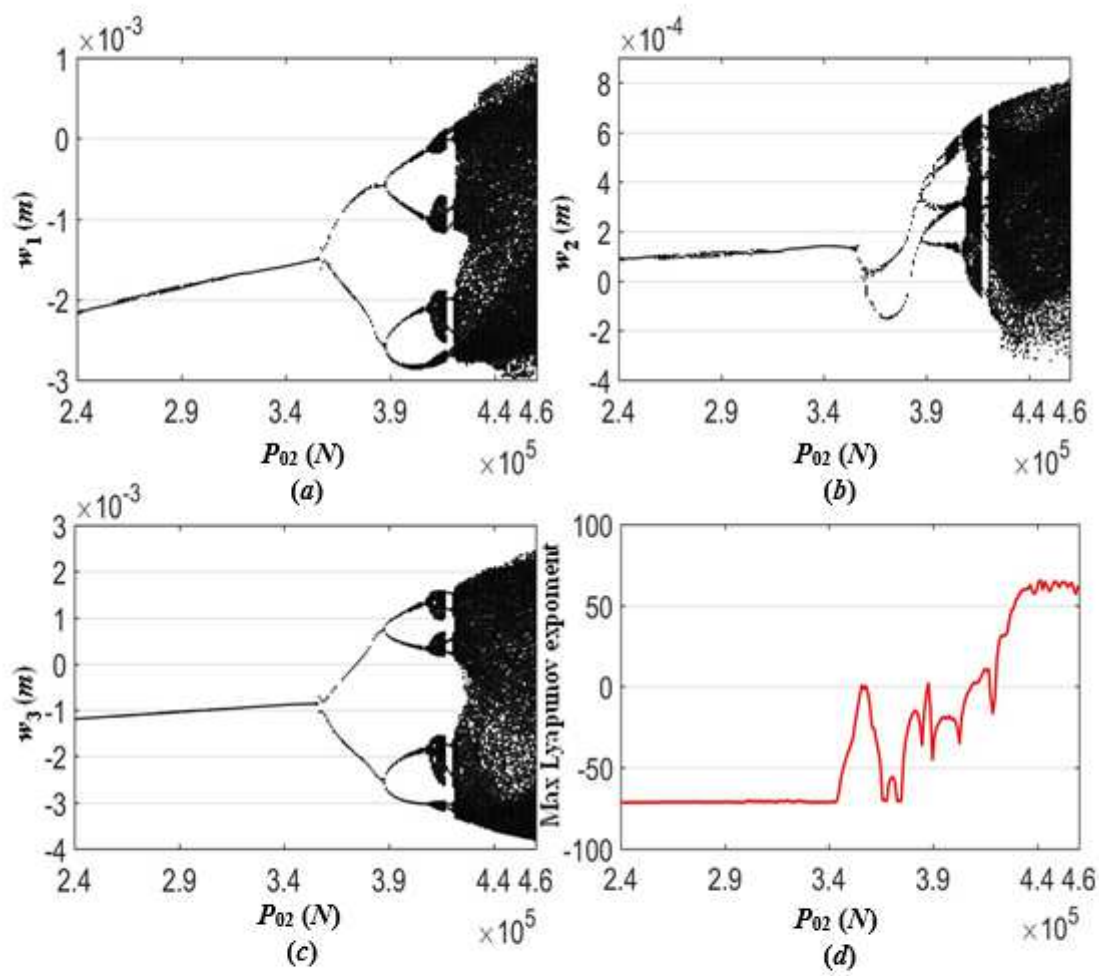


Figure 11

Figure 11

Please see the Manuscript PDF file for the complete figure caption.

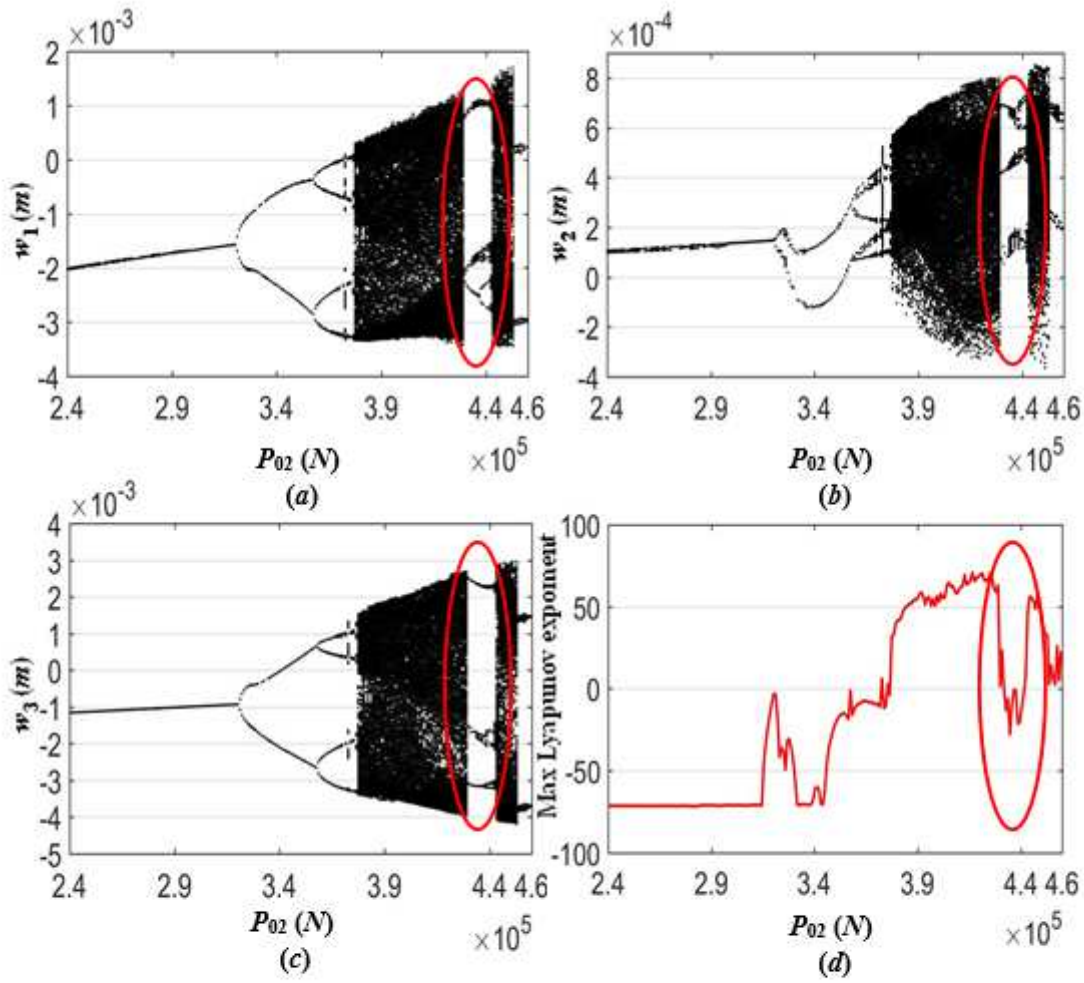


Figure 12

Figure 12

Please see the Manuscript PDF file for the complete figure caption.

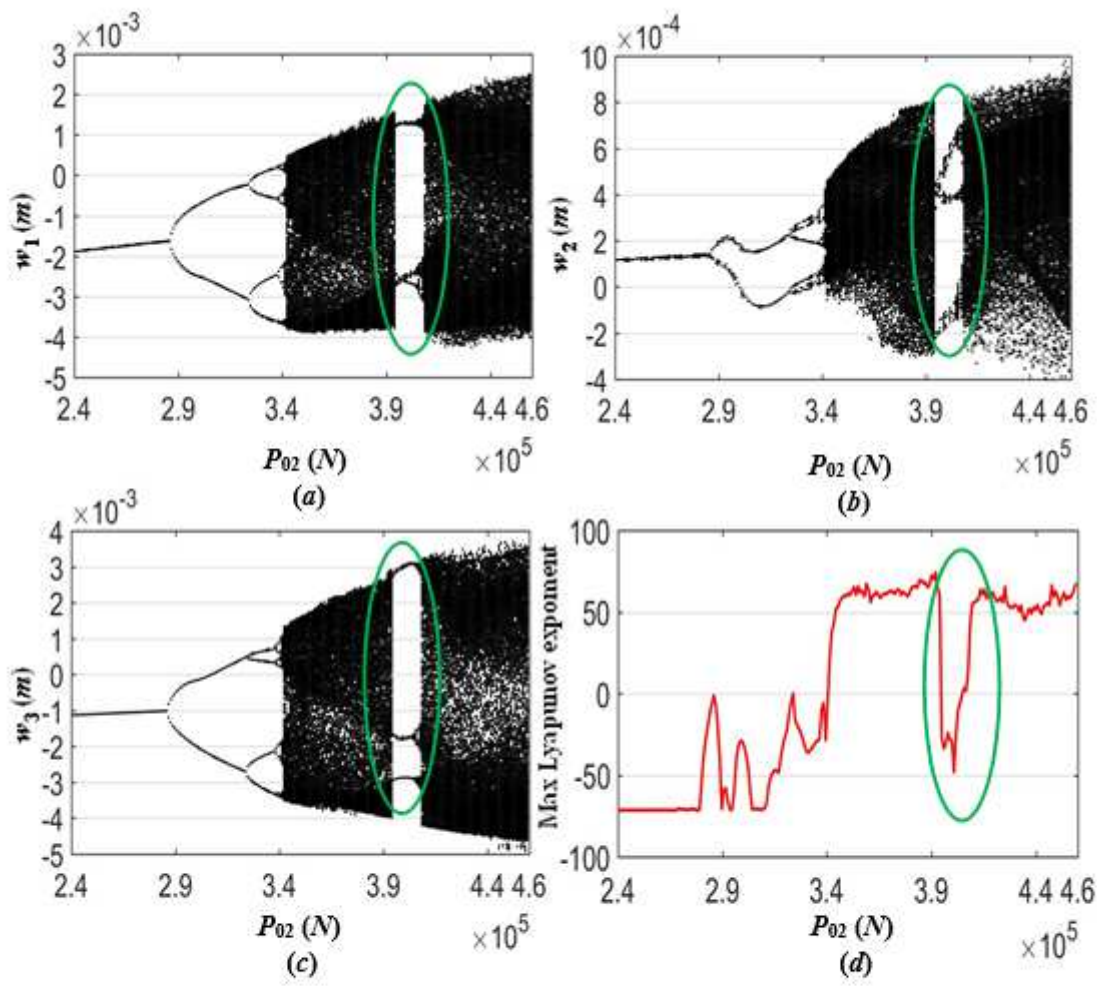


Figure 13

Figure 13

Please see the Manuscript PDF file for the complete figure caption.

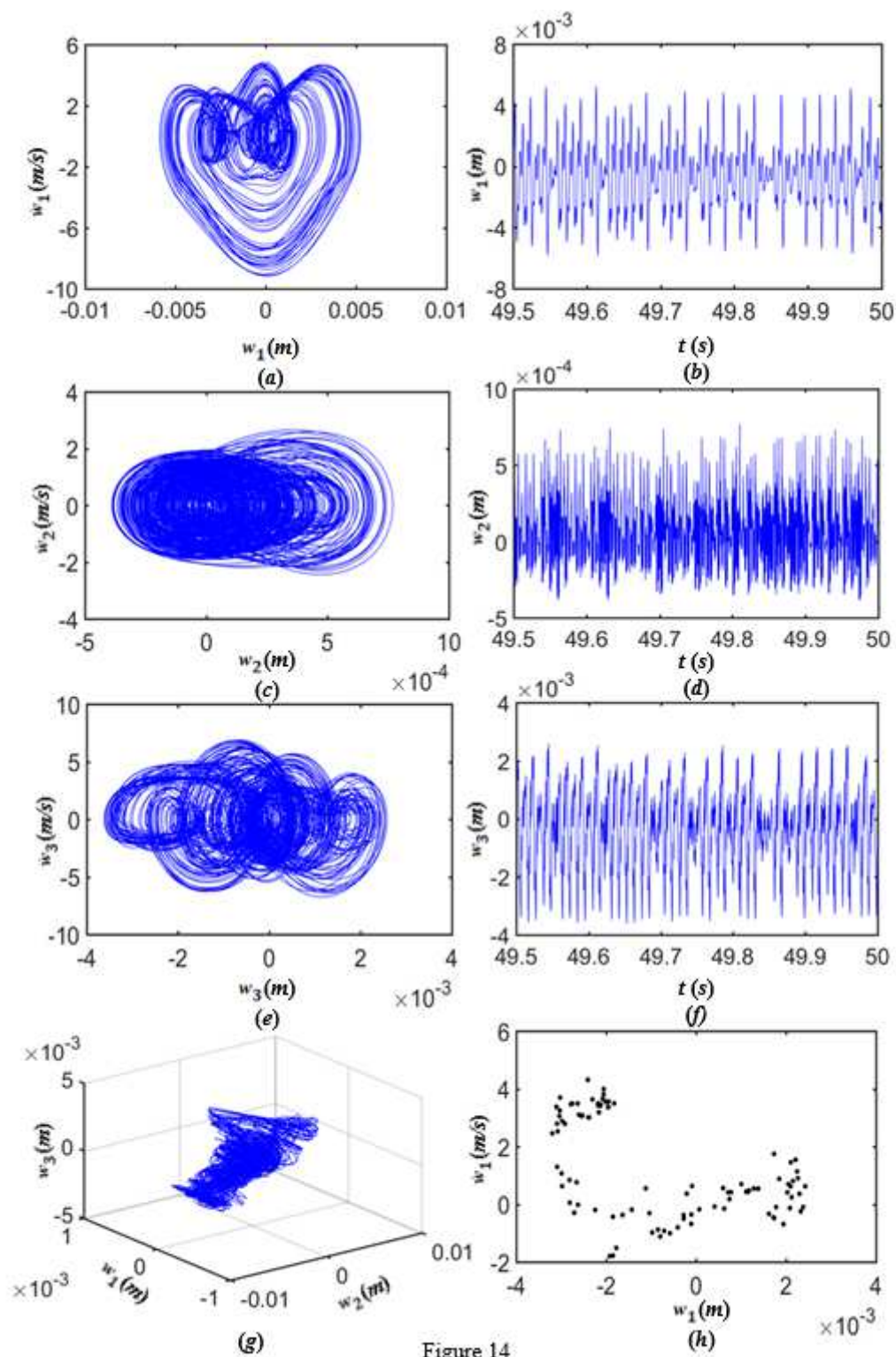


Figure 14

Figure 14

Please see the Manuscript PDF file for the complete figure caption.

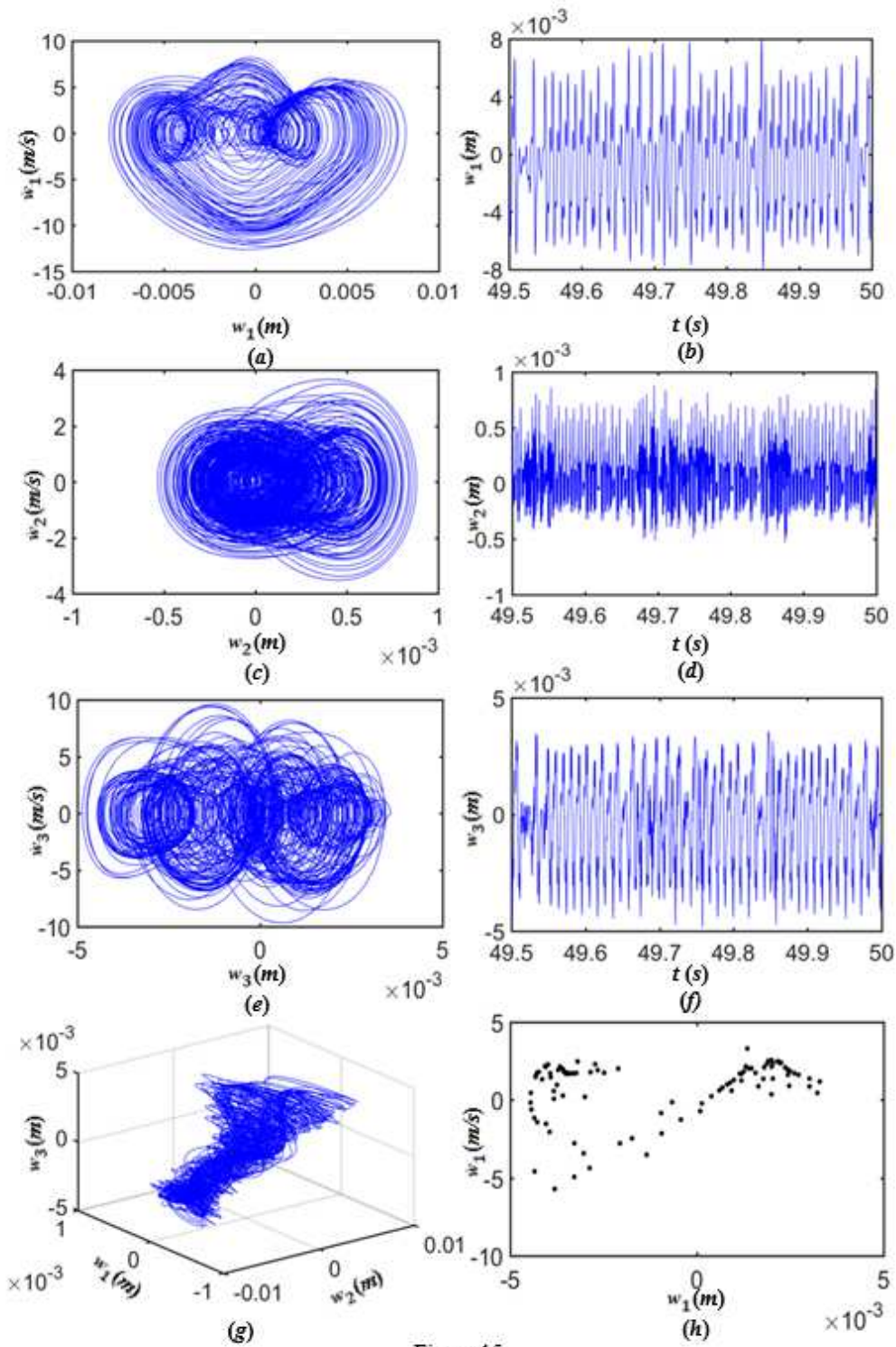


Figure 15

Figure 15

Please see the Manuscript PDF file for the complete figure caption.

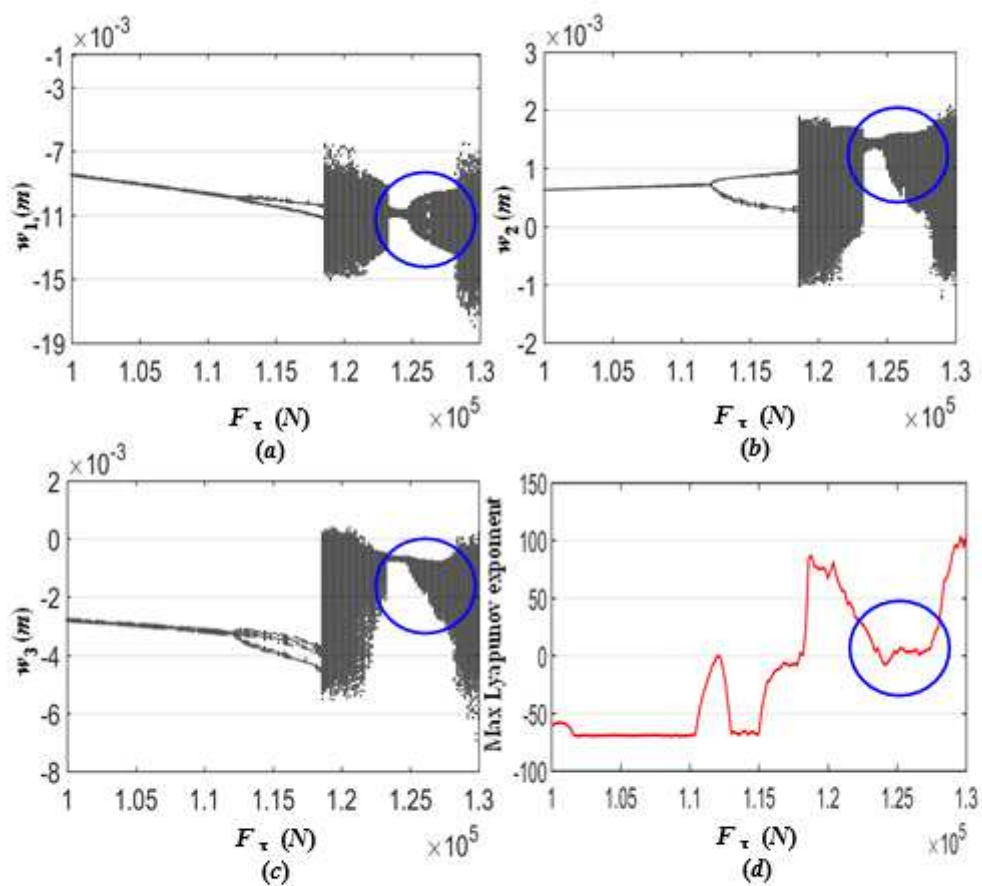


Figure 16

Figure 16

Please see the Manuscript PDF file for the complete figure caption.

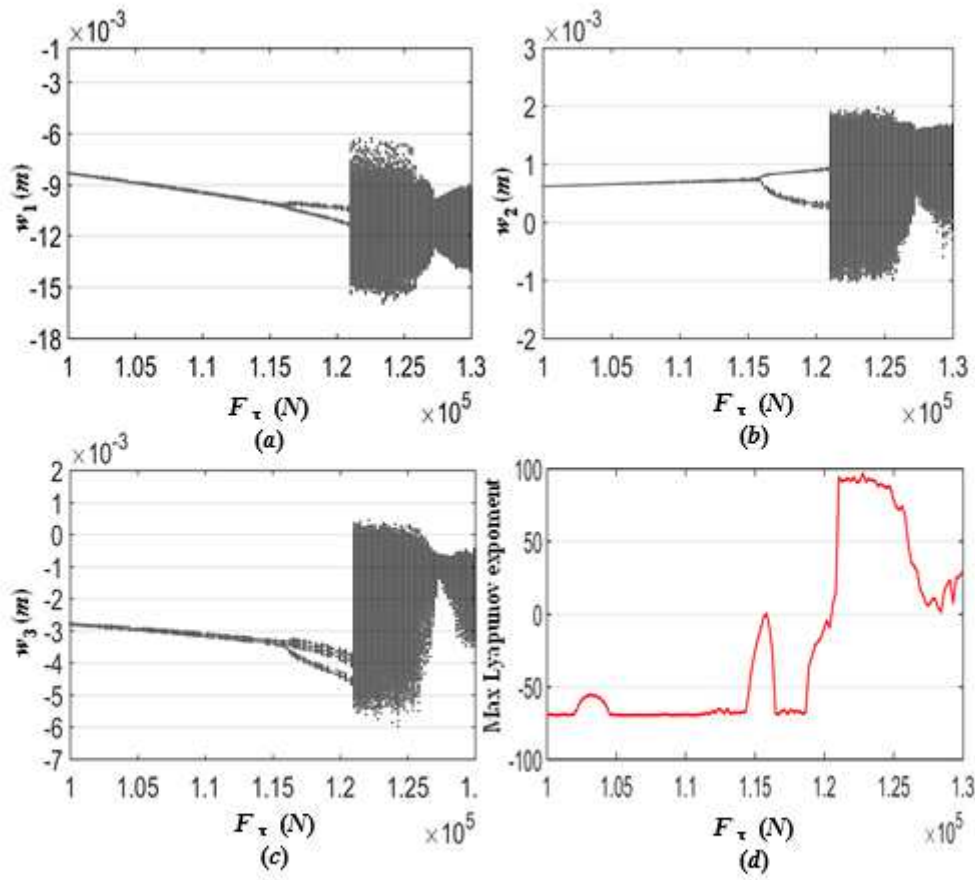


Figure 17

Figure 17

Please see the Manuscript PDF file for the complete figure caption.

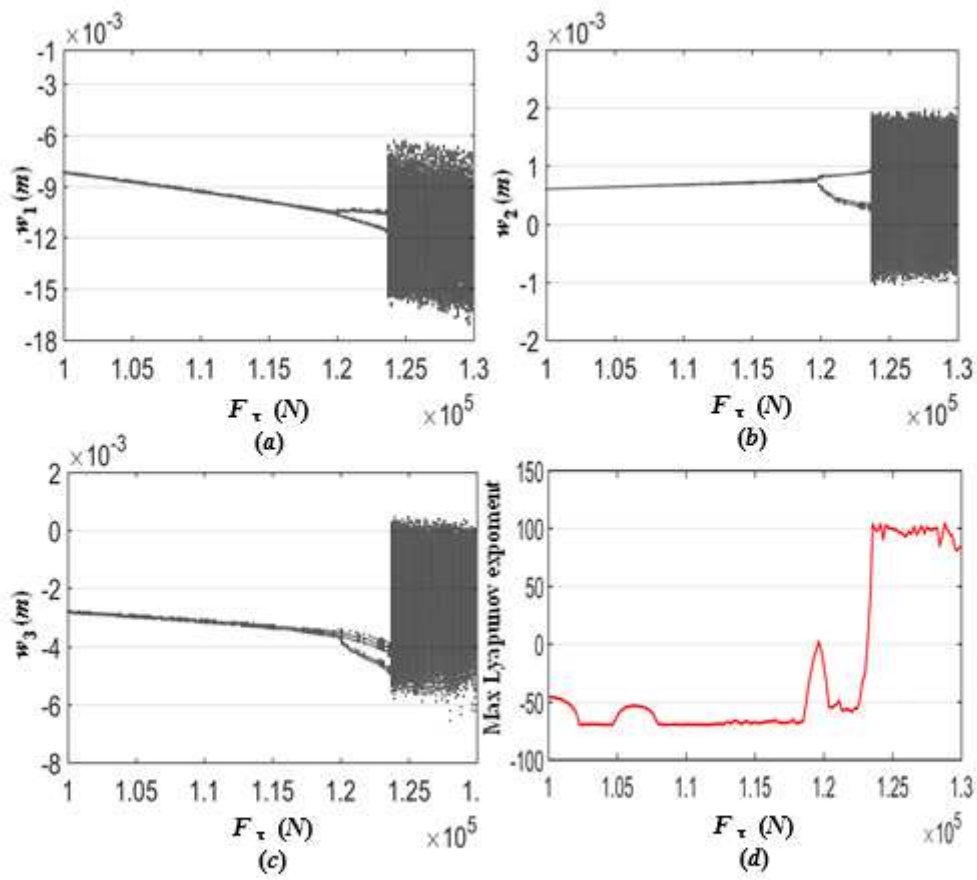


Figure 18

Figure 18

Please see the Manuscript PDF file for the complete figure caption.

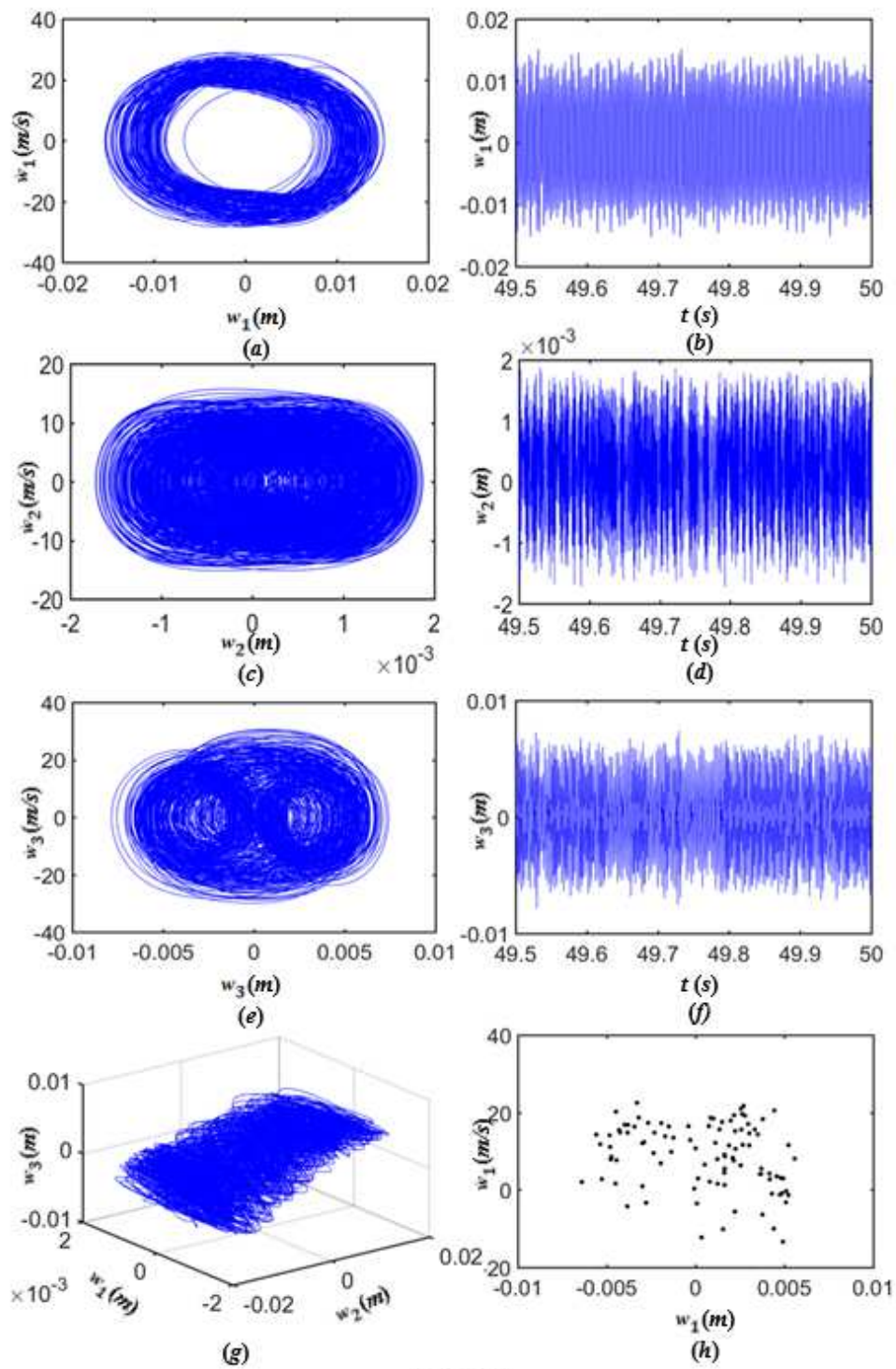


Figure 19

Figure 19

Please see the Manuscript PDF file for the complete figure caption.

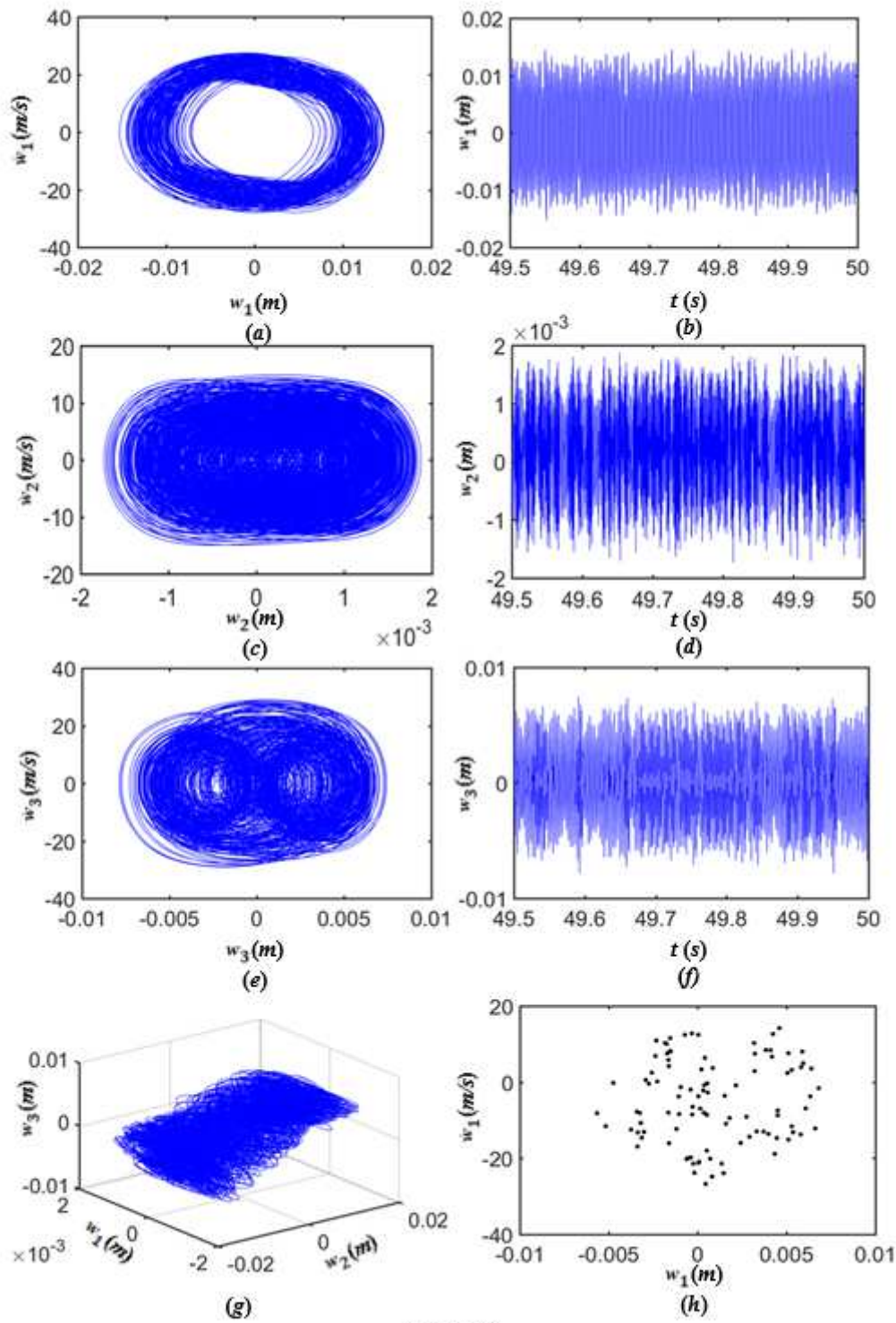


Figure 20

Figure 20

Please see the Manuscript PDF file for the complete figure caption.